THESIS REPORT
Ph.D.

SYSTEMS
RESEARCH
CENTER

Supported by the National Science Foundation Engineering Research Center Program (NSFD CD 8803012), Industry and the University

Kinematic Synthesis of Bevel-Gear-Type Robotic Wrist Mechanisms

by C.C. Lin
Advisor: L.W. Tsai

Ph.D. 90-7

Kinematic Synthesis of Bevel-Gear-Type Robotic Wrist Mechanisms

by
Chen-Chou Lin

Dissertation submitted to the Faculty of the Graduate School
of The University of Maryland in partial fulfillment
of the requirements for the degree of
Doctor of Philosophy
1990

Advisory Committee:

Professor Lung-Wen Tsai, Chairman/Advisor
Profesor Bruce Berger
Professor Jackson C.S. Yang
Associate Professor Shapour Azarm
Asistant Professor Wijesuriya P. Dayawansa

THE UNIVERSITY OF MARYLAND

COLLEGE PARK CAMPUS

GRADUATE STUDIES AND RESEARCH

Date: July 10, 1990

Report of Examining Committee

Name of degree candidate Chen-Chou Lin S.S.# 216-06-7181

Degree sought PhD

Date of Oral Examination Nov. 9, 1990

The Examination and thesis or dissertation has been approved by the following committee. Signatures of the committee indicated that all thesis or dissertation corrections have been made.

Chairman: Lung-Wen Tsai

[illegible]

[illegible]

[illegible]

N. P. Dayawansa

Representative of the Graduate Dean:

(To be returned to Graduate Records Office as soon as signed by the Committee)

8/87

ABSTRACT

Title of Dissertation: KINEMATIC SYNTHESIS OF BEVEL-GEAR-TYPE ROBOTIC WRIST MECHANISMS

Chen-Chou Lin, Doctor of Philosophy, 1990

Dissertation directed by: Lung-Wen Tsai, Professor
Mechanical Engineering Department
and
Systems Research Center

Bevel-gear-type robotic wrist mechanisms are commonly used in industry. The reasons for their popularity are that they are compact, light-weight, and relatively inexpensive. However, there are singularities in their workspace, which substantially degrade their manipulative performance. The objective of this research is to develop an atlas of three-degree-of-freedom bevel-gear-type wrist mechanisms, and through dimensional synthesis to improve their kinematic performance. The dissertation contains two major parts: the first is structural analysis and synthesis, the other is kinematic analysis and dimensional synthesis.

To synthesize the kinematic structures of bevel-gear-type wrist mechanisms, the kinematic structures are separated from their functional considerations. All kinematic structures which satisfy the mobility condition are enumerated in an unbiased, systematic manner. Then the bevel-gear-type wrist mechanisms are identified by applying the functional requirements. Structural analysis shows that a three-degree-of-freedom wrist mechanism usually consists of a non-fractionated,

two-degree-of-freedom epicyclic gear train jointed with the base link. Therefore, the structural synthesis can be simplified into a problem of examining the atlas of non-fractionated, two-degree-of-freedom epicyclic gear trains. The resulting bevel-gear-type wrist mechanisms has been categorized and evaluated. It is shown that three-degree-of-freedom, four-jointed wrist mechanisms are promising for further improving the kinematic performance.

It is found that a spherical planetary gear train is necessarily imbedded in a three-degree-of-freedom, four-jointed wrist mechanism. Therefore, to study the workspace and singularity problems of three-degree-of-freedom, four-jointed spherical wrist mechanisms, we have to study the trajectories of spherical planetary gear trains. The parametric equations of the trajectories and some useful geometric properties for the analysis and synthesis of workspace are derived. The workspace boundary equations can be derived via both geometric consideration and Jacobian analysis. The workspace is divided by inner and outer boundaries into regions of accessibility of zero, two and four. The design criteria of full workspace and a maximum four-root region are established. Finally, a design is suggested based on its kinematic performance.

To the Lord

ACKNOWLEDGEMENT

I would like to express my deepest gratitude to my advisor, Dr. Lung-Wen Tsai, for his guidance, patience, and constructive criticism during the research, and for his financial support throughout these years of my graduate studies.

Acknowledgements are also due to Dr. J.C.S. Yang, Dr. B. Berger, Dr. S. Azarm, and Dr. W.P. Dayawansa, for their serving in my advisory committee and for reading this dissertation and providing helpful comments.

I would like to dedicate this work to my father, who passed away three years ago, and yet his endless love upon me will always be in my memory. I wish to thank my family, my mother, brother, and sister, for their long-term support which made this all possible. Finally, I would like to thank my wife, Yen-Chin, for her love, patience and encouragement over these years.

This work was supported in part by the U.S. Department of Energy under Grant DEF05-88ER13977 and in part by the NSF Engineering Research Centers Program, NSFD CDR 8803012. Such support does not constitute an endorsement by the supporting agencies of the views expressed in the dissertation.

TABLE OF CONTENTS

LIST OF TABLES

LIST OF FIGURES

Chapter 1

INTRODUCTION

1.1 Robot design

Robot, by definition [51], is an automatically controlled, reprogrammable, multi-purpose manipulative machine with or without locomotion for use in industrial automation applications. This definition includes manipulators, numerical control machines, walking machines, and science-fiction humanoids. Although people most commonly perceive robots to be of the anthropomorphic (human-like) type, yet industrial robots nowadays are hardly humanoid in appearance. Most industrial robots today are in fact mechanical arms, or manipulators. A manipulator can be divided into four components: the base, arm, wrist, and end-effector. Usually, the arm is used for global motion, while the wrist and end-effector are used for fine manipulation.

The emergence of industrial manipulators was primarily due to the need of flexible manufacturing and automation in industry, and partly due to the advancement of new technologies. *Robotics* is a consequence of the continuing development on a broad front in such diverse fields as materials, mechanics, controls, and computers. It concerns itself with the desire to synthesize some aspects of human function by using mechanisms, sensors, actuators, and computers.

Although much effort has been spent in robotics, the ultimate goals for the development of 'intelligent robots' that can emulate human functions are unrealized. Some problems are attributed to the fact that the required technologies have not been established. For example we need better tactile sensors to interpret touch data, motors that can generate large torques for direct-drive purpose, and experimental evaluation for modern control techniques, etc. Important problems that need to be solved are listed in [6], including problems in vision, sensing, mobility, design, control, planning, reasoning, and system integration. On the other hand, new technologies such as artificial intelligence, adaptive control, and neural networks are rapidly advancing and seem very promising in the future development of robotics.

Kinematics is among the most important factors affecting manipulator performance. In particular, kinematics determine the motion and force transmissions from the manipulator joints to the end-effector. From the kinematics and mechanism design point of view, major issues of concern are: (i) workspace, (ii) manipulability, (iii) singularity, and (iv) computational efficiency.

(i) Workspace & (ii) manipulability

Workspace volume and manipulability are the two most important performance indices in the design process. Since manipulators are used to manipulate objects in space, the workspace must be as large as possible, and the *manipulability* must be optimized under certain constraints. Roth [55] was the first to address the workspace problem. Since the kinematics of manipulators are highly nonlinear, it is not an easy task to identify the workspace boundaries and determine the *regions of accessibility* [30,32,33,34]. Workspace synthesis is an even more complicated problem, because it usually involves solving nonlinear kinematic equations and inequalities. Gupta and Roth [26] have investigated the synthesis of an arm linkage when *dexterous workspace* is specified. Yoshikawa [69] proposed the idea of manipulability measure, which is the 'distance' between the current position of the end-effector and the singular point. Later, Asada and Cro Granito [4] used the condition number and average velocity ratio to establish the criteria of optimality. Gosselin and Angeles [25] defined a global conditioning index to measure the global behavior of the condition number of the manipulator. Chiu [13] found that the manipulability must be obtained at the expense of accuracy, and defined a task-dependent performance measure. All the kinematic and static evaluations are based upon the *Jacobian matrix*, a matrix that transforms the joints velocity vector to the end-effector velocity vector.

(iii) Singularity

A manipulator may contain singularities in its workspace. When a manipulator is singular (degenerate), it loses one or more degrees of freedom and becomes immovable in certain directions. At this point, the manipulator's Jacobian matrix becomes singular. As a result, joint rates tend to be infinite and lead to loss of control. Paul and Stevenson [47] have investigated singularity for three-DOF (degree-of-freedom), three-jointed robotic wrist mechanism. It was pointed out that around singular points, there exist conic zones in which mobility is significantly degraded. The problems of singularity can be solved by adding a redundant degree of freedom to eliminate singular points inside the workspace. However, this redundancy necessitates a much more complex control system [19,40], virtually negating the advantages. Another method to deal with singularities is to move singular points out of the workspace [59] or to relocate them in less essential working zones.

(iv) Computational efficiency

To locate an end-effector at a specified position and orientation, it is necessary to obtain the corresponding joint displacements of the manipulator. Therefore, kinematic equations must be solved for joint displacements. This problem is called the *inverse kinematics problem.* The number of real solutions for inverse kinematics depends on the manipulator architecture and the desired end-effector position and orientation. For a six-DOF manipulator, the number of real solutions can be up to sixteen [42]. Many researchers have investigated the inverse kinematics problems to improve the computational efficiency [1,29,41,48,49]. Tsai and Morgan [60] are the first to develop an off-line algorithm using the homotopy map technique to solve all the real and complex roots for the general six-DOF manipulators with all revolute joints. Since computational efficiency is very crucial in the real-time controlled manipulation process, most industrial manipulators are built to possess closed-form solutions for the inverse kinematics. Pieper [50] has shown that a manipulator with three adjacent joint axes intersecting at a point leads to a closed-form solution for the inverse kinematics. For this reason, many industrial manipulators possess spherical wrist mechanisms in which the three joint axes intersect at the wrist center.

Despite the availability of somewhat sophisticated mechanical hands (for example, Stanford/JPL hand [56] and Utah/MIT hand [31]), most end-effectors used in industry today are simple clamping devices such as grippers, losing the manipulative ability of fingers as in a human hand. Thus there is a great need to design robot wrists that can provide better manipulability and large workspace. This dissertation will concentrate on the design and development of *Bevel-Gear-Type wrist mechanisms*, one class of wrist mechanism that is commonly used in many industrial manipulators; and the associated kinematics problems such as singularity and workspace.

1.2 Bevel-gear-type robotic wrist mechanisms

In a three-dimensional Cartesian space, a rigid body possesses six degrees of freedom, three translational and three orientational degrees of freedom. Therefore, to position and orient an object freely in a three-dimensional space, a manipulator must have at least six degrees of freedom. Figure 1.1 shows the kinematic structure of a serially-jointed, six-DOF manipulator with all revolute joints. Usually, the first three joints are used for controlling the end-effector position (gross motion), and the last three for controlling the orientation (local motion). So the linkage associated with the first three moving links is called the major linkage, or the arm, and the portion associated with the last three moving links is called the minor linkage, or the wrist. Note that in Fig. 1.1, the three joint axes of the wrist intersect at a point, therefore, the wrist mechanism is spherical.

The kinematic structure of the serially-jointed manipulator shown in Fig. 1.1 has an open-loop configuration. Intuitively, we may mount actuators on each joint axis to drive the manipulator. This simple idea, called *direct-drive,* however, is still not feasible using today's motor technology. This is because a direct-drive manipulator needs motors that can generate very large torques. Usually, such motors are very heavy; if mounted on each joint, they become a huge burden for the manipulator. Therefore, most industrial manipulators are driven through gearing mechanisms, chains, linkages, or other power transmission mechanisms. In this way, motors can be mounted remotely to reduce inertia effects and to achieve torque amplification. Hence, the major problem in designing a wrist mechanism is

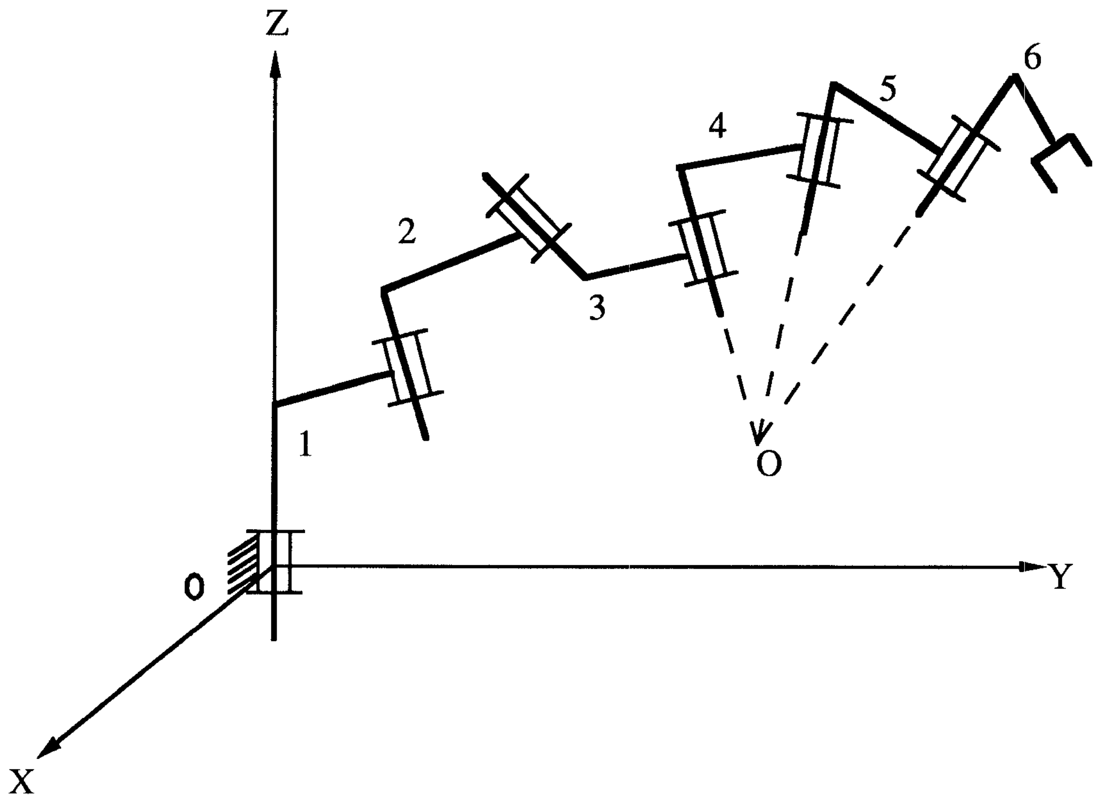

Figure 1.1 The kinematic structure of a
serially-jointed manipulator

not achieving the wrist functions, but rather power transmission.

The development of mechanisms that can provide multi-directional rotation motions may be dated back to the thirteen century, when *universal joints* were first introduced by an architect. Later, in the seventeen century, British physicist Robert Hooke described an operational theory for universal joints. He also invented the *double-jointed cardan universal joint* that can be applied to derive constant velocity transmission. Today many industrial robot wrists still bear the shape of universal joints (Hook Joints). It was not until the late 1940s that modern wrist technology emerged due to the need to handle nuclear materials and to perform hazardous work. Since then a considerable amount of work has been done in inventing wrist mechanisms. Rosheim [54] provides a thorough survey in the current development of wrist actuator technology, including patents and published papers. His book also contains design suggestions and other information for inventing a robot wrist mechanism. Generally, most of these inventions were not accomplished on a systematic basis, instead relying solely on the individual ingenuity of the designer.

This research focuses on the kinematic synthesis of bevel-gear-type wrist mechanisms based upon the following considerations:

1. Bevel-gear-type wrist mechanisms are commonly used in industry. Several different constructions for this type of wrist mechanism exist, such as PUMA, Bendix, and Cincinnati-Milacron 3-roll wrist mechanisms. Thus the following question is raised: "How many different constructions exist for this type of wrist mechanisms for a given number of links and number of degrees of freedom?" This motivates me to study the structural characteristics of the mechanisms, and further to synthesize them systematically.

2. They are comparatively simple and compact in size. Although there are singularities in their workspace, when compared to other "singularity-free" wrist mechanisms described in [54], bevel-gear-type wrist mechanisms are much simpler in construction. Besides that, they can be sealed in a metallic housing, reducing the cost of construction and maintenance.

3. Using bevel gear trains for power transmission, the actuators can be mounted remotely (on the forearm). Therefore, the weight and dynamic effects can be reduced.

Figure 1.2(a) shows a mechanical drawing of the Cincinnati-Milacron 3-roll wrist mechanism, and Fig. 1.2(b) shows the schematic drawing. The wrist mechanism has seven links (including base link), six turning pairs and three gear pairs. Therefore, it has three degrees of freedom. Since there are three articulation points, we call this type of mechanisms three-DOF, three-jointed wrist mechanisms. In Fig. 1.2(b), link 0 is the forearm of the manipulator, and link 3 is the end-effector mount. The wrist actuating system is installed remotely in the forearm and attached to links 1, 4 and 5 through three concentric shafts. Because the three joint axes, a, b, and c intersect at one point (wrist center), the end-effector will perform a spherical motion about the wrist center. The wrist-roll motion is accomplished by driving link 1. Therefore, the end-effector can rotate about the a-axis. The pitch motion is accomplished by driving link 4. Through the gear mesh between links 4 and 2, the end-effector can rotate about the b-axis. The tool-roll motion is accomplished by driving link 5. Through two gear meshes, the end-effector can rotate about the c-axis. The 3-roll wrist has the important feature that there is no mechanical interference, therefore continuous rotational motions about the three joint axes can be achieved. Note that the three-DOF wrist mechanism can be re-

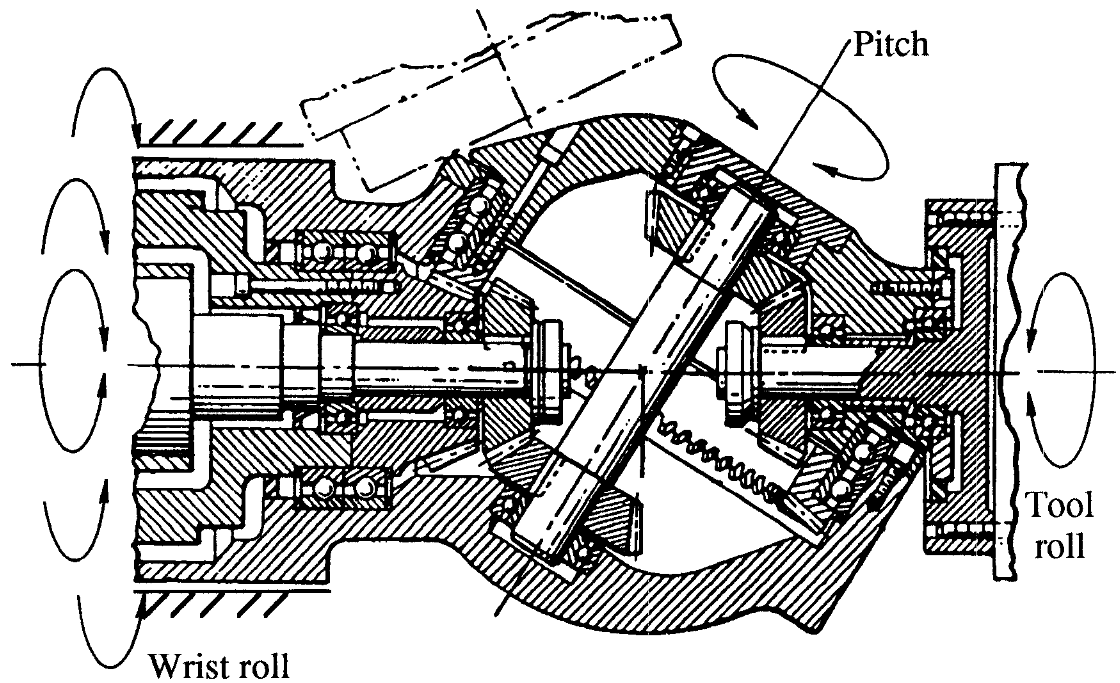

(a)The mechanical drawing

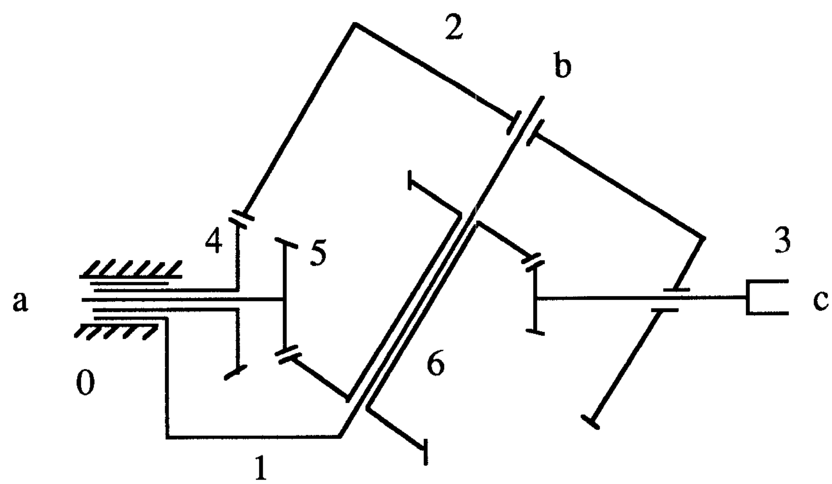

(b) The schematic drawing

Figure 1.2 A Cincinnati-Milacron 3-roll wrist mechanism garded as a two-DOF gear train jointed with a single link (the base link). We call the three-DOF wrist mechanism a *fractionated* mechanism. On the other hand, the two-DOF gear train, which cannot be further divided into two components, is non-fractionated. The formal definition of non-fractionated mechanisms and the method of identifying them will be discussed in Chapter 3.

1.3 Overview

The objective of this research is to study the singularities and workspace problems associated with bevel-gear-type robotic wrist mechanisms, and to create new and innovative wrist mechanisms with good manipulability.

The contents of this dissertation can be categorized into two major parts: the first being structural analysis and synthesis; the other being kinematic analysis and dimensional synthesis. In structural analysis and synthesis, three subtopics are discussed: (i) the structural analysis of bevel-gear-type wrist mechanisms (Chapter 2); (ii) the topological synthesis of non-fractionated, two-DOF epicyclic gear trains (Chapter 3); and (iii) the development of an atlas of bevel-gear-type robotic wrist mechanisms (Chapter 4). In kinematic analysis and dimensional synthesis, two subtopics are explored: (i) the trajectory analysis of spherical planetary gear trains (Chapter 5); and (ii) the workspace of three-DOF, four-jointed spherical wrist mechanisms (Chapter 6).

The basic idea for creating new wrist mechanisms in this research is based upon separation of kinematic structures from their functional requirements. Mechanism structures thus can be created systematically using graph theory and combinatorial analysis. In Chapter 2, the kinematic structure of an existing bevel-gear-type wrist mechanism is analyzed to establish the functional requirements for this type of wrist mechanism. The major considerations in establishing functional requirements are: (i) the topological relationship between the number of turning pairs and the number of gear meshes; (ii) the arrangements of turning pairs which allow at least three coaxial inputs and three articulation joints; and (iii) the arrangements of gear meshes which allow power transmission from actuators to end-effector. The analysis procedure is generalized using ***graphs*** to represent the kinematic structure of the mechanism. An examination reveals that a three-DOF wrist mechanism consists of a non-fractionated, two-DOF epicyclic gear train jointed with a single link. Therefore the next step for creating the bevel-gear-type wrist mechanisms is to enumerate all the non-fractionated, two-DOF epicyclic gear trains.

In Chapter 3, a systematic methodology is developed to enumerate the kinematic structures of non-fractionated, two-DOF epicyclic gear trains. The enumeration of kinematic structures is based on the fundamental rules of epicyclic gear trains. The *isomorphic graphs* are identified and eliminated by comparing the *linkage characteristic polynomials.* Then a simple algorithm for the identification of non-fractionated mechanisms is introduced. Since the enumeration and identification process requires significant computational efforts, the procedures are implemented on a digital computer. Finally, generic design guidelines for two-DOF epicyclic gear trains are proposed, based on practical constraints. Using these design guidelines, graphs that have potential applications in two-input devices are highlighted.

In Chapter 4, the functional requirements established in Chapter 2 are applied to the results obtained from Chapter 3, then all the bevel-gear-type wrist mechanisms are identified (created). The results are then categorized according to their structure matrices and link numbers. Finally, bevel-gear-type wrist mechanisms with four joint axes are evaluated based on the kinematics perspective. As the kinematic structures of three-DOF, four-jointed wrist mechanisms are significantly different from those of three-jointed wrist mechanisms, so is their kinematic performance. Due to their promising characteristics, three-DOF, four-jointed wrist mechanisms are further studied and optimized in the next two chapters.

In Chapter 5, the trajectories of spherical planetary gear trains are studied. The trajectory analysis is the preliminary step for the study of the workspace and singularity for three-DOF, four-jointed spherical wrist mechanisms. The parametric equations of trajectory are derived. It is shown that the trajectory generated by a tracer point on the planet of a spherical planetary gear train is analogous to that of the planar case. Two cases, gear ratio equal to one and two, are presented in detail including the geometric description, planes of symmetry, extent of trajectories, number of nodes (cusps) and their locations. The criteria for the existence of cusps are verified algebraically and interpreted from the geometrical point of view.

In Chapter 6, the orientational workspace of three-DOF, four-jointed spherical wrist mechanisms is investigated. The workspace boundary equations are derived via both geometric consideration and Jacobian analysis. It is shown that for the first type of wrist mechanism with links 2 and 3 coupled, the workspace boundary consists of circles centered at fixed axis of rotation; while for the second type of mechanism with links 1 and 2 coupled, the boundary consists of two branches of curves. The workspace is divided by inner and outer boundaries into regions of accessibility zero, two and four. The criteria for full workspace design as well as for maximum four-root regions have been established.

Finally, in Chapter 7, the dissertation is reviewed and suggestions are given for future research.

The contributions of this research are:

1. Development of a systematic approach for the creation of bevel-gear-type robotic wrist mechanisms.
2. Creation of a class of non-fractionated, two-DOF, epicyclic gear trains.
3. Creation of an atlas of three-degree-of-freedom, bevel-gear-type wrist mechanisms.
4. Contribution to the understanding of the geometric properties of trajectories of spherical planetary gear trains.
5. Contribution to the basic understanding of the structural characteristics and the kinematic property of bevel-gear-type wrist mechanisms, including workspace and singularity.

Chapter 2

STRUCTURAL ANALYSIS OF BEVEL-GEAR-TYPE SPHERICAL WRIST MECHANISMS

2.1 Introduction

In this chapter, we shall examine the ideal characteristics for robotic wrist mechanisms and establish the fundamental requirements of bevel-gear-type spherical wrist mechanisms.

Pieper [50] showed that a manipulator with three adjacent joint axes intersecting at a point leads to a closed-form solution for the inverse kinematics. Hence, a spherical wrist makes the decoupling of position and orientation possible. And the computational efficiency can be improved. In addition to the need for a wrist to perform a spherical motion, the recent trend in wrist technology has required the wrist to be dexterous. Since 1940s many researchers have devoted themselves in creating simple and cost effective wrist mechanisms which can fulfill the above requirements. We may find it difficult to design a wrist mechanism which satisfies all the important demands such as dexterity, simplicity and inexpensiveness. Some wrist mechanisms are claimed to be singularity-free. However, they often suffer from the problems of complicated (heavy) mechanical construction, less stiffness and less precision [46,59]. On the other hand, bevel-gear-type wrist mechanisms, such as PUMA, Bendix, Cincinnati-Milacron 3-roll wrists, are considered to be simple, reliable, and cost effective, but they generally contain singularities in their workspace. Furthermore, because actuators can be mounted remotely from the joint center, they suffer less vibration and dynamics problems. We can ask ourselves the following question: for a given number of links, how many spherical bevel-gear-type wrist mechanisms exist? To answer this question, one can resort to the aide of graph theory [21]. In what follows, functional requirements for the design of bevel-gear-type, spherical wrist mechanisms will be established.

2.2 Robot wrist characteristics

The ability of a robot to manipulate an object depends strongly on the performance of the wrist mechanism. The major linkage of a robot manipulator provides the ability for moving an object globally in the workspace, while the usual manipulation task is usually accomplished in the local area. Thus, proper design of a wrist mechanism is critical in the performance of a manipulator. Dexterity is a very important factor in designing a robot wrist mechanism. In addition, compactness and simplicity are also essential requirements. In general, an ideal wrist mechanism should possess the following characteristics:

- A minimum of three degrees of freedom
- Small size and light weight
- Remote drive system
- High accuracy and repeatability

- High mechanical stiffness
- Large workspace
- End-effector possess a spherical motion
- Low manufacturing and maintenance cost

Some of the above characteristics call upon proper dimensioning of mechanical parts, known as the dimensional synthesis. Many researchers have been working on this area [2,4,24,25]. Others call upon proper configuration of the mechanism, known as the structural synthesis. In this chapter, we shall only focus on the structural analysis. The structural synthesis will be discussed in Chapters 3 and 4. And the dimensional synthesis will be discussed in Chapter 6.

We may consider a three-DOF wrist as a multi-input and multi-output system, where the inputs are the actuator displacements or torques, and the outputs are the angular orientation or torques about the wrist center of an end-effector. The system transfers the motion or power from the actuators to the end-effector. To transfer power, one may use gear trains, tendons, linkages, or gear mechanisms, etc. In addition to power transfer, the system should also perform rotational motion (ideally spherical motion) for the end-effector. Among the above construction alternatives, bevel gear trains seem to be more preferable than others, since gear train mechanisms have the advantages of design simplicity and compactness. Other mechanisms, such as coupled spherical four-bar linkage configuration and universal-joint configuration [54], are either too complicated in construction, or lack of stiffness, or are bulky in nature.

In this dissertation, we shall concentrate on the creation of bevel-gear-type wrist mechanisms. First functional requirements for the design of spherical wrist mechanisms will be established. Then these requirements will be used for the purpose of structural synthesis.

2.3 Bevel-gear-type spherical wrist mechanisms

Before establishing functional requirements for the bevel-gear-type spherical wrist mechanisms, let us examine the topological characteristics associated with an existing mechanism. A typical bevel-gear-type spherical wrist mechanism is the Cincinnati-Milacron 3-roll wrist designed by Stackhouse [58]. Aside from its special arrangement of axes orientation which permits full range of rotation, let us look into its kinematic model. Figure 2.1(a) shows the functional representation; Figure 2.1(b) shows the equivalent open-loop chain [62], obtained by deleting the drive trains from the mechanism; And Fig. 2.1(c) shows the canonical graph representation of the mechanism [62]. In a graph representation, links are denoted by vertices, joints by edges, and the edge connection of vertices corresponds to the joint connection of links. In order to distinguish different types of joints, the edges can be colored and/or labeled. For epicyclic gear trains, turning pairs are represented by thin edges, gear pairs by heavy edges, and the thin edges are labeled according to their axis locations in space. See next chapter or [63] for the definition of graph elements in an epicyclic gear train. The reason for using graphs to represent kinematic structures is that systematic methodology for the structural enumeration of gear trains can be easily implemented and processed in a digital computer. Since from structural analysis point of view, we are only concerned with the topological relations between links and joints, the actual locations of links or joints are irrelevant. A kinematic analysis reveals that the mechanism has three degrees of freedom. The three input links are links 2, 6, and 7, and the output link

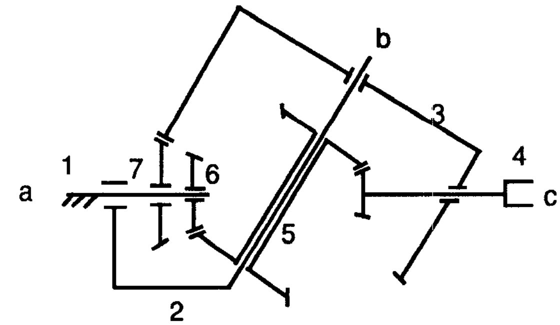

(a) Functional representation

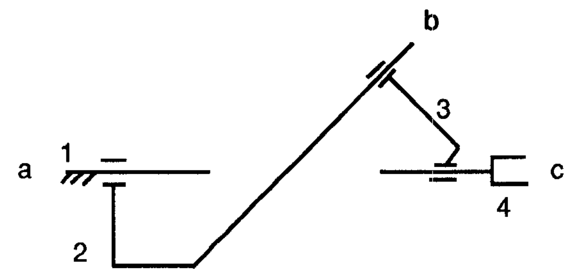

(b) Equivalent open-loop chain

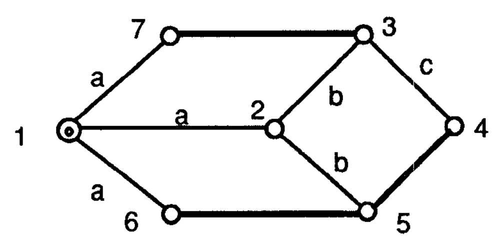

(c) Canonical graph representation

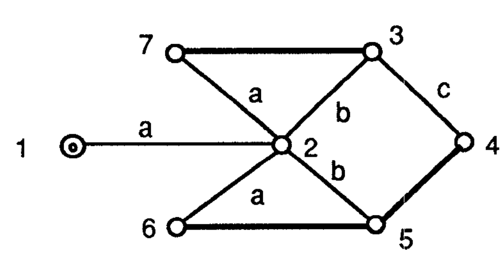

(d) Graph representation of pseudoisomorphic mechanism

Figure 2.1 The kinematic model of a 3-roll wrist mechanism is link 4.

In the equivalent open-loop chain, four links (including the base link) are serially connected by revolute joints, and three axes of rotation intersect at one common point which called the wrist center. Since the equivalent open-loop chain is imbedded in the mechanism, its graph representation is a sub-graph of the graph representing the whole mechanism. Examining Fig. 2.1(c), we note that the sub-graph for the equivalent open-loop chain is the thin-edged (denoting turning pair) path, 1-2-3-4, connecting the base link to the end-effector. The three labels, a, b, and c, in the thin-edged path represent the locations of the joint axes.

One advantage of the bevel-gear-type spherical wrist is that actuators can be located remotely from the wrist center, which make the wrist mechanism light weight and compact. This is accomplished by the use of gear trains which permit the transfer of power from the base level to the mid-level and then the end-effector level. As shown in Fig. 2.1(c), there are two heavy-edged paths (transmission lines [11]) starting from the base level, one ended at the end-effector level and the other at the mid-level. Relative motions of link 4 with respect to link 3, and link 3 with respect to link 2 are accomplished by the two transmission lines defined by the heavy-edged paths 7-3 and 6-5-4. Relative motion of link 2 with respect to link 1 is accomplished by driving link 2 directly.

Furthermore, since links 1, 2, 6, and 7 are coaxial, the mechanism shown in Fig. 2.1(c) can be rearranged into one with an *articulation point* [63] as shown in Fig. 2.1(d). It can be concluded that, in general, a three-DOF wrist can be constructed by connecting a non-fractionated, two-DOF gear-train in series with a base link. The term, *non-fractionated*, means the mechanism can not be divided into two or more components with a common link but no common joint. The definition will be discussed in Chapter 3 in more detail. The third degree of freedom is simply obtained by rotating the two-DOF gear train as a whole about the base link. Thus we may simplify the synthesis problem by developing an atlas of non-fractionated, two-DOF gear trains.

From the above discussion, the fundamental requirements for a graph of gear train to be admissible for the construction of a spherical wrist can be summarized as follows:

R1 There must be three or more vertices connected together with thin edges of the same label. These vertices are potential candidates for input links.

R2 In the graph, there must be at least two heavy-edged paths originated from the input vertices. An input link can be the starting vertex of one of heavy-edged paths. On the other hand, two heavy-edged paths can meet at a common vertex other than the input vertex.

R3 There must exist at least three edge levels in one of the thin-edged paths originating from the input vertices.

R4 A link is considered as redundant, if removal of the link and its associate joints from the kinematic chain does not change the degrees of freedom of the mechanism. Note that the input links and the end-effector link are not to be removed. We shall consider only those mechanisms with no redundant links.

The first requirement has been derived from the fact that the size and inertia of the wrist must be as small as possible. The input links must be coaxial to permit all the actuators be connected to the base link.

The second requirement states that power is to be transmitted from the input links to other links via gear meshes.

The third requirement states that there should be at least three different levels from the base link to the end-effector. The three articulation points enable the wrist to perform a three-DOF motion. However, if there are more than three levels, then some of the articulation points are coupled, and only three of them are independent.

The fourth requirement is set primarily for the reason of efficiency. A redundant link does nothing but waste energy. Elimination of redundant links results in a mechanism having the same degree of freedom and with fewer links. Hence mechanisms with redundant links will be discarded.

The above fundamental requirements are believed to be sufficient for the creation of a class of bevel-gear-type wrist mechanisms. It may be possible to impose additional requirements on the design, which will result in a smaller number of admissible mechanism structures. Hence, we may consider these fundamental requirements as the axioms for the design of a particular class of bevel-gear-type wrist mechanisms.

Note that it is possible to construct wrist mechanisms from non-fractionated, three-DOF gear trains. For example, the wrist mechanism shown in Fig. 4.10 (page 77) is a non-fractionated three-DOF gear train. However, the structural synthesis of this type of mechanisms has been excluded from this research. The reason is that mechanisms derived from non-fractionated three-DOF gear trains are generally more complicated in construction.

<u>Example</u>

To illustrate the above design principles, we take one graph of a non-fractionated, two-DOF gear train as an example. Figure 2.2 shows that link 6, 4 and 7 are coaxial at level d, link 1, 3, and 4 are coaxial at level b. Both set of links are potential

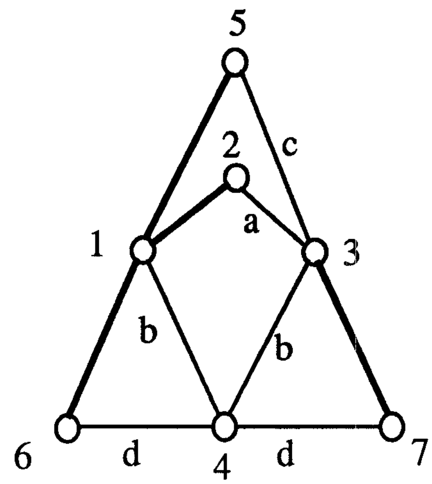

Figure 2.2 A two-DOF epicyclic gear train

candidates for input links at this stage. Using links 6, 4, 7 as input links, we may then choose link 2 or 5 as the end-effector link, since there are three edge levels in the thin-edged paths, (6-4-3-2), (7-4-3-2), (6-4-3-5), and (7-4-3-5). In addition, there are two heavy-edged paths originated from vertices 6 and 7. Hence, links 6, 4, and 7 are considered as a set of acceptable input links. Links 1, 3, and 4 are excluded from further consideration as input links since fundamental requirement **R3** can not be satisfied. Although the kinematic chain using links 6, 4, and 7 as input links satisfies the first three fundamental requirements, it still can't be considered as a qualified wrist mechanism structure. Because once we choose link 2 as the end-effector link, link 5 become a redundant link, and vice versa.

2.4 Summary

The kinematic structure of bevel-gear-type robotic wrist mechanism has been analyzed. Based on the analysis, a set of fundamental requirements of bevel-gear-type wrist mechanisms has been established. It has been shown that a three-DOF bevel-gear-type wrist mechanism can be regarded as a non-fractionated, two-DOF gear train jointed with a base link. Thus to create all bevel-gear-type wrist mechanisms, we shall first develop an atlas of non-fractionated, two-DOF epicyclic gear trains. Then these fundamental requirements will be applied to select those gear trains that are suitable for the design of wrist mechanisms. And, finally, an atlas of bevel-gear-type spherical wrist mechanisms will be developed.

Chapter 3

TOPOLOGICAL SYNTHESIS OF NON-FRACTIONATED, TWO-DEGREE-OF-FREEDOM EPICYCLIC GEAR TRAINS

3.1 Introduction

In previous chapter, it has been shown that to create all bevel-gear-type wrist mechanisms, we need to establish an atlas of non-fractionated, two-DOF epicyclic gear trains. In Chapter 3, the enumeration of the kinematic structures of non-fractionated, two-DOF epicyclic gear trains will be discussed.

Traditionally, mechanical systems are made up of closed-loop configurations which rely on a single input to drive the systems. These, so-called, one-DOF mechanisms are characterized by the fact that the configuration of the system depends on one input parameter. For each given input, the output is uniquely determined regardless of the complexity of the system. One-DOF mechanisms are by far the most common type of mechanisms, and can be found in almost every kind of machines and mechanical devices. The topological synthesis of such devices have been studied extensively [8,9,14,15,18,20,21,43,44,52,57,61,64,66,67,68].

Another group of importance is the multi-DOF systems. The characteristic of a multi-DOF system is that the configuration of the system depends on more than one input parameter. This means that these mechanisms require multiple inputs in order to derive a unique output. On the other hand, with a single input, the outputs are indeterminate. The behavior of such multi-output devices will depend on the nature of the resistance opposing the motion at each of the output shafts. Multi-DOF mechanisms can be found in adders and gear differentials for adding or subtracting motion or for torque distribution. Recently, they can also be found in robotic devices such as robotic wrists, grippers, and walking machines [3,16,58,62].

Although mechanical systems with multiple inputs or multiple outputs have existed for many years, generally, they have been used as a series of one-DOF devices rather than as non-fractionated, multi-DOF mechanisms. For example, the automotive bevel-gear differential, a two-DOF mechanism with one input and two outputs, is made up of a one-DOF gear train in series with its gear box. The second degree of freedom is simply obtained by allowing the gear train as a unit to rotate with respect to the gear box. It has been found that most of the two-DOF mechanisms enumerated in [16] and [44] belong to this type of mechanisms.

With ever increasing use of modern control theory and the demands for industrial automation and flexible manufacturing, multi-DOF mechanisms are coming into wider use, and being used in fundamentally different ways. However, the availability of such mechanisms is relatively scarce. Comparatively little is known with regard to the synthesis of such mechanisms.

In what follows, a method for the identification of non-fractionated epicyclic gear trains will be introduced and a systematic methodology for the enumeration of the topological structure of this type of mechanism will be described.

3.2 The topological structure of epicyclic gear trains

(a) Structural characteristics

The research of topological synthesis will limit to those mechanisms which obey the general mobility equation. Graphs will be used to represent the topological structure of a mechanism. The advantage of using graphs to represent the topological structures is that many of well developed theorems of graph theory can be directly applied, and systematic methodology for the structural enumeration can be automated in a computer.

We shall consider only those mechanisms which obey the basic assumptions and the fundamental rules established in the earlier papers [8,9,20,61]. According to the fundamental rules [20], the relationships among the number of thin edges, heavy-edges, and vertices for two-DOF epicyclic gear trains can be listed as shown in Table 3.1. In Table 3.1, 'n' denotes the number of vertices, 't' the number of

n	t	h
4	3	1
5	4	2
6	5	3
7	6	4
8	7	5

Table 3.1: **Number of vertices vs. number of edges for two-DOF gear trains**

thin edges, and 'h' the number of heavy edges.

In order to automate the process of mechanism creation, a vertex-vertex adjacency matrix will be used to denote the graph of a mechanism. The adjacency matrix is a symmetric matrix of order n. All the diagonal elements of the matrix are set to zero and the off-diagonal elements are set to 1, or g, or 0 according to whether vertex i is connected to vertex j by a turning pair, or a gear pair, or not at all. The thin edges can be labeled by different symbols such as a, b, c, etc. to indicate their axis locations.

(b) Rotation graph

A rotation graph is defined as the graph obtained from the graph of an epicyclic gear train by deleting all the thin edges and, then, reconnecting the end vertices of the heavy edges directly to their corresponding transfer vertices with thin edges. This definition is taken from Ravisankar and Mruthyunjaya [52] and is different from that defined by Freudenstein [20]. The vertex in a fundamental circuit which divides the thin-edge path into two parts such that thin edges on one side of the vertex are all at one level and those on the opposite side of the vertex are at a different level is call the transfer vertex [20].

(c) Pseudoisomorphic graphs

According to the fundamental rules [20], the subgraph G formed by deleting all the heavy edges from the graph of an epicyclic gear train is a tree. Furthermore, if the subgraph G contains k vertices connected together by thin edges of a common level, these vertices and their incident edges of the same level form a subtree H. From the point of view of mechanisms, vertices connected together by thin edges having a common level implies that the corresponding links in the mechanism are connected by revolute joints that share a common joint axis. Thus, it is possible to rearrange the turning pairs among these coaxial links without changing functional characteristics of the mechanism [62]. Hence any edge in the subtree H can be replaced with a new edge of the same level. The only restriction is that the resulting subgraph remains a tree. The operation of replacing an edge in the subtree H with another edge of the same level is called *vertex selection.*

Two graphs satisfying the fundamental rules of epicyclic gear trains [9] are said to be *pseudoisomorphic* if they become isomorphic under single or repeated application of vertex selection. From the above discussion, it is clear that if the graphs of two epicyclic gear trains are pseudoisomorphic, then their functional characteristics are identical.

(d) Canonical Displacement Graph

A canonical displacement graph is obtained by labeling the thin edges of a rotation graph according to their axis locations in space. Thin edges are permitted to form one or more loops in a rotation graph and its corresponding canonical displacement graph. However, all the thin edges that form a loop must share a common edge level. Hence, the number of thin edges in a rotation graph and its corresponding canonical displacement graph can exceed that given in Table 3.1 by the number of thin-edged loops.

3.3 Non-fractionated epicyclic gear trains

(a) Articulated kinematic chains

According to Table 3.1, one observes that the most elementary graph of two-DOF epicyclic gear trains is a four-link chain having three thin edges and one heavy edge. Fig. 3.1(a) shows the functional schematic of such a kinematic chain and Fig.

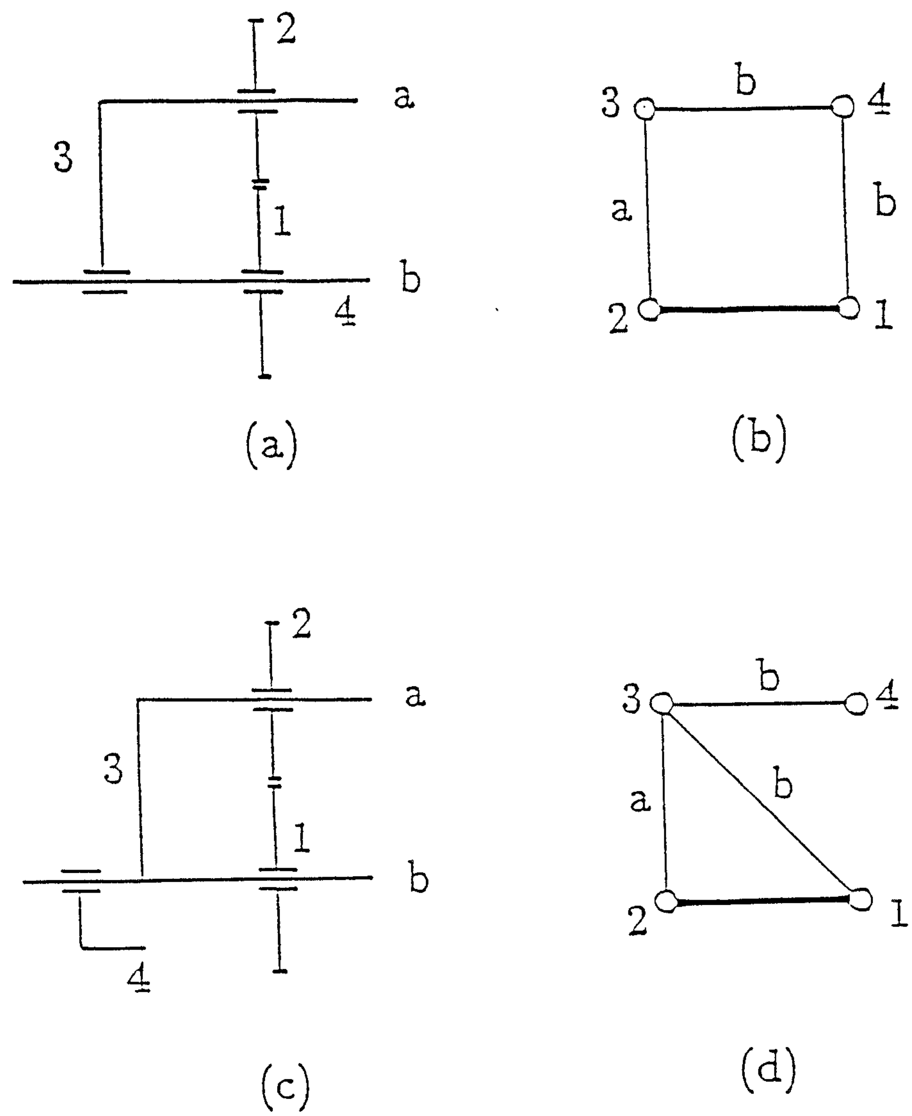

Figure 3.1 A four-link chain and its pseudoisomorphic mechanism with a cut-link

3.1(b) shows the corresponding graph. As shown in Fig. 3.1(b), thin edges 1-4 and 3-4 share a common level, *b*, which implies that links 1, 3, and 4 are coaxial. Hence, the revolute joints connecting these coaxial links can be rearranged according to the definition of vertex selection. Figure 3.1(c) shows such a rearrangement and Fig. 3.1(d) shows the corresponding graph. It is obvious that Fig. 3.1(d) is obtained by adding the 1-3 edge to and removing the 1-4 edge from the graph of Fig. 3.1(b).

An *articulation point* in a graph is a vertex whose removal increases the number of components, and a graph is a *block* if it is connected and has no articulation points [23]. The graph shown in Fig. 3.1(b) is a block but the one shown in Fig. 3.1(d) is not.

The mechanism shown in Fig. 3.1(c) consists of two kinematic chains which have one common link but no common joints. More specifically, it is made up of a three-link chain (links 1, 2, and 3) in series with a two-link chain (links 3 and 4) with link 3 as the common link. A multi-DOF kinematic chain which is made up of two or more kinematic chains with one common link but no common joints is called an *articulated kinematic chain* as opposed to a fully closed-loop kinematic chain. An articulated chain is sometimes called a fractionated chain. The common link corresponding to the articulation point in the graph is called the *cut-link* since an articulated kinematic chain can be broken into two chains by cutting the chain at the common link.

In general, a kinematic chain is considered to be articulated, if under one or repeated application of vertex selection, one of its pseudoisomorphic graphs contains one or more articulation points. The link corresponding to the articulation point serves as the common link for the two subchains. Each subchain can be a simple two-link chain or a gear train having one or multiple degrees of freedom. It can be shown that a single-DOF epicyclic gear train has no cut-link; a two-DOF epicyclic gear train has at most one cut-link; and an n-DOF epicyclic gear train has at most $n-1$ cut-links.

Although articulated kinematic chains have their own usefulness, its synthesis can usually be decoupled into that of several kinematic chains. It is quite straightforward and is not the subject of this study. In what follows, we shall concentrate on the synthesis of non-fractionated epicyclic gear train.

(b) Identification of non-fractionated, two-DOF epicyclic gear trains

A non-fractionated epicyclic gear train is defined as a kinematic chain with no cut-links. Since a labeled graph with no articulation points can sometimes be reconfigured into an articulated one, it appears that it would be necessary to apply the vertex selection procedure to a graph in as many different ways as possible in order to test the validity of a non-fractionated kinematic chain. However, a graph with k vertices connected to each other with thin edges of a common edge level can have as many as $(k)^{k-2}$ pseudoisomorphic graphs. It would be difficult, if not impossible, to derive all the pseudoisomorphic graphs as the number of edges having a common edge label increases. In the following, a simple algorithm for the detection of an articulation point in a labeled graph will be presented.

As discussed previously, the graph of an articulated two-DOF epicyclic gear train can be divided into at least two components. Each component can be a single-DOF epicyclic gear train or a simple two-link chain. When these two components are transformed into rotation graphs, the articulation point becomes the one and only vertex that belongs to both rotation graphs. In the case when one component is a two-link chain, the two-link chain does not result in a rotation graph. Therefore, the link on the outer end of the two-link chain will disappear from the rotation graph. This serves as the basis for the identification algorithm to be described below.

Step 1. For each labeled graph, construct a $k \times 3$ matrix $R(i, j)$ such that the elements in the first two columns denote the two end-vertices of a heavy edge and the element in the third column denotes the associated transfer vertex of the gear pair, where k denotes the number of gear pairs.

Step 2. If any vertex does not appear in the matrix R, then the graph itself or one of its pseudoisomorphic graphs contains an articulation point. No further checking is necessary.

Step 3. Choose m_1 rows of elements from the matrix R to form a group, G_1, and let the remaining rows of elements to form another group, G_2. Select only the distinct vertices of G_1 to form a set, S_1, and that of G_2 to form another set, S_2. If there exists one and only one element common to both sets S_1 and S_2, then the element is an articulation point of the graph. No further checking is necessary.

Step 4. Repeat step 3 by choosing different rows of elements and different number of rows of elements until all the possible combinations are tested. If no articulation points are found in all the tests, then the kinematic chain is a non-fractionated chain.

As an example, consider the contra-rotation gear train [8] shown in Fig.

3.2(a) and its graph representation shown in Fig. 3.2(b). The matrix R is given by

$$R = \begin{bmatrix} 2 & 1 & 3 \\ 4 & 2 & 3 \\ 5 & 4 & 6 \\ 7 & 5 & 6 \end{bmatrix}$$

For $m_1 = 1$, we pick one row of elements from the matrix R to form the first group, G_1, and the remaining three rows to form the second group, G_2. There are four combinations. One such combination is given by:

$$G_1 = (2, 1, 3)$$

and

$$G_2 = (4, 2, 3; 5, 4, 6; 7, 5, 6).$$

Hence,

$$S_1 = (2, 1, 3)$$

and

$$S_2 = (2, 3, 4, 5, 6, 7).$$

Since vertices 2 and 3 appear in both sets, no articulation point has been found for this combination. The search has been repeated for the other $m_1 = 1$ combinations with no success.

For $m_1 = 2$, we pick two rows of elements from the matrix R for the first group, G_1, and remaining rows of elements for the second group, G_2. There are six combinations. Because of the symmetry between G_1 and G_2, only three are distinct. We may choose, for example,

$$G_1 = (2, 1, 3; 4, 2, 3)$$

and

$$G_2 = (5, 4, 6; 7, 5, 6).$$

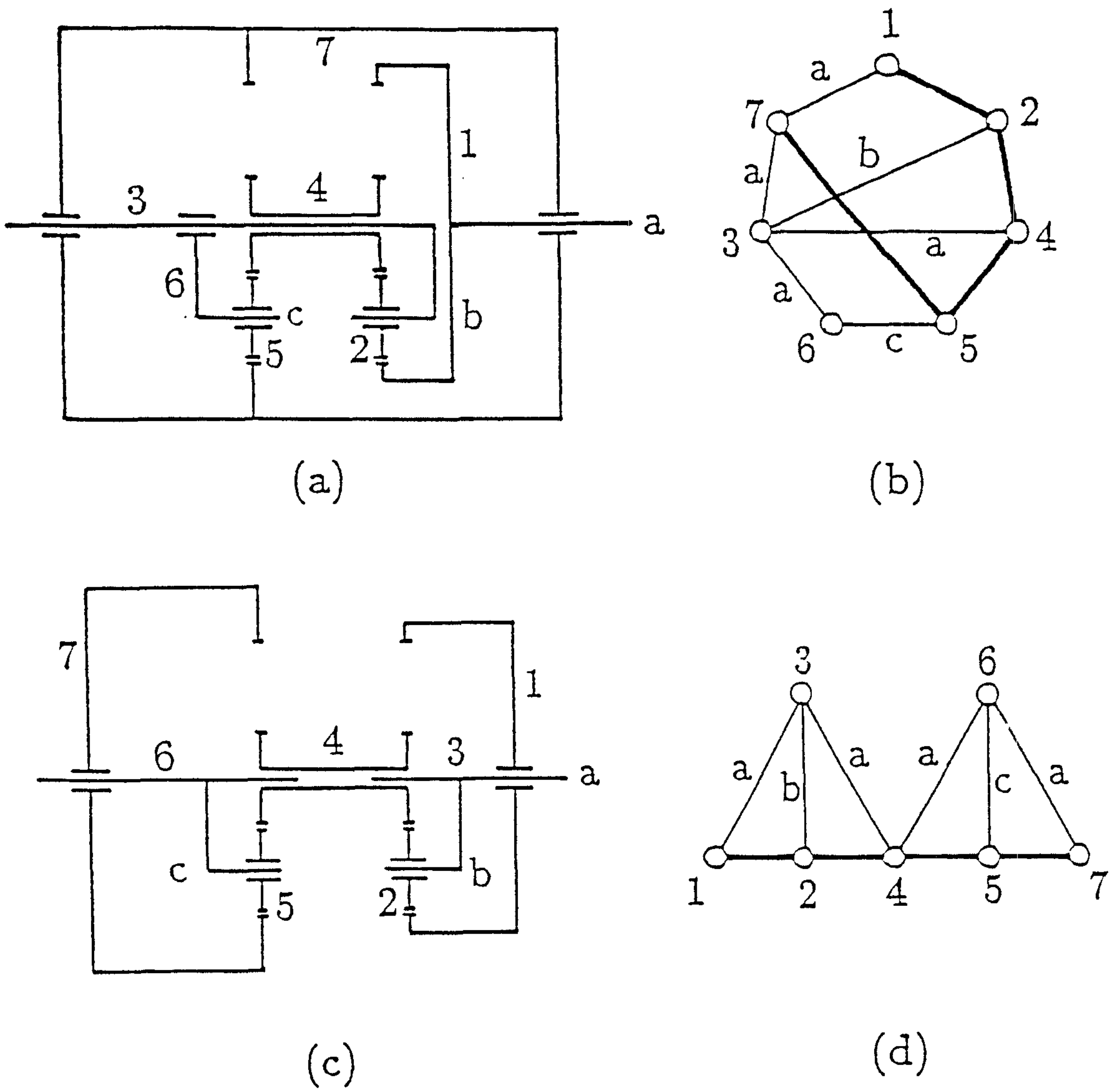

Figure 3.2 The contra-rotation gear train

Then,

$$S_1 = (1, 2, 3, 4)$$

and

$$S_2 = (4, 5, 6, 7).$$

Since, vertex number 4 is the one and only element common to both sets, S_1 and S_2, it is concluded that the mechanism contains a cut-link. Further, the vertices shown in S_1 form one kinematic chain and that in S_2 form another kinematic chain. The gear train can, therefore, be rearranged as shown in Fig. 3.2(c). Figure 3.2(d) shows the corresponding graph representation. Note that if we are to apply the vertex selection procedure, it would require up to $(5)^{5-2} = 125$ vertex selections in order to identify the articulation point.

3.4 Methods of enumeration

Buchsbaum and Freudenstein [9] developed an atlas of unlabeled graphs for mechanisms with up to six links. This atlas was subsequently modified by Mayourian and Freudenstein [43] based on the restrictions governing the graphs of kinematic chains. Such an atlas can be used as a basis for the creation of mechanisms. First, those graphs which satisfy the relationship listed in Table 3.1 are selected. Then, for each of the admissible unlabeled graph, we can label it in as many structurally distinct ways as possible in accordance with the fundamental rules of epicyclic gear trains. Mayourian [44] carried out this process and obtained a number of two-DOF epicyclic gear trains with up to six links. However, a careful examination of those mechanisms revealed that most of them belong to articulated kinematic chains. The method works well for simple mechanisms. But, as the number of links increases, the process of labeling the edges becomes quite complicated.

Another possible method of enumeration is by combining two single-DOF kinematic chains. One link from each of the two single-DOF kinematic chain can be rigidly coupled together to form a two-DOF kinematic chain. Thus, an m-link chain combined with an n-link chain results in an $(m+n-1)$-link chain. In fact, most of the existing two-DOF epicyclic gear trains are synthesized this way. However, this type of mechanisms always contains the coupling link as a cut-link.

One additional link is needed to form a non-fractionated, two-DOF epicyclic gear train. The additional link is to be connected to the above fractionated kinematic chain with a turning pair on one side and with a gear pair on the opposite side of the cut-link. Further, the link to be connected to the additional link with a turning pair must also serve as the gear carrier. For example, Fig. 3.3(a) shows the graph of a two-DOF epicyclic gear train with a cut-link. It is obvious that the graph of Fig. 3.3(a) is derived from the combination of two single-DOF epicyclic gear trains. Figure 3.3(b) shows the graph of a non-fractionated, two-DOF epicyclic gear train obtained by adding the vertex 7 to the graph of of Fig. 3.3(a). This method seems to work. However, it does not ensure the identification of all the non-fractionated, two-DOF epicyclic gear trains. It also lacks the proof of completeness.

Recently, Tsai [61] developed a generic approach based on the fundamental rules of epicyclic gear trains. In his approach, the process starts with the most elementary graphs of interest, known as the generic graphs, and increases the complexity of the kinematic chain by adding one vertex at one time. The process is similar to the conventional method of gear-train design, where the designer begins with a rather simple gear train and increases the complexity by adding one gear at a time. Each time he adds a new gear, he adds not only a gear mesh to the mecha-

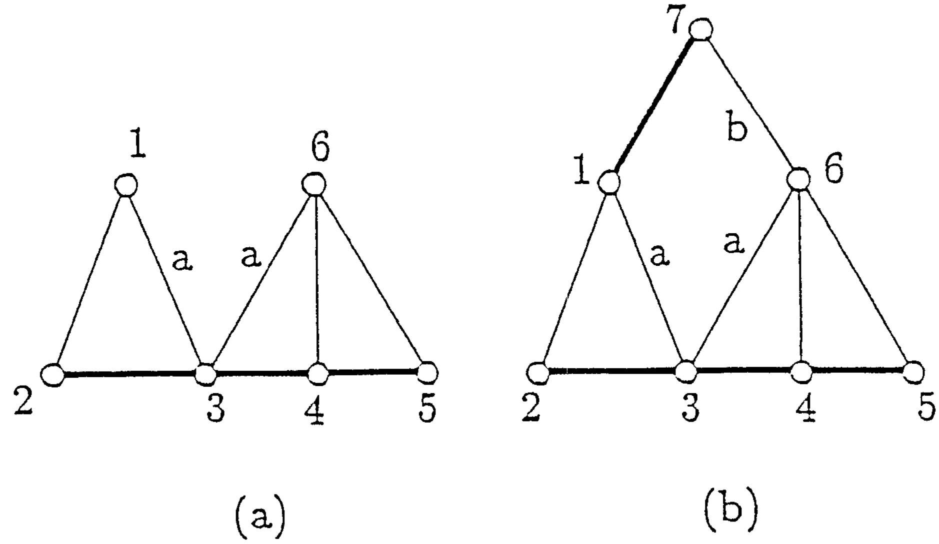

Figure 3.3 The creation of a non-fractionated, two-DOF gear train

nism but also a revolute joint to support the gear. Hence, a family of mechanisms can be generated systematically. The procedure has been successfully automated by Tsai [61] for the enumeration of one-DOF epicyclic gear trains with up to six links. In what follows, this methodology shall be modified for the enumeration of non-fractionated, two-DOF epicyclic gear trains.

From Table 3.1, the most elementary graph of two-DOF epicyclic gear trains is a four-link chain having three thin edges and one heavy edge as shown in Fig. 3.1(b). However, it has been shown earlier that its pseudoisomorphic graph, Fig. 3.1(d), contains an articulation point. The questions remaining to be answered are: Shall we use this four-link chain as the generic graph? Or, shall we find the most elementary graphs of non-fractionated epicyclic gear trains first and, then, use them as the generic graphs for the enumeration of graphs of higher complexity?

It has been shown earlier that a non-fractionated chain can be constructed by adding a gear to a fractionated kinematic chain,. Hence, we should start with the graph of four-link chain and increase the complexity by adding one vertex at a time. Using this approach, graphs with and without articulation points will be created simultaneously. The systematic procedure can be summarized as follows:

Step 1. Start with the generic graphs of n-link chains to enumerate the graphs of $(n+1)$-link chains. The generic graphs of n-link chains are defined as a set of non-isomorphic rotation graphs which may contain an articulation point.

Step 2. Enumerate all the unlabeled graphs of $n+1$ vertices for each generic graph. This can be accomplished by connecting a new vertex to one of the existing vertices with a thin edge and to any one of the remaining vertices with a heavy edge. There are $n(n-1)$ possible combinations.

Step 3. Determine if the new graph is an admissible rotation graph. First, identify the transfer vertices of the graph. Since the transfer vertices of the generic portion are already known, it is only necessary to check the newly created fundamental circuit [20]. There are three possibilities: (i) If there is only one transfer vertex in the new fundamental circuit and the transfer vertex is adjacent to the newly added vertex, the graph is retained as an admissible graph. (ii) If there is only one transfer vertex , but the transfer vertex is not adjacent to the new vertex, the graph is rejected. Under this condition, the graph can always be reconfigured into one of the graphs enumerated in category (i) above. And (iii) if there are multiple transfer vertices in the new fundamental circuit, the graph is rejected due to violation of the fundamental rules.

Step 4. Check for rotational isomorphism. Once the transfer vertices of each admissible graph are identified, the corresponding rotation graph is constructed and compared with previously enumerated graphs for rotational isomorphism. This can be accomplished by comparing their linkage characteristic polynomials [61]. If the graph is isomorphic with a previous one, it is discarded. If not, it is kept as new rotation graph of $n+1$ vertices. Note that if the rotation graph contains an isolated point, then the point may be connected to any other vertex with a thin edge. The only restriction is that the thin edge must be labeled with one of its adjacent edge levels.

Step 5. Detect articulation points using the algorithm described in the previous section. If no articulation points are found, the kinematic chain is identified as a non-fractionated epicyclic gear train.

Step 6. Label the thin edges of the rotation graph in as many different ways as possible to obtain a set of canonical displacement graphs. In the rotation graph, if there exists a loop formed by thin edges only, then these thin edges must share one edge level.

Step 7. Check for displacement isomorphism. Here it is only necessary to compare with those graphs having the same rotation graph. Ravisankar and Mruthyunjaya's method [52] can be used to test displacement isomorphism. Different edge levels $a, b, c, \ldots$ are denoted by different numbers $1, 2, 3, \ldots$, etc. These numbers are then assigned to the corresponding elements in the linkage adjacency matrix. Since the symbols (numbers) have no practical meaning, they can be interchanged without altering the structure of a mechanism. We can permute the labels in all possible ways and compare the linkage characteristic polynomials. If one such permutation results in an polynomial identical with another, then they are isomorphic in labeling.

Step 8. Repeat steps 2 to 7 until all the generic graphs of n vertices have been used.

3.5 Graphs enumeration

Using the above systematic procedure, all the graphs of two-DOF epicyclic gear trains with up to seven links have been enumerated. The following illustrates the sequence of enumeration.

(a) Four-link chain

As stated earlier the most elementary graph for two-DOF epicyclic gear trains is the four-link chain shown in Fig. 3.1(d). The corresponding epicyclic gear train is shown in Fig. 3.1(c).

(b) Five-link chains

Figure 3.1(d) is used as the generic graph. There are $4 \times 3 = 12$ possible ways of adding a vertex to the graph of four-link chain. Figures 3.4(a) and 3.4(b) show two such possibilities, where 1 to 4 represent the vertices of the generic graph and 5 represents the added vertex.

Let the levels of edges 2-3, 3-4, and 3-1 be 'a', 'b', and 'b', respectively. Then, it becomes clear that the newly added fundamental circuits for the graphs of Figs. 3.4(a) and 3.4(b) are circuits 1-5-2-3-1, and 1-5-3-1, respectively. The corresponding transfer vertices are both vertex 3. Since the transfer vertex in Fig. 3.4(a) is not adjacent to the new vertex, 5, it is rejected. However, the transfer vertex in Fig. 3.4(b) is adjacent to the new vertex. Hence, the graph shown in Fig. 3.4(b) is accepted as an admissible graph. We note that the 5-2 edge in Fig. 3.4(a) must be labeled as 'a' while the 5-3 edge in Fig. 3.4(b) can be labeled as 'a' or 'c'. Further, the graph shown in Fig. 3.4(a) can be reconfigured into the one shown in Fig. 3.4(b). This is the reason why the unlabeled graph of Fig. 3.4(b) has been accepted as an admissible rotation graph while the one shown in Fig. 3.4(a) is rejected.

At this point there is no need to check for graph isomorphism, since this is the first rotation graph enumerated. Applying the algorithm for checking the articulation point, it can be shown that the graph shown in Fig. 3.4(b) contains an articulation point. Note that the 3-4 edge in Fig. 3.4(b) can also be labeled as 'a'.

All the twelve combinations of graphs have been constructed and tested.

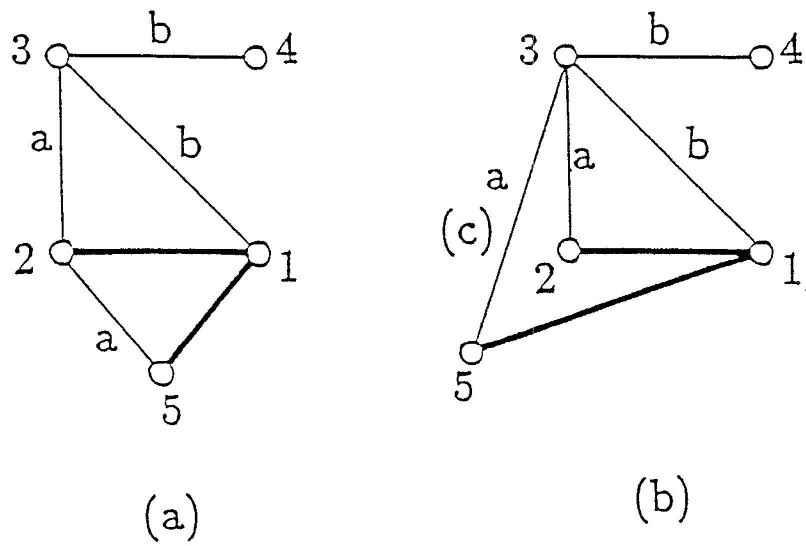

Figure 3.4 Two graphs derived from Fig. 3.1(d), but only one is admissible.

There are five non-isomorphic rotation graphs and ten canonical displacement graphs. The results are shown in Table 3.2, where the first and second columns of the g matrix represent the vertex number of a gear pair and the third represents the corresponding transfer vertex; the second and third columns of the t matrix represent the vertex numbers of a turning pair, and the first one represents the corresponding edge label. The articulation point in each graph is also shown in Table 3.2. Note that there are five non-isomorphic rotation graphs and ten canonical displacement graphs. All of them contain an articulation point. However, all the five non-isomorphic rotation graphs have been kept as the generic graphs for the enumeration of six-link chains.

	Rotation Graphs g	Edge Labels t	Articulation Point
1	$\begin{bmatrix} 2 & 1 & 3 \\ 5 & 1 & 3 \end{bmatrix}$	$\begin{bmatrix} 1 & 3 & 2 \\ 2 & 3 & 1 \\ 2 & 4 & 3 \\ 1 & 5 & 3 \end{bmatrix}$ $\begin{bmatrix} 1 & 3 & 2 \\ 2 & 3 & 1 \\ 2 & 4 & 3 \\ 3 & 5 & 3 \end{bmatrix}$ $\begin{bmatrix} 1 & 3 & 2 \\ 2 & 3 & 1 \\ 1 & 4 & 3 \\ 1 & 5 & 3 \end{bmatrix}$ $\begin{bmatrix} 1 & 3 & 2 \\ 2 & 3 & 1 \\ 1 & 4 & 3 \\ 3 & 5 & 3 \end{bmatrix}$	3
2	$\begin{bmatrix} 2 & 1 & 3 \\ 5 & 1 & 4 \end{bmatrix}$	$\begin{bmatrix} 1 & 3 & 2 \\ 2 & 3 & 1 \\ 2 & 4 & 1 \\ 3 & 5 & 4 \end{bmatrix}$	1
3	$\begin{bmatrix} 2 & 1 & 3 \\ 5 & 3 & 1 \end{bmatrix}$	$\begin{bmatrix} 1 & 3 & 2 \\ 2 & 3 & 1 \\ 2 & 4 & 3 \\ 3 & 5 & 1 \end{bmatrix}$ $\begin{bmatrix} 1 & 3 & 2 \\ 2 & 3 & 1 \\ 1 & 4 & 3 \\ 3 & 5 & 1 \end{bmatrix}$	3
4	$\begin{bmatrix} 2 & 1 & 3 \\ 5 & 3 & 4 \end{bmatrix}$	$\begin{bmatrix} 1 & 3 & 2 \\ 2 & 3 & 1 \\ 2 & 4 & 3 \\ 3 & 5 & 4 \end{bmatrix}$	3
5	$\begin{bmatrix} 2 & 1 & 3 \\ 5 & 4 & 3 \end{bmatrix}$	$\begin{bmatrix} 1 & 3 & 2 \\ 2 & 3 & 1 \\ 2 & 4 & 3 \\ 1 & 5 & 3 \end{bmatrix}$ $\begin{bmatrix} 1 & 3 & 2 \\ 2 & 3 & 1 \\ 2 & 4 & 3 \\ 3 & 5 & 3 \end{bmatrix}$	3

Table 3.2: **Two-DOF five-link chains**

(c) Six-link chains

Using the five non-isomorphic rotation graphs of five vertices as the generic graphs, eighteen (18) non-isomorphic rotation graphs of six-link chains have been enumerated. However, only two were identified as blocks which resulted in three canonical displacement graphs as shown in Fig. 3.5.

(d) Seven-link chains

Using the eighteen non-isomorphic rotation graphs of six vertices as the generic graphs, twenty blocks which resulted in fifty canonical displacement graphs have been enumerated as shown in Fig. 3.6. These graphs can be used to construct non-fractionated, two-DOF epicyclic gear trains of seven links.

For the purpose of illustration, a typical epicyclic gear train is also sketched for each of the graphs shown in Figs. 3.5 and 3.6.

3.6 Some design guidelines

Each graph shown in Figs. 3.5 and 3.6 can be converted into non-fractionated epicyclic gear trains, and these gear trains can be designed to possess planar, spherical, or spatial motion. Buchsbaum and Freudenstein gave detailed procedure for the construction of mechanisms [9].

The potential usefulness of a two-DOF epicyclic gear train depends on which link is held fixed and which links are assigned as the input and/or output links. Although the construction of such mechanisms depends highly on the ingenuity of a designer, some general guidelines can be established for the selection of graphs.

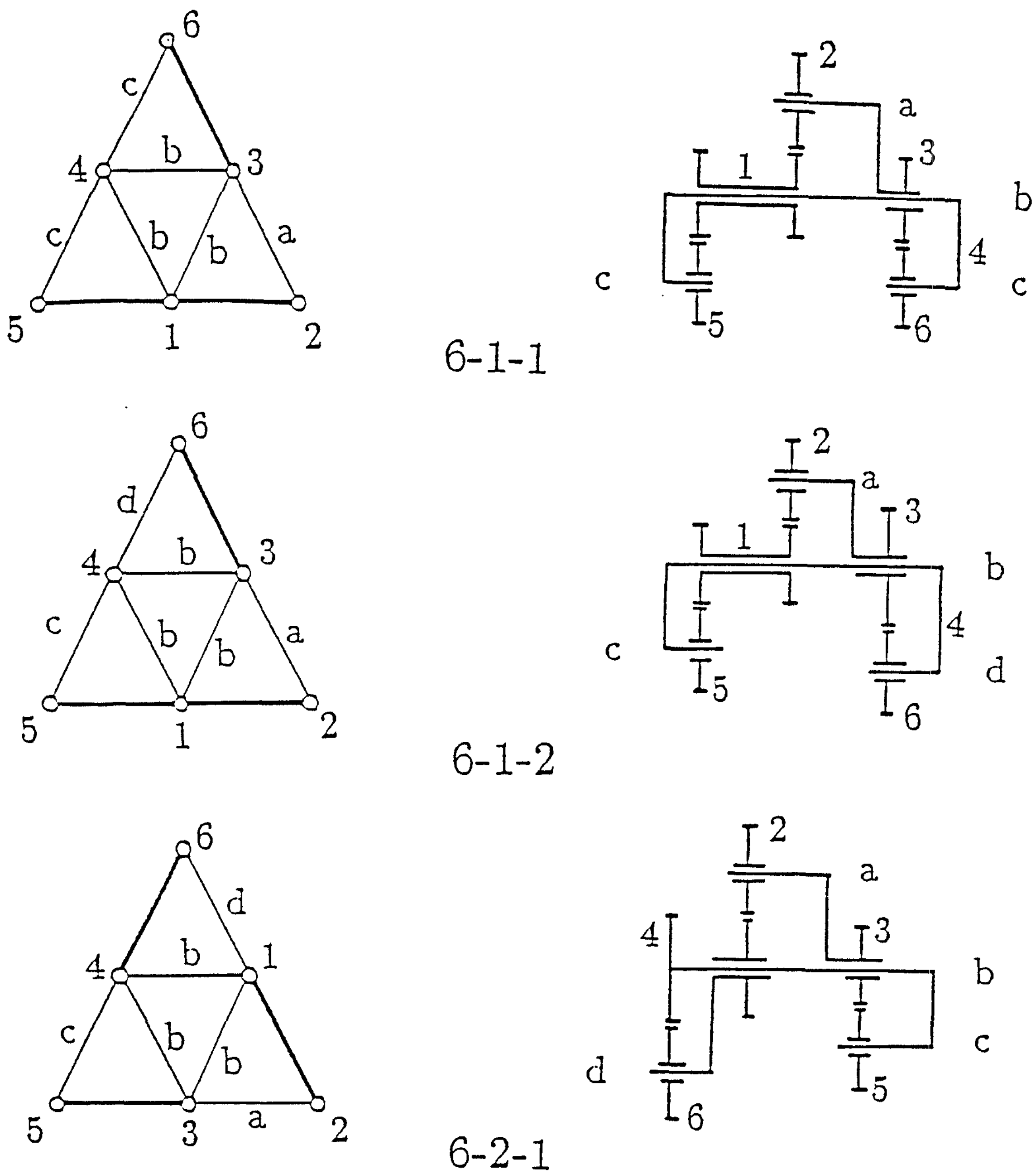

Figure 3.5 Six-link epicyclic gear trains

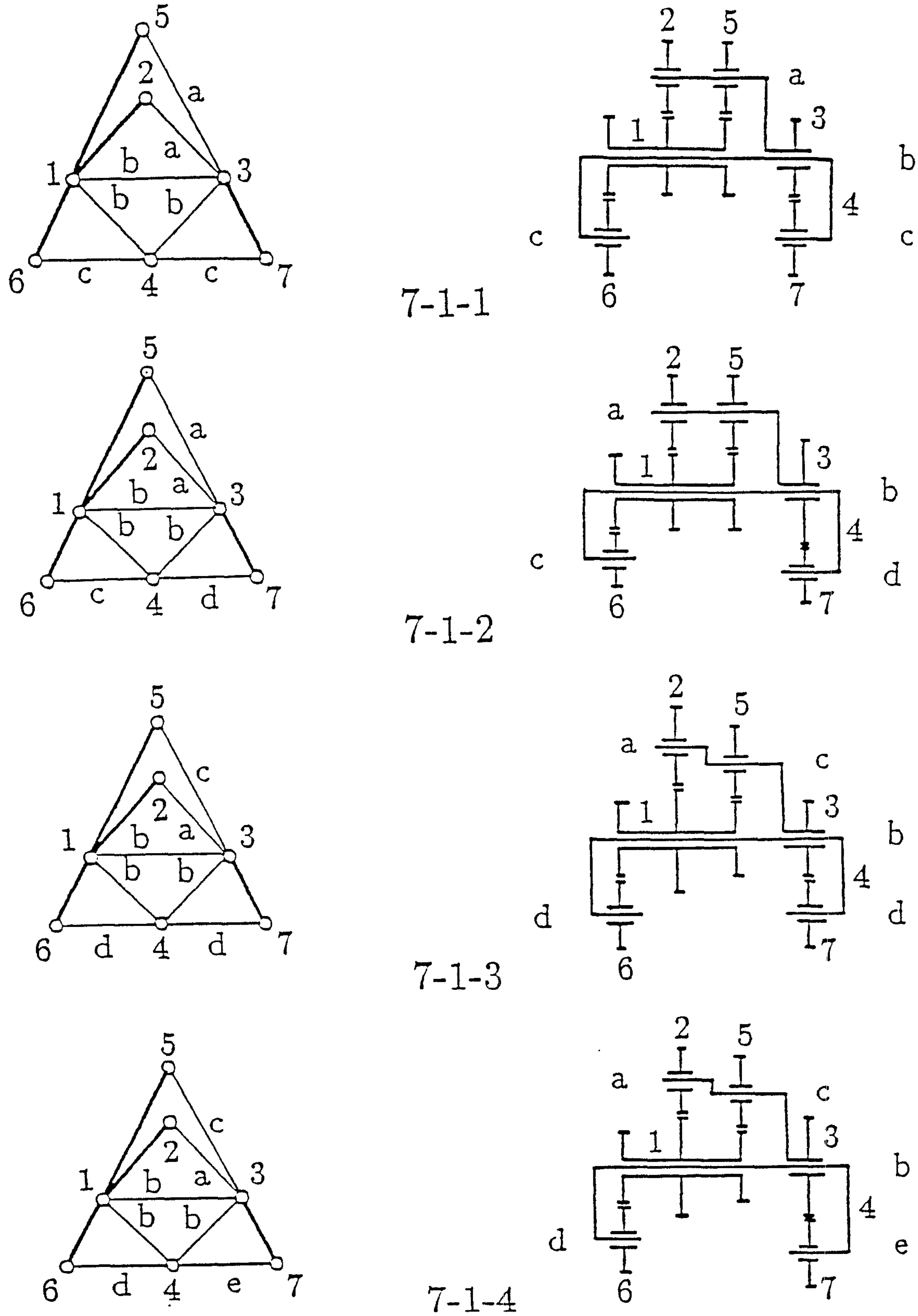

Figure 3.6 Seven-link epicyclic gear trains

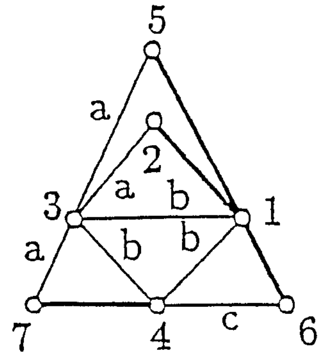

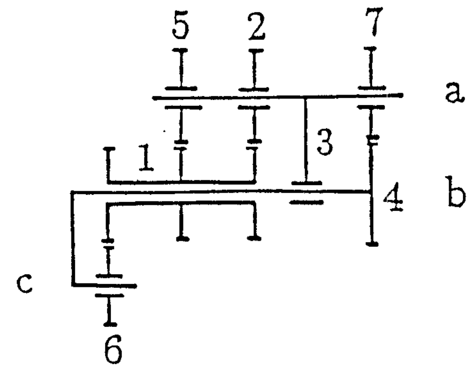

7-2-1

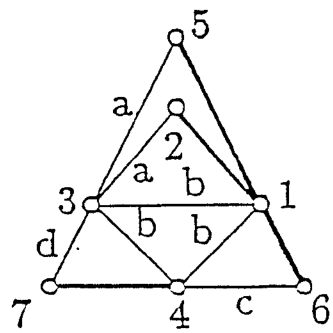

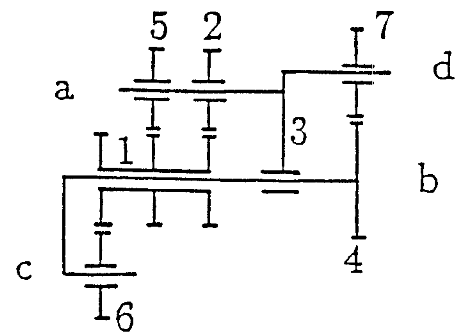

7-2-2

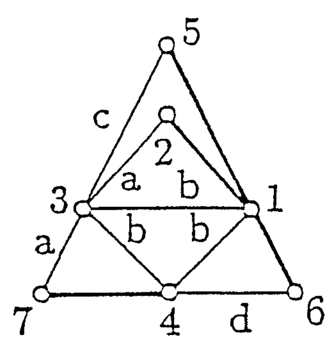

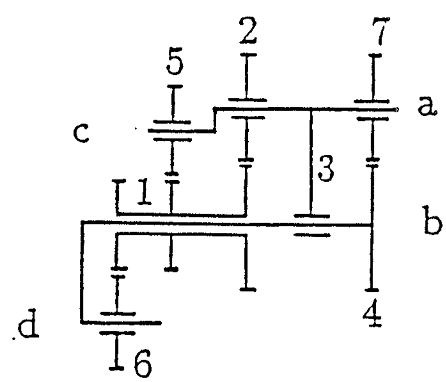

7-2-3

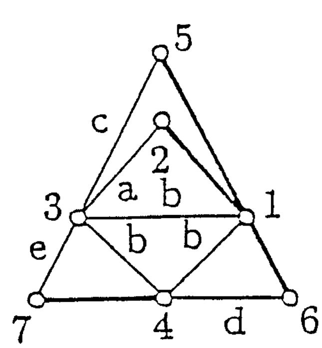

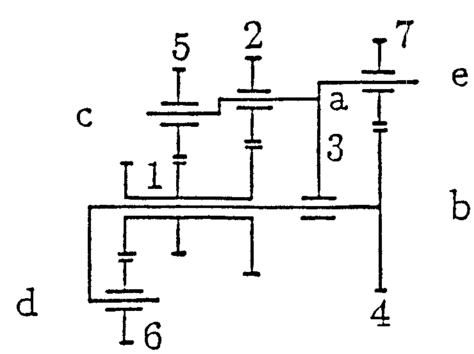

7-2-4

Figure 3.6 (Continued)

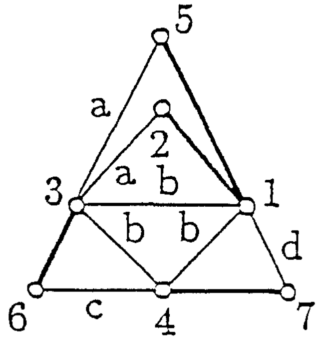

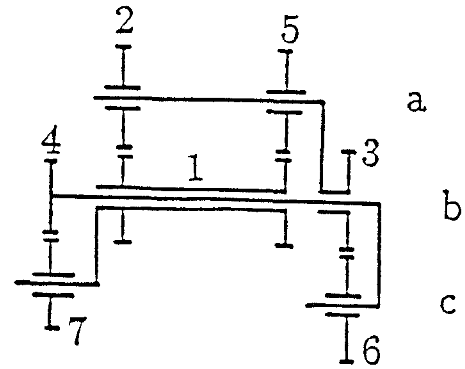

7-3-1

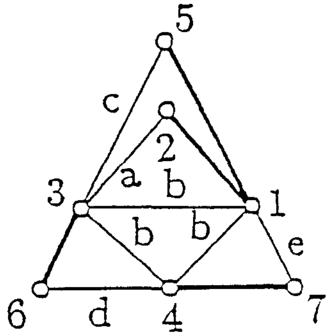

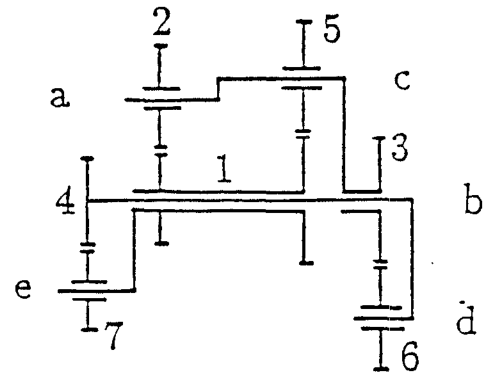

7-3-2

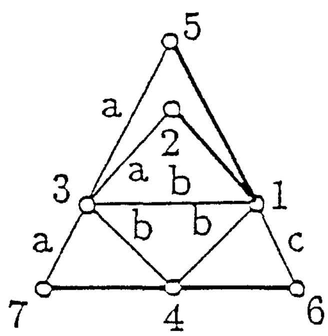

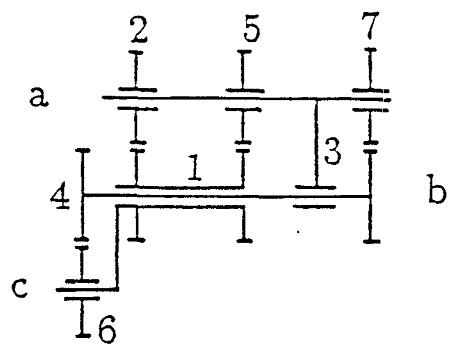

7-4-1

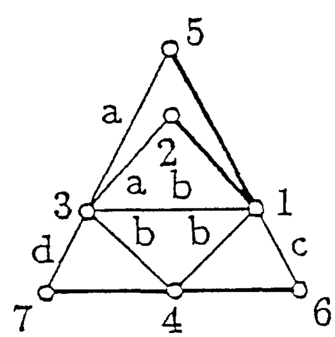

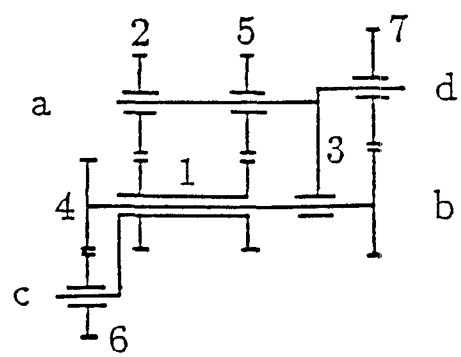

7-4-2

Figure 3.6 (Continued)

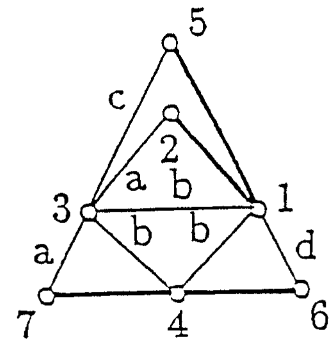

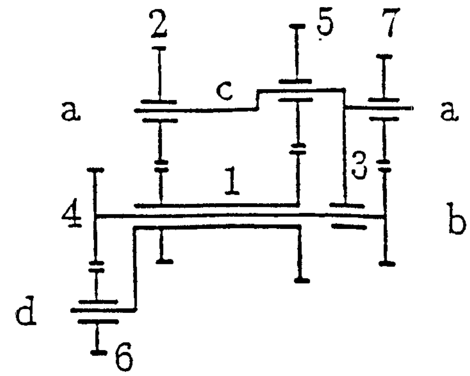

7-4-3

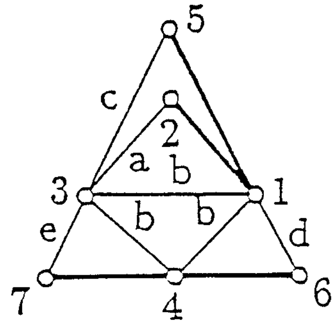

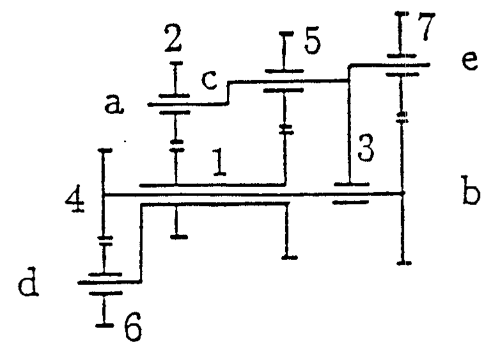

7-4-4

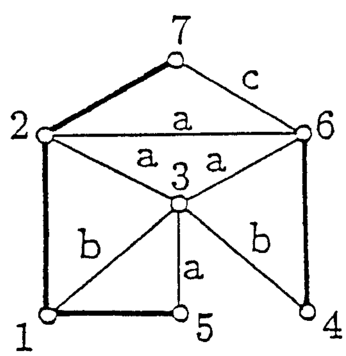

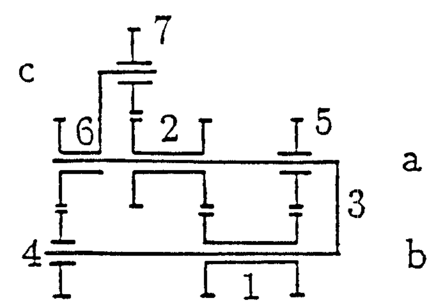

7-5-1

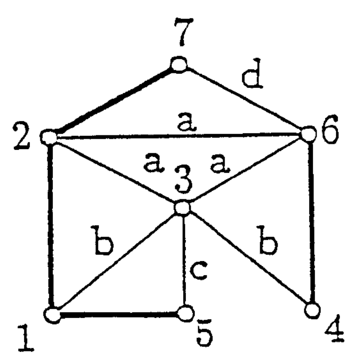

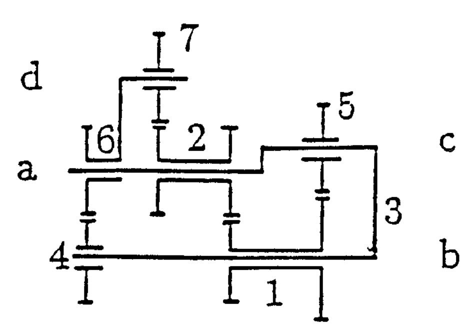

7-5-2

Figure 3.6 (Continued)

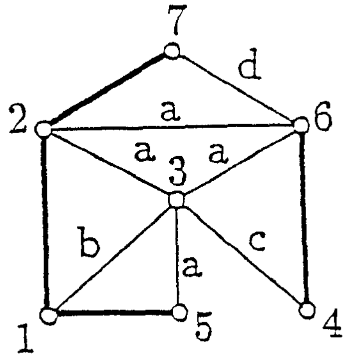

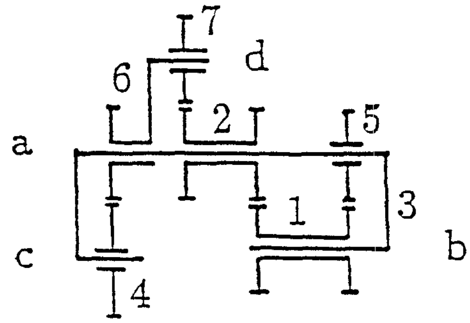

7-5-3

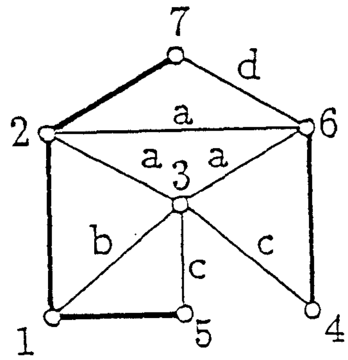

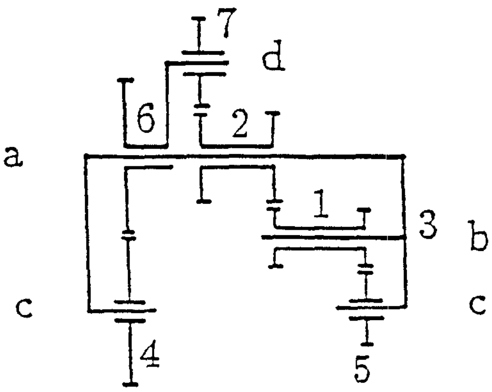

7-5-4

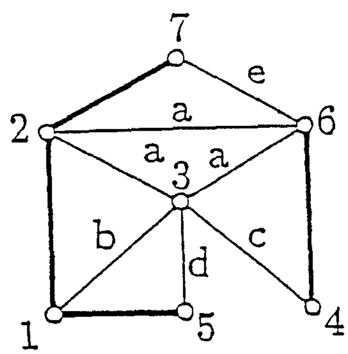

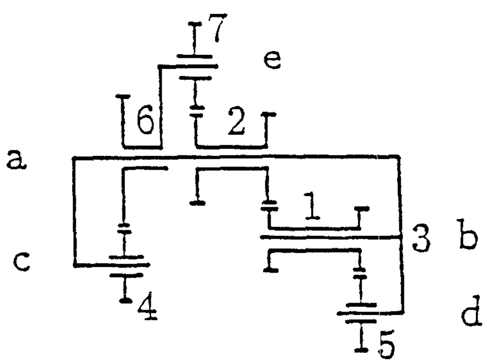

7-5-5

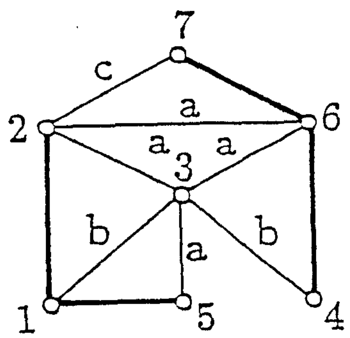

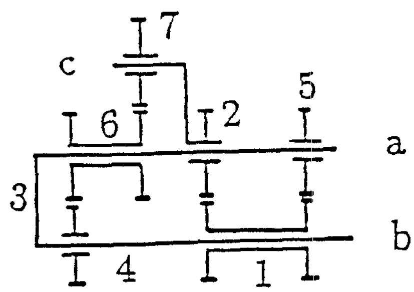

7-6-1

Figure 3.6 (Continued)

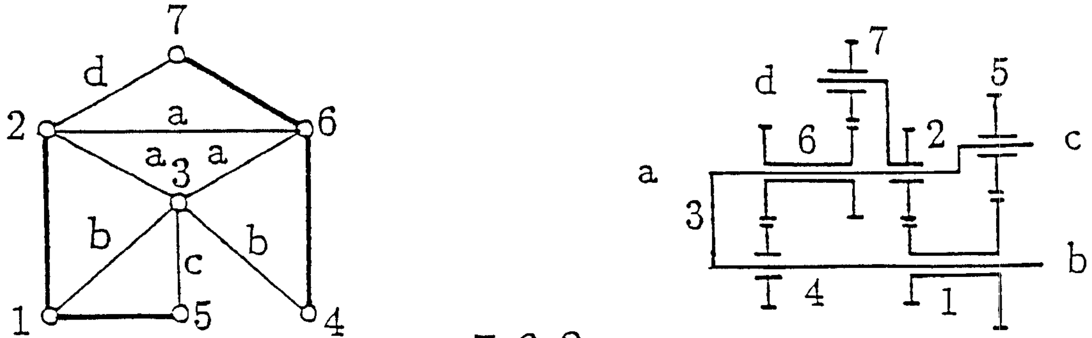

7-6-2

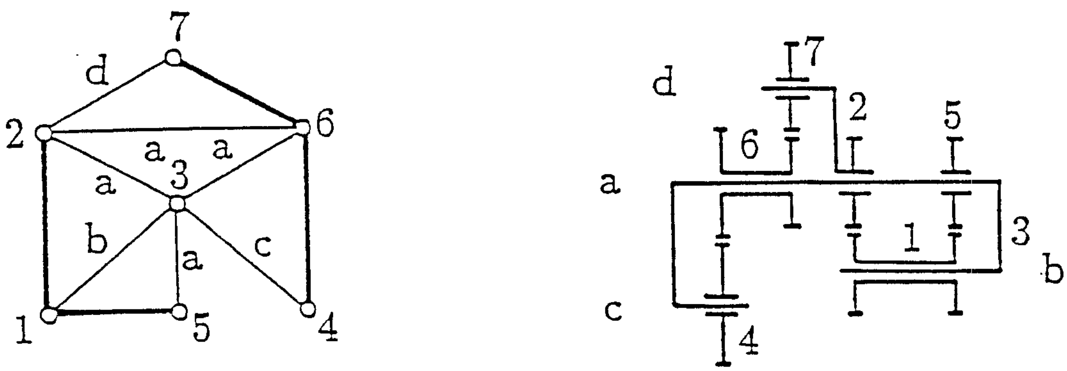

7-6-3

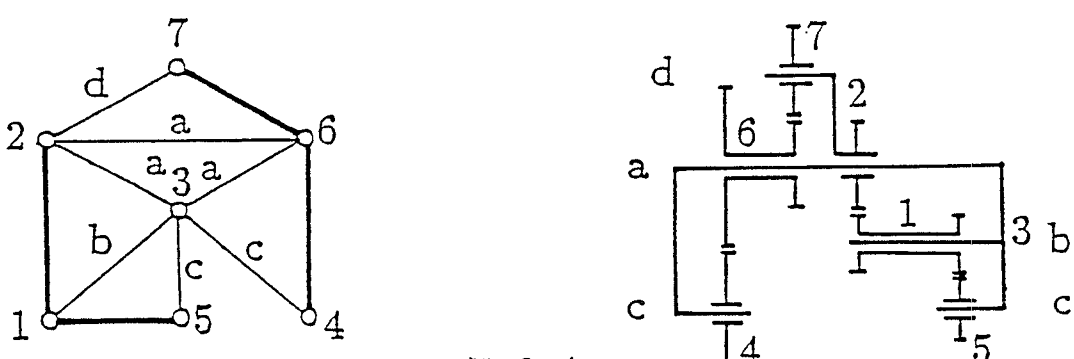

7-6-4

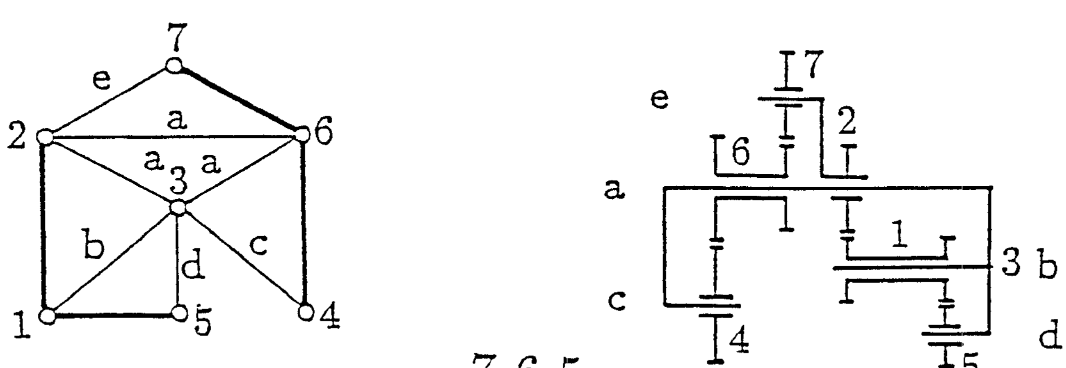

7-6-5

Figure 3.6 (Continued)

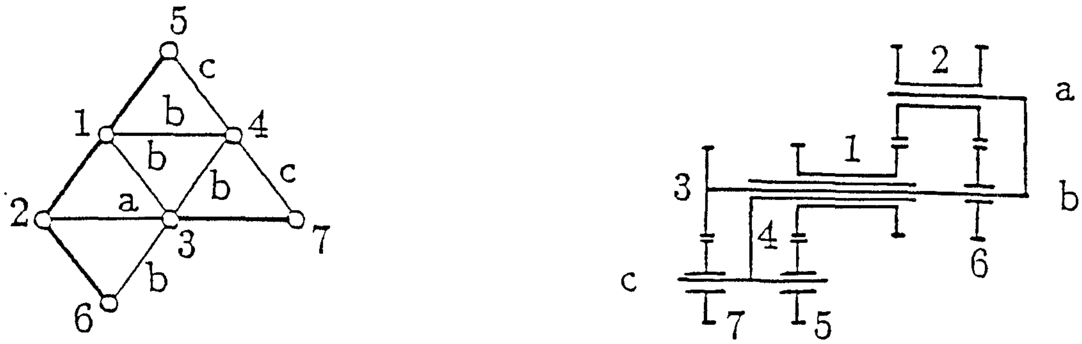

7-7-1

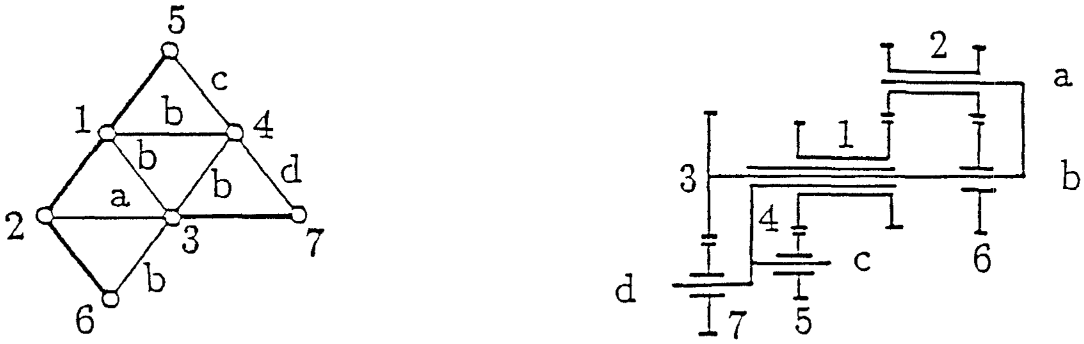

7-7-2

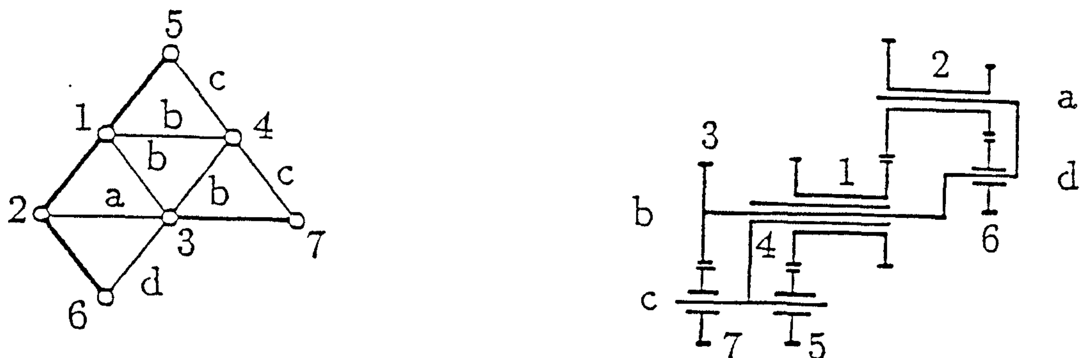

7-7-3

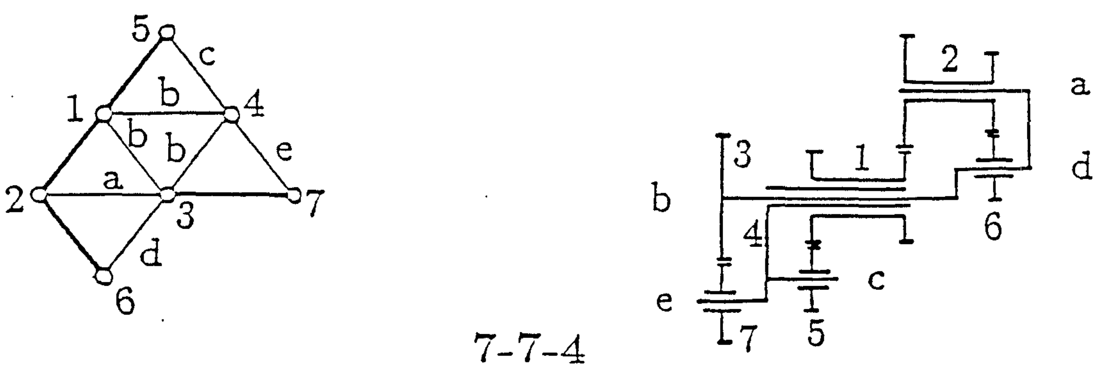

7-7-4

Figure 3.6 (Continued)

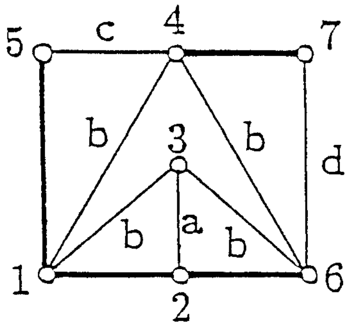

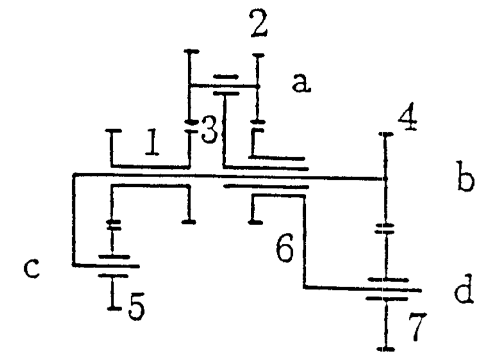

7-8-1

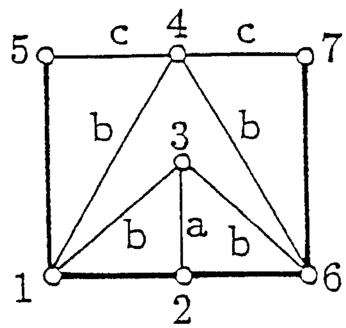

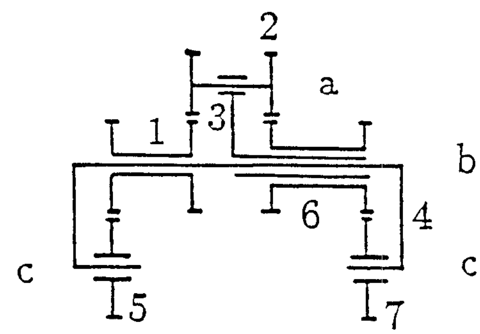

7-9-1

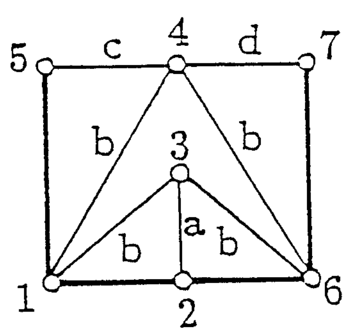

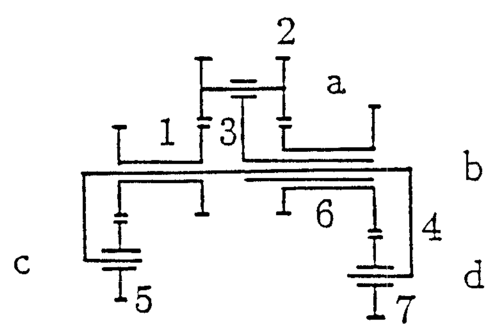

7-9-2

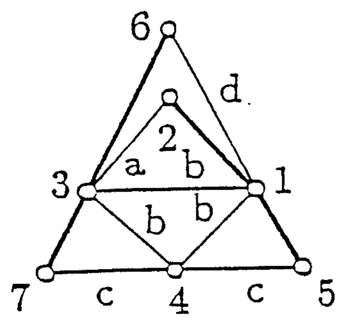

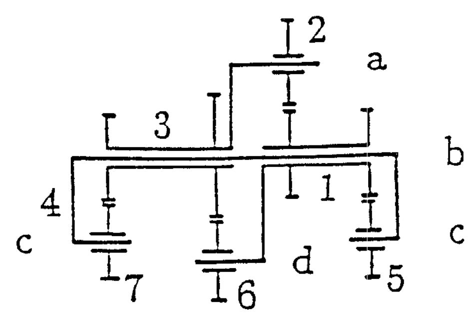

7-10-1

Figure 3.6 (Continued)

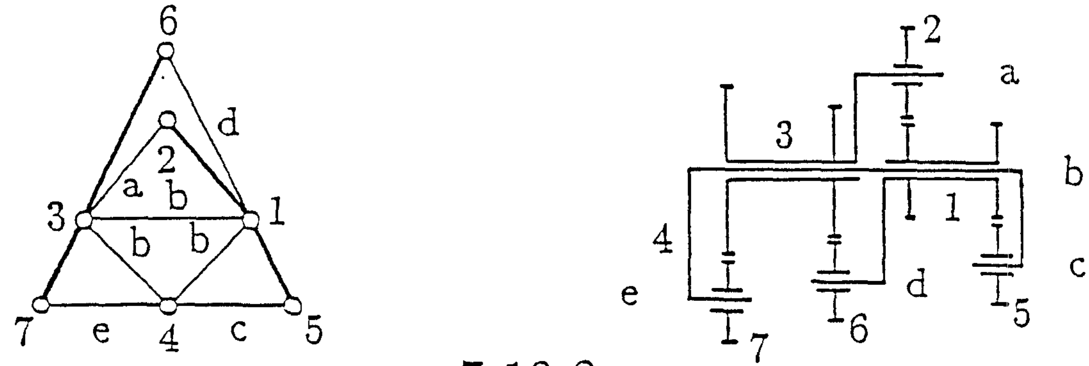

7-10-2

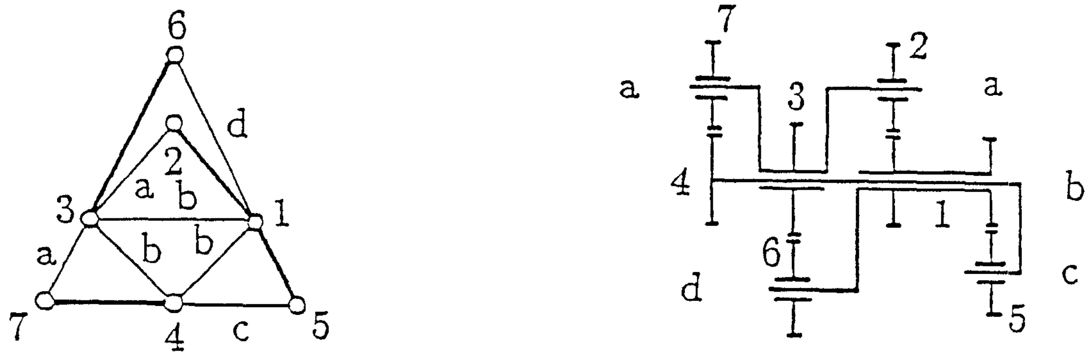

7-11-1

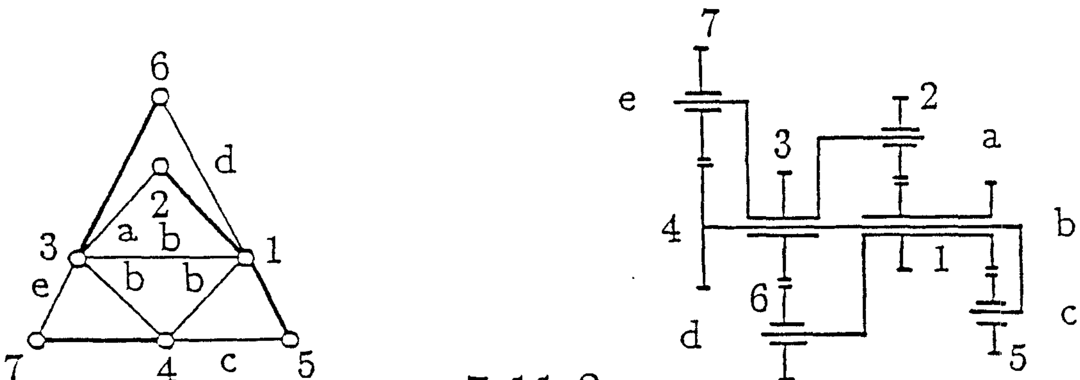

7-11-2

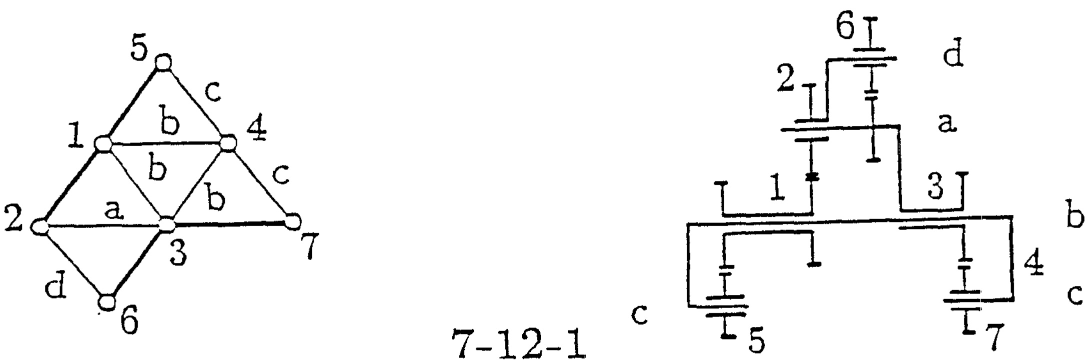

7-12-1

Figure 3.6 (Continued)

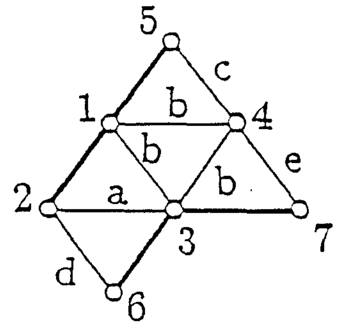

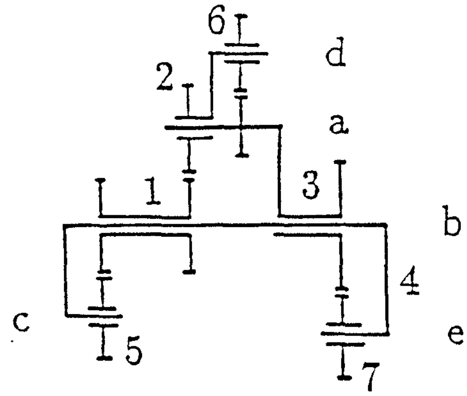

7-12-2

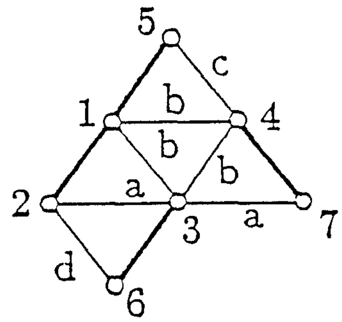

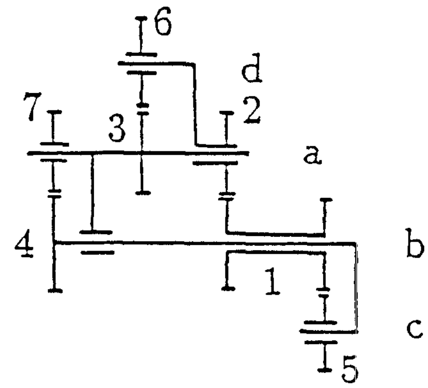

7-13-1

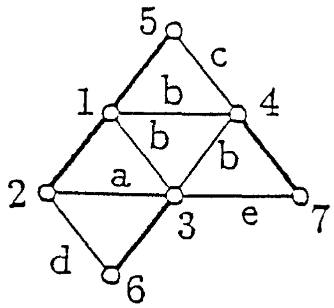

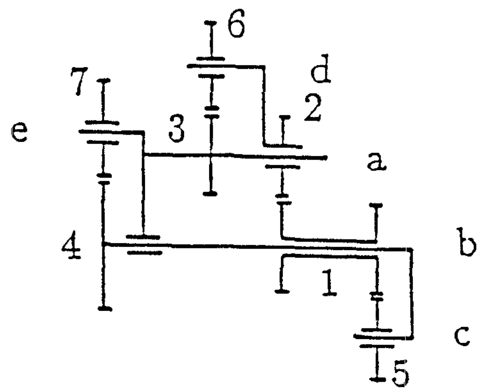

7-13-2

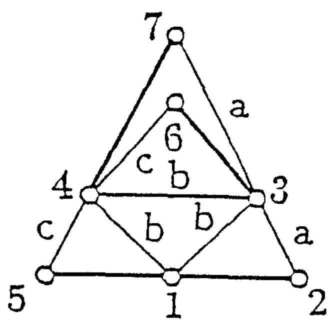

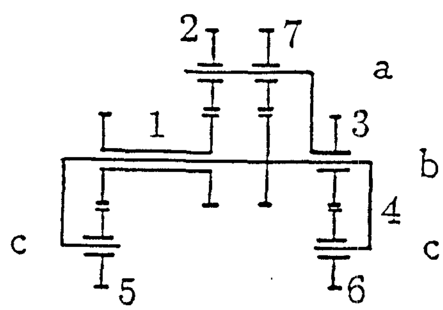

7-14-1

Figure 3.6 (Continued)

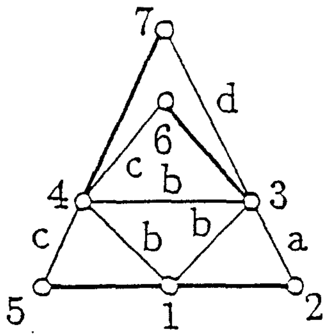

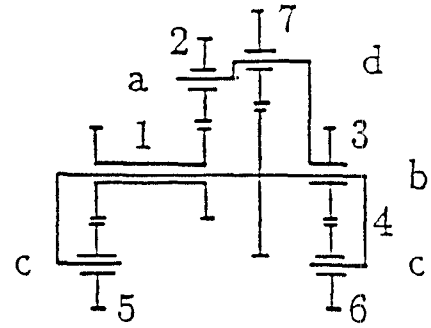

7-14-2

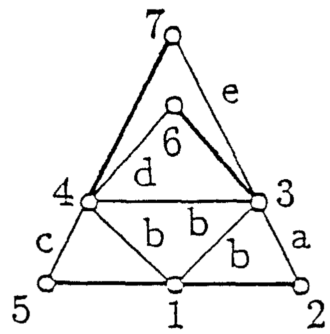

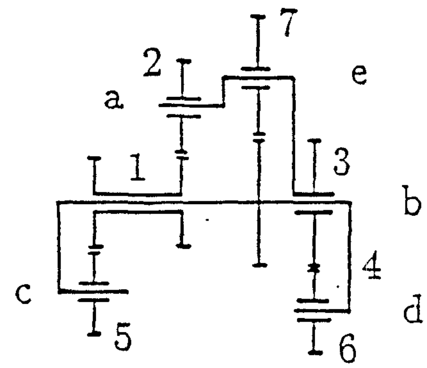

7-14-3

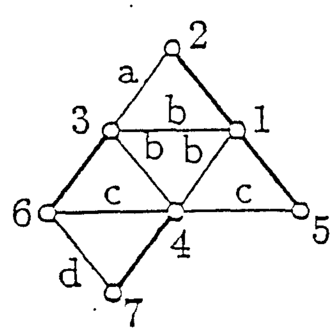

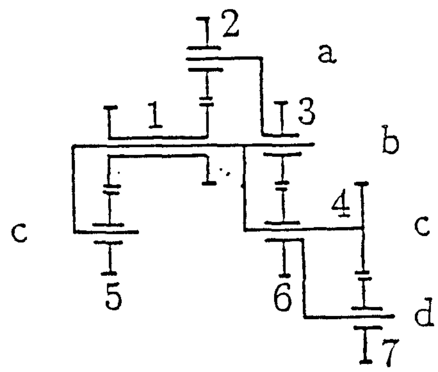

7-15-1

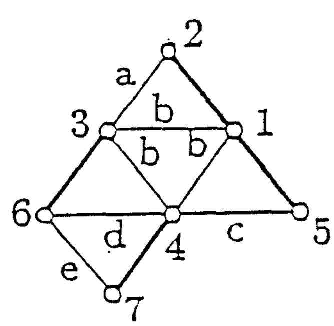

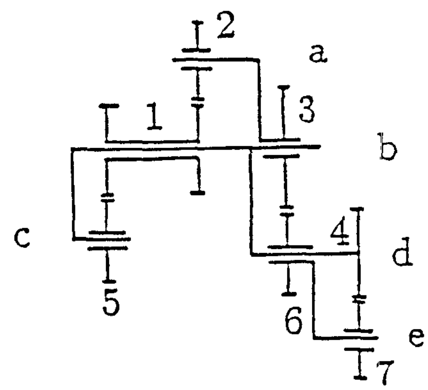

7-15-2

Figure 3.6 (Continued)

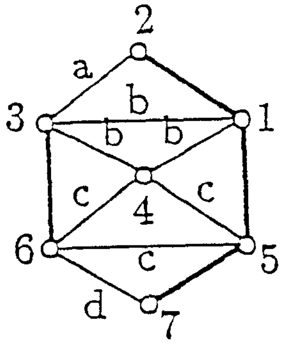
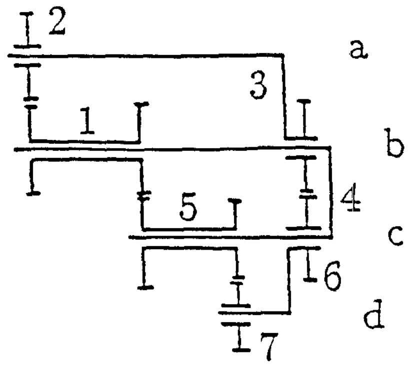

7-16-1

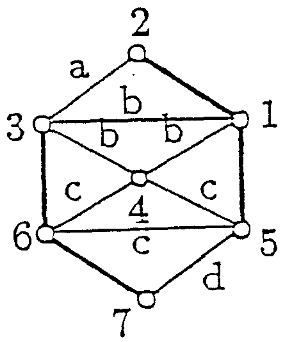
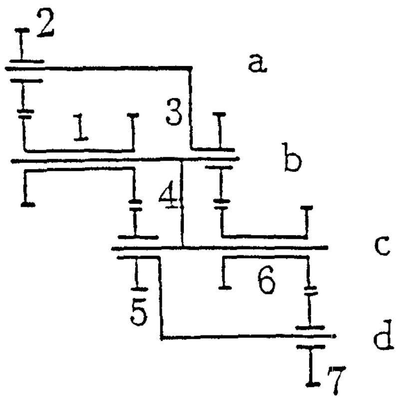

7-17-1

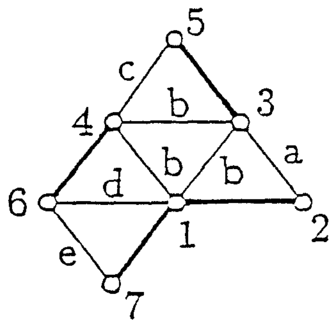
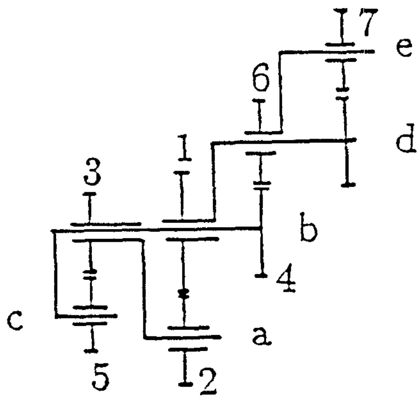

7-18-1

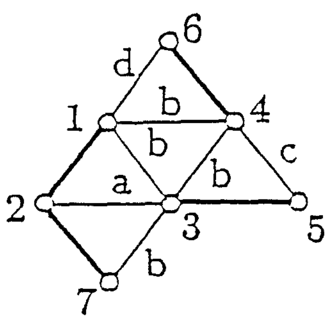
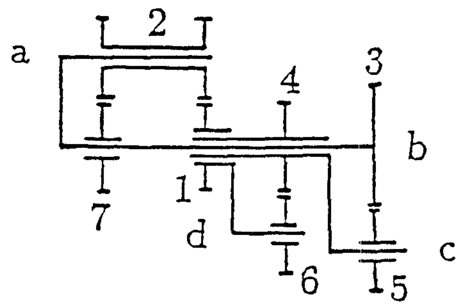

7-19-1

Figure 3.6 (Continued)

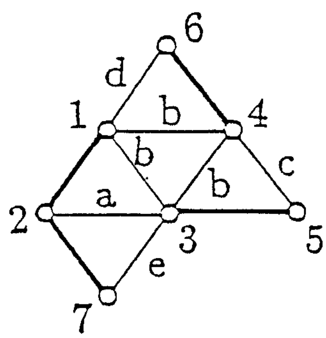

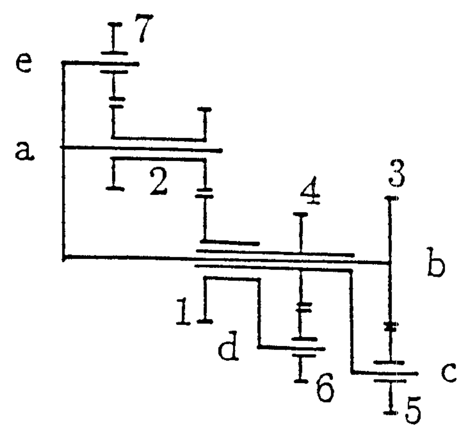

7-19-2

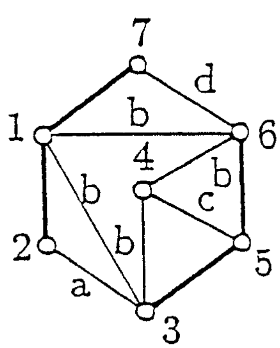

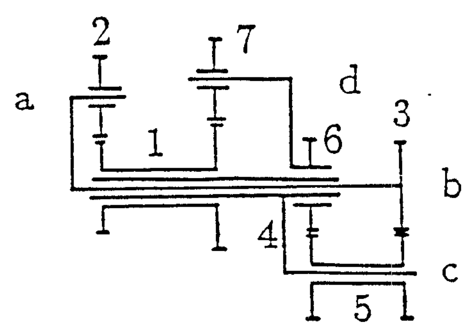

7-20-1

Figure 3.6 (Continued)

In general, it is preferred to have input actuators ground connected. Hence, for a two-input system, the ground link must contain at least two revolute joints. Furthermore, it is also desirable to have no redundant gears. A redundant gear is one that can be taken out of a mechanism without affecting its function. Following these guidelines, graphs that are applicable for the design of two-input devices have been identified as shown in Table 3.3. One possible choice of the fixed link, input links, and output link for each candidate graph is also shown in Table 3.3 for the purpose of illustration.

3.7 Summary

A systematic methodology has been developed for the enumeration of non-fractionated, two-DOF epicyclic gear trains. It has been shown that there are no non-fractionated, two-DOF epicyclic gear trains with five or less links. For six-link chains, there are two blocks which have been labeled into three canonical displacement graphs. For seven-link chains, there are twenty blocks which have been labeled into fifty canonical displacement graphs. A typical epicyclic gear train is sketched for each of the graphs for the purpose of illustration. Graphs which have potential applications in two-input devices have also been pointed out. This atlas will be used for structural synthesis of robotic wrist mechanisms to be explored in the next chapter.

Figure No.	Fixed Link	Input Links	Output Link
6-1-1	5	4, 6	2
6-1-2	4	5, 6	2
7-2-1	2	5, 7	6
7-4-1	2	5, 7	6
7-5-1	3	4, 5	7
7-5-2	3	4, 5	7
7-5-3	3	4, 5	7
7-5-4	3	4, 5	7
7-5-5	3	4, 5	7
7-6-1	3	4, 5	7
7-6-2	3	4, 5	7
7-6-3	3	4, 5	7
7-6-4	3	4, 5	7
7-6-5	3	4, 5	7
7-7-1	7	4, 5	6
7-7-2	4	5, 7	6
7-7-3	4	5, 7	6
7-7-4	4	5, 7	6
7-8-1	4	3, 5	7
7-9-1	5	4, 7	2
7-9-2	4	3, 5	7
7-12-1	5	4, 7	6
7-12-2	4	5, 7	6
7-13-1	2	6, 7	5
7-15-1	6	5, 7	2
7-16-1	6	4, 7	2
7-17-1	5	4, 7	2
7-20-1	3	2, 4	7

Table 3.3: **Graphs which have potential applications**

Chapter 4

THE DEVELOPMENT OF AN ATLAS OF BEVEL-GEAR-TYPE SPHERICAL WRIST MECHANISMS

4.1 Introduction

In this chapter, the fundamental requirements of a bevel-gear-type wrist mechanism will be applied to the non-fractionated, two-DOF gear trains derived from Chapter 3. Then all the admissible kinematic structures of bevel-gear-type, spherical wrist mechanisms will be identified and categorized.

4.2 Development of the atlas

All the graphs of non-fractionated, two-DOF gear chains with up to eight links have been analyzed. A computer program has been written to test the first three requirements listed in Chapter 2. Those graphs which satisfy **R1** to **R3** are then further examined to identify the existence of redundant links. If a graph satisfies all the fundamental requirements, then it is an admissible graph, and wrist mechanisms can be constructed by adding a base link.

For each admissible graph, a base link is jointed with one of the three coaxial input links to form a three-DOF mechanism. Since a mechanism containing three or more coaxial links can have multiple graph representations known as pseudoisomorphic graphs, it is helpful to redraw the graphs in canonical forms [61]. In the canonical graph representation, all the thin-edged paths originated from the base link have distinct edge labels, and the equivalent open-loop chain is defined as the thin-edged path starting from the base link and ending at the end-effector link. In what follows, thin edges in the equivalent open-loop chain will be labeled in an alphabetic order, a, b, c,..., etc. Labels such as m and n which are not in the same alphabetic order as a, b,..., represent axes which are not coaxial with any of the joint axes in the equivalent open-loop chain. Figures 4.1 through 4.5 show the canonical graphs from which all the possible bevel-gear-type wrist mechanisms with up to nine links can be constructed.

It has been shown [11] that for each bevel-gear-type wrist mechanism, there is a unique *structure matrix*, A, describing the relation between the angular velocities of the input links and the joint angular velocities of the equivalent open-loop chain. That is,

$$\dot{\phi} = A\dot{\theta} \tag{4.1}$$

Where $\dot{\phi}$ is the angular velocity vector of the input links, and

$\dot{\theta}$ is the joint velocity vector of the equivalent open-loop chain.

Note the structure matrix A defined in this dissertation is the transpose of that defined in [11].

The matrix A is a $n \times n$ square matrix if the number of articulation points

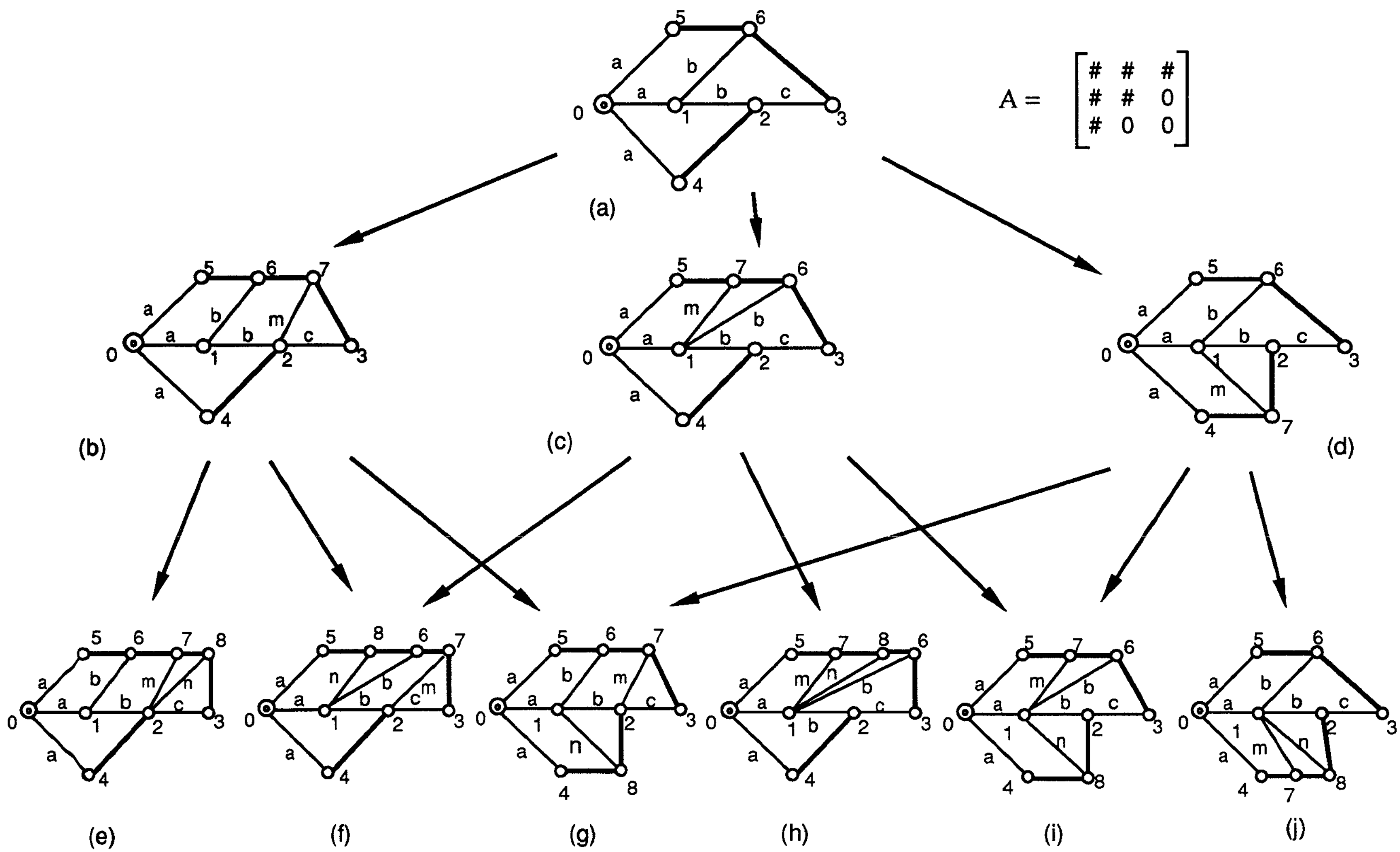

$$A = \begin{bmatrix} \# & \# & \# \\ \# & \# & 0 \\ \# & 0 & 0 \end{bmatrix}$$

Figure 4.1 The graphs of wrist mechanisms with three articulation points

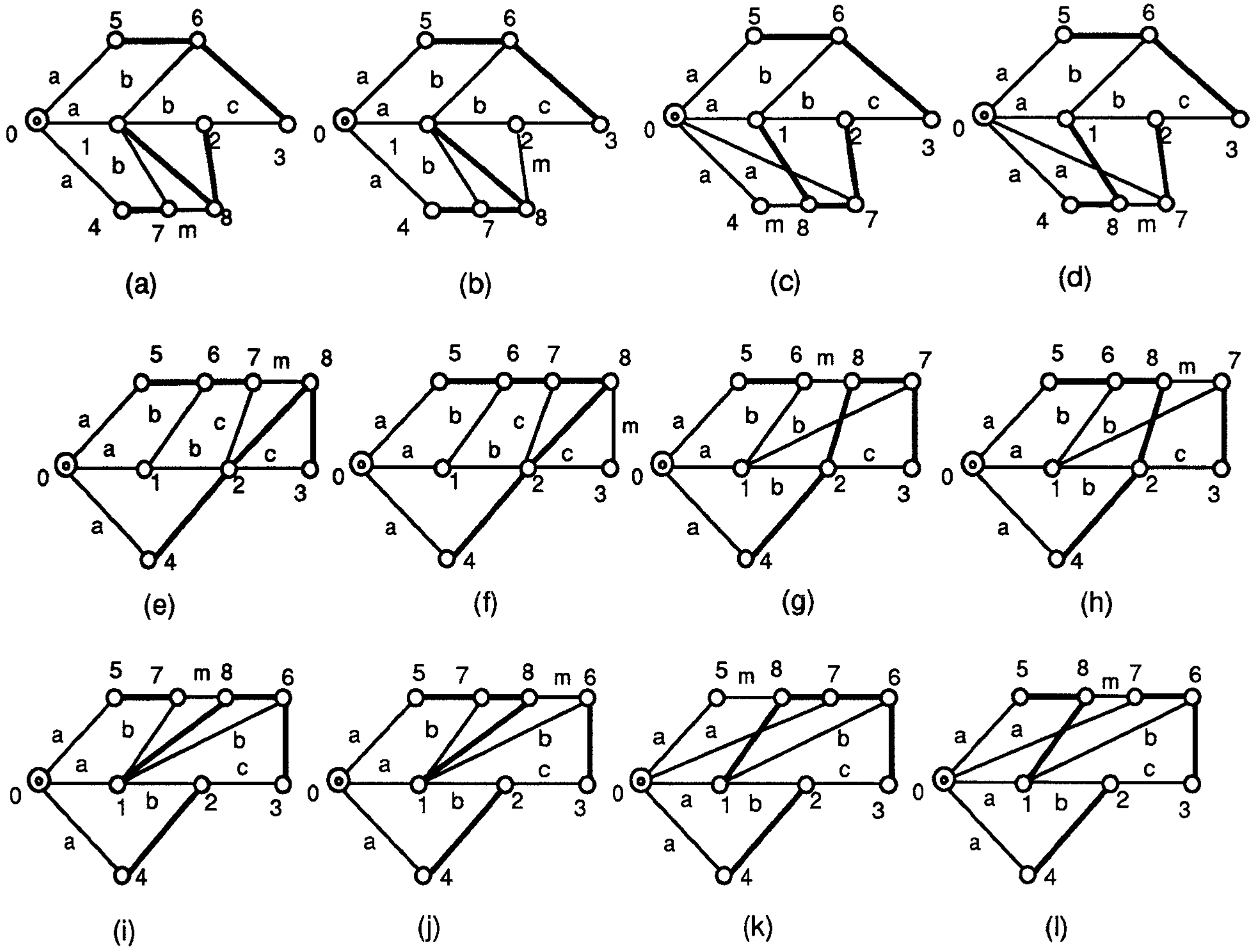

$$A = \begin{bmatrix} \# & \# & \# \\ \# & \# & 0 \\ \# & 0 & 0 \end{bmatrix}$$

Figure 4.2 The graphs of wrist mechanisms with three articulation points

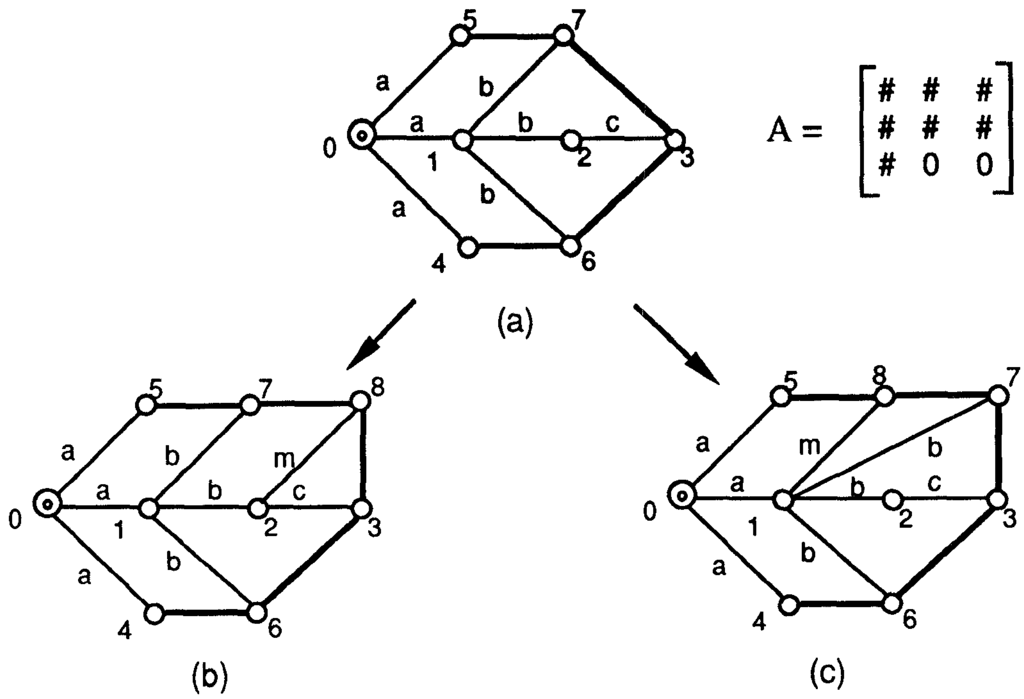

Figure 4.3 The graphs of wrist mechanisms with three articulation points

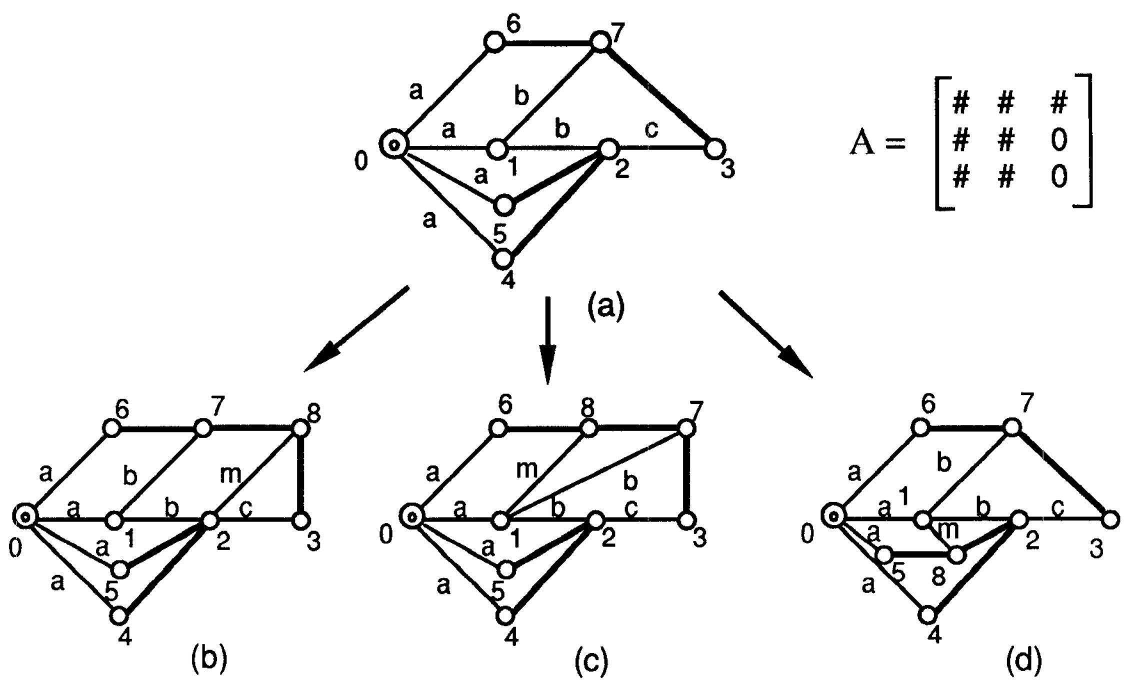

Figure 4.4 The graphs of wrist mechanisms with three articulation points

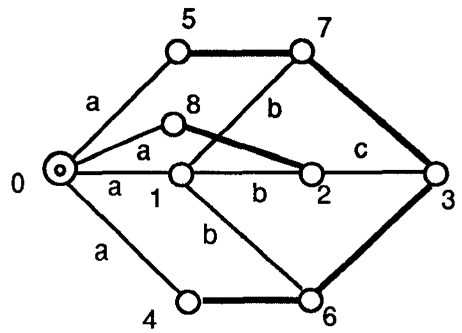

$$A = \begin{bmatrix} \# & \# & \# \\ \# & \# & \# \\ \# & \# & 0 \end{bmatrix}$$

Figure 4.5 The graphs of wrist mechanisms with three articulation points

in the mechanism is equal to the number of degrees of freedom, n. For example, the input-output relations for the Cincinnati-Milacron 3-roll wrist, Figure 2.1(b), is given by:

$$\begin{bmatrix} \dot{\theta}_{61} \\ \dot{\theta}_{71} \\ \dot{\theta}_{21} \end{bmatrix} = \begin{bmatrix} 1 & N_{56} & N_{45}N_{56} \\ 1 & N_{37} & 0 \\ 1 & 0 & 0 \end{bmatrix} \begin{bmatrix} \dot{\theta}_{21} \\ \dot{\theta}_{32} \\ \dot{\theta}_{43} \end{bmatrix} \tag{4.2}$$

where $\dot{\theta}_{ij} = \dot{\theta}_i - \dot{\theta}_j$ and $N_{ij} = N_i/N_j$ is the gear ratio. Note that the sign of each matrix element depends on the gear meshes and the definitions of link coordinate systems, and has been ignored here.

The canonical graphs have been categorized by the type of structure matrices and by the number of links. Figures 4.1 through 4.5 each shows a family of canonical graphs having the same structure matrix. Note that the '# ' sign in the structure matrix denotes a non-zero element. Figure 4.6 shows the graphs of wrist mechanisms which have more than three articulation points. Graphs in the lower level of each figure are obtained by adding an idler gear to the corresponding graph of one higher level, and the arrows are used to express their relationship. Note that the graph in the top level is called the basic mechanism, while the others are called the derived mechanisms [11].

Figure 4.1(a) is the canonical graph representation of the Cincinnati-Milacron 3-roll wrist mechanism, which has the least number of links. Figure 4.1(b) is the graph of the PUMA wrist mechanism. We note that the PUMA wrist mechanism is constructed by adding an idler gear between links 6 and 3 of the 3-roll wrist mechanism. However, they both possess the same type of structure matrix.

Although the graphs shown in Fig. 4.2 have the same type of structure matrix as that shown in Fig. 4.1, yet they are listed in a different category due to

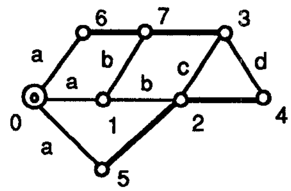

$$A = \begin{bmatrix} \# & \# & \# & 0 \\ \# & \# & 0 & 0 \\ \# & 0 & 0 & 0 \\ 0 & 0 & \# & \# \end{bmatrix}$$

(a)

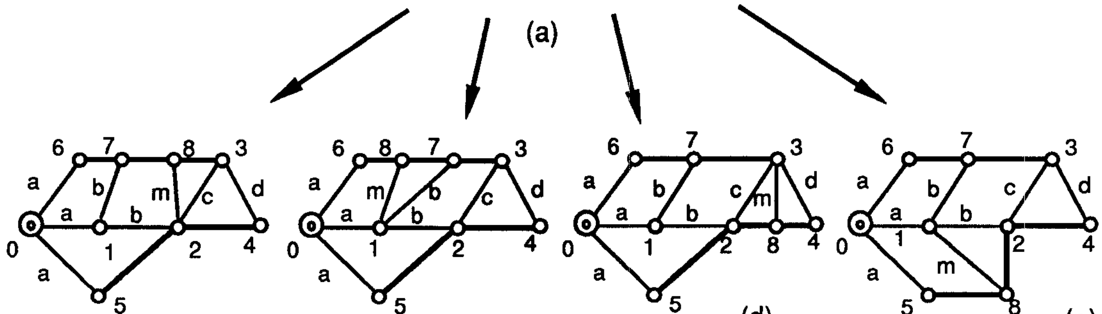

(b) (c) (d) (e)

4.6.1

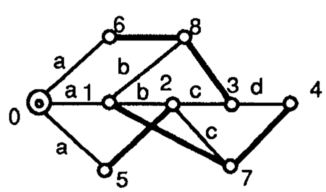

$$\begin{bmatrix} \# & \# & \# & 0 \\ \# & \# & 0 & 0 \\ \# & 0 & 0 & 0 \\ 0 & \# & \# & \# \end{bmatrix}$$

4.6.2

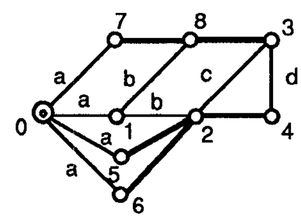

$$\begin{bmatrix} \# & \# & \# & 0 \\ \# & \# & 0 & 0 \\ \# & \# & 0 & 0 \\ 0 & 0 & \# & \# \end{bmatrix}$$

4.6.3

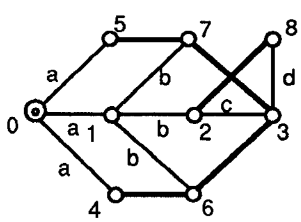

$$\begin{bmatrix} \# & \# & \# & 0 \\ \# & \# & \# & 0 \\ \# & 0 & 0 & 0 \\ 0 & 0 & \# & \# \end{bmatrix}$$

4.6.4

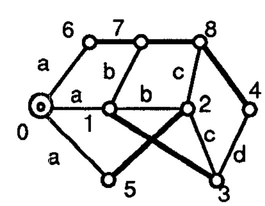

$$\begin{bmatrix} \# & \# & \# & \# \\ \# & \# & 0 & 0 \\ \# & 0 & 0 & 0 \\ 0 & \# & \# & 0 \end{bmatrix}$$

4.6.5

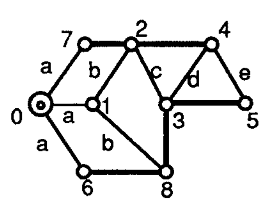

$$\begin{bmatrix} \# & \# & \# & 0 & 0 \\ \# & \# & 0 & 0 & 0 \\ \# & 0 & 0 & 0 & 0 \\ 0 & 0 & \# & \# & 0 \\ 0 & 0 & 0 & \# & \# \end{bmatrix}$$

4.6.6

Figure 4.6 The graphs of wrist mechanisms with more than three articulation points the existence of a one-DOF chain in the mechanisms. This results in different forms of the matrix elements. For example, the input-output relation for Fig. 4.2(a) is

$$\begin{bmatrix} \dot{\theta}_{50} \\ \dot{\theta}_{40} \\ \dot{\theta}_{10} \end{bmatrix} = \begin{bmatrix} 1 & N_{65} & N_{36}N_{65} \\ 1 & \frac{N_{74}N_{28}}{N_{28}-N_{18}} & 0 \\ 1 & 0 & 0 \end{bmatrix} \begin{bmatrix} \dot{\theta}_{10} \\ \dot{\theta}_{21} \\ \dot{\theta}_{32} \end{bmatrix} \tag{4.3}$$

Figure 4.3(a) is identified as the structure of the Bendix wrist mechanism. The remaining gear trains are believed to be new kinematic structures for wrist mechanisms.

Mechanisms constructed from the graphs shown in Figs. 4.4 and 4.5 have four links coaxial with base link. However, only three links can be used as the inputs. Among the four coaxial links, link 1 can not be chosen as the input link. For example, in Fig. 4.4(a), links 1, 4, and 5 is not a valid set of input links because they form a one-DOF gear train. If links 1, 5, and 6 are chosen as the input links, then link 4 becomes a redundant link, and if links 1, 4, and 6 are chosen as the input links, then link 5 becomes a redundant link. In either case, the function of the resulting mechanism is the same as that of Fig. 4.1(a). However, if links 4, 5, and 6 are chosen as input links, then the resulting mechanism will have different functional characteristics. Note that the structure matrix shown in Fig. 4.4 is based on the selection of 4, 5, and 6 as the input links.

The graphs shown in Figs. 4.6.1 through 4.6.5 have four axis levels. Hence, in the corresponding mechanisms the number of articulation points will be greater than the number of degrees of freedom by one. Further analysis shows that, although there are four articulation points, the relative motions associated with the joints in the equivalent open-loop chain are not all independent. For this reason, the structure matrices have been augmented by one. Equating the dot product of the fourth row of structure matrices and the joint velocity vector $\dot{\theta}$ to zero gives the internal dependence (coupling) of the joint velocities or joint angles. This constraint guarantees that the number of inputs is equal to the number of degrees of freedom, and the solution of the system is determinate. For example, the input-output relation for the graph shown in Fig. 4.6.1(a) is given by

$$\begin{bmatrix} \dot{\theta}_{60} \\ \dot{\theta}_{50} \\ \dot{\theta}_{10} \\ 0 \end{bmatrix} = \begin{bmatrix} 1 & N_{76} & N_{37}N_{76} & 0 \\ 1 & N_{25} & 0 & 0 \\ 1 & 0 & 0 & 0 \\ 0 & 0 & 1 & N_{42} \end{bmatrix} \begin{bmatrix} \dot{\theta}_{10} \\ \dot{\theta}_{21} \\ \dot{\theta}_{32} \\ \dot{\theta}_{43} \end{bmatrix} \tag{4.4}$$

Similarly, in Fig. 4.6.6, the graph has five axis levels, and the augmented fourth and fifth rows of the structure matrix give the internal coupling of the joints.

Figures 4.7 and 4.8 show the functional representations of wrist mechanisms having seven and eight links. These mechanisms are constructed from the graphs shown in Figs. 4.1(a)-(d), 4.3(a), 4.4(b), and 4.6.1(a), respectively. All the mechanisms are drawn in spherical wrist form, i.e. all axes intersecting at one point.

Recently, Chang and Tsai [11] independently developed an algorithm for the enumeration of the structure matrices for geared robotic mechanisms. Without resorting to the graph theory, they use the concept of transmission lines, and successfully derived all the *basic mechanisms* for different actuator distribution. Furthermore, they showed that by adding idler gears to the basic mechanisms, *derived mechanisms* can be constructed. According to their results, there are five basic mechanisms for the three-DOF, three-axes geared robotic mechanisms. In my atlas, there are four basic mechanisms as shown in Figs. 4.1(a), 4.3(a), 4.4(a), and 4.5. The The fifth basic mechanism given by Chang and Tsai [11] has all non-zero elements in the structure matrix. It is a ten-link mechanism, hence is not listed here.

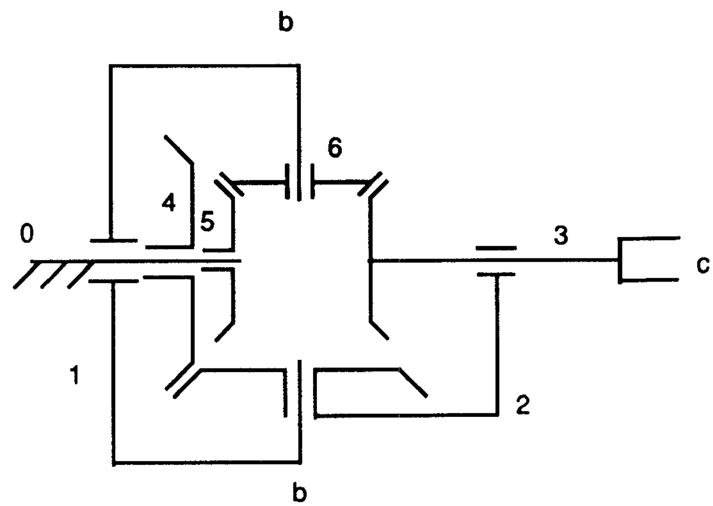

Figure 4.7 A seven-link wrist mechanism derived from Fig. 4.1(a)

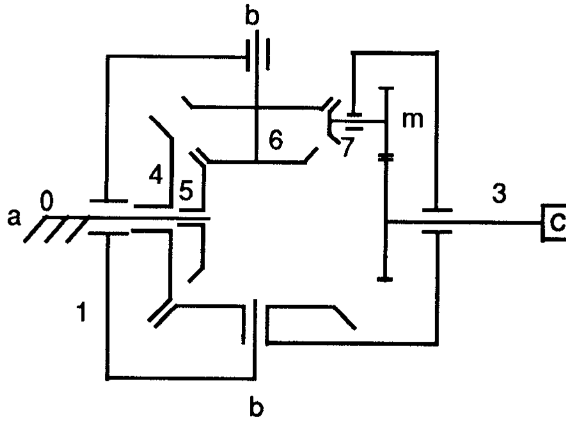

(a) Derived from Fig. 4.1(b)

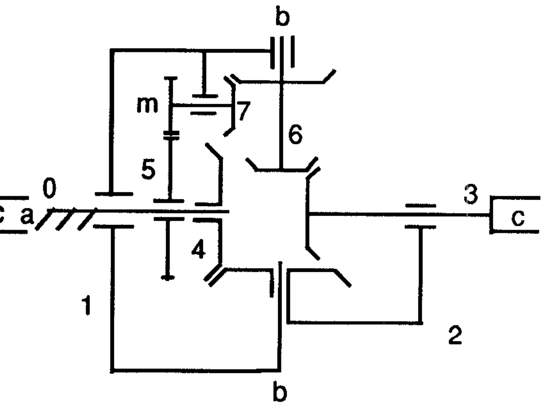

(b) Derived from Fig. 4.1(c)

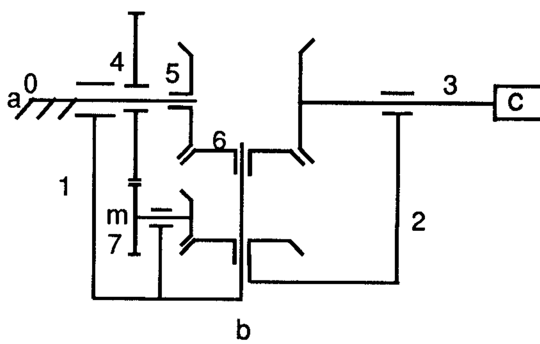

(c) Derived from Fig. 4.1(d)

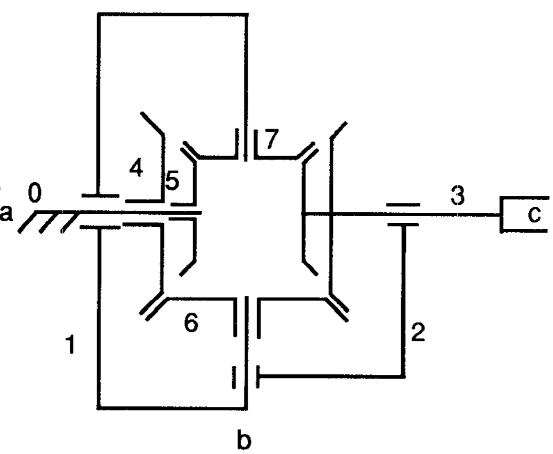

(d) Derived from Fig. 4.3(a)

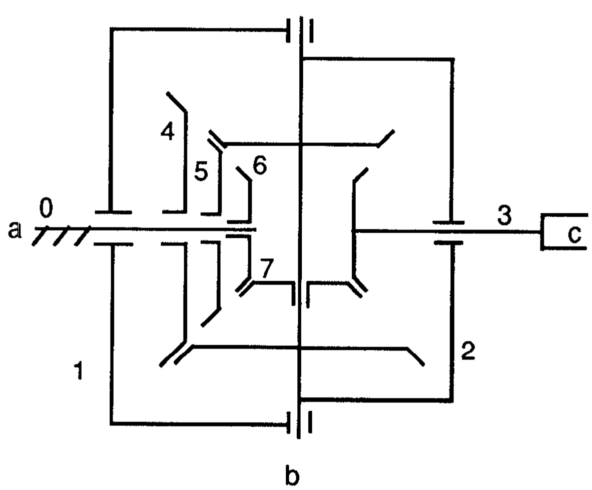

(e) Derived from Fig. 4.4(a)

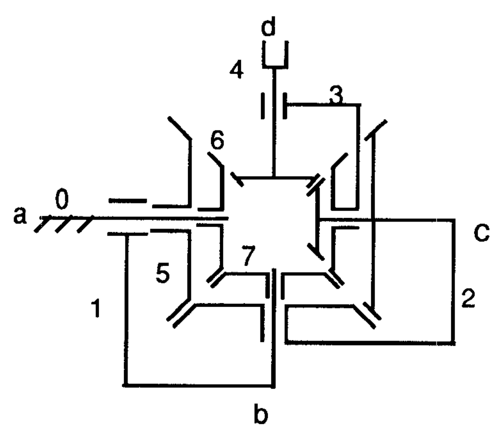

(f) Derived from Fig. 4.6.1(a)

Figure 4.8 Eight-link wrist mechanisms

4.3 Structural evaluation

The kinematic structures of bevel-gear-type robotic wrist mechanisms have been enumerated. Now a question can be asked: what is the most promising kinematic structure from the point of view of manipulability? Traditionally, the Jacobian matrix, which transforms the velocity vector from the joint space to the end-effector space, has been used to measure the kinematic performance of a manipulator. For geared robotic mechanisms, the performance measure should be based on the transformation between the actuator space and the end-effector space. Chen and Tsai [12] have developed a methodology for choosing the gear ratios of geared robotic mechanisms based on kinematic isotropy and maximum acceleration capacity conditions. In this dissertation, we shall concentrate on the singularity problem.

Paul and Stevenson [47] studied the singularity problem for open-loop, three-jointed wrist mechanisms. It was pointed out that the void in the front end can be reduced to a singular point [58]. The singular point can substantially degrade the manipulability in the frontal working zone. To study the singularity problem associated with geared robotic wrist mechanisms, the Jacobian matrix will be extended to the transformation from actuator space to end-effector space. We may write J as the product of two matrices as follows:

$$J = J_o B \tag{4.5}$$

where the matrix J_o represents the velocity mapping from the joint space to the end-effector space (the subscript 'o' denotes equivalent open-loop chain), and the matrix B represents the velocity mapping from the actuator space to the joint space. The matrix J_o depends on the linkage parameters such as the twist angles and the joint angles, while B depends on the structural topology of the mechanism. If the number of articulation points is equal to the number of degrees of freedom, then B is the inverse of the structure matrix A, i.e. $B = A^{-1}$. Since B is a non-singular square matrix, the singularities of J are not affected by B. Thus the singularity depends only on the geometry of the joint axes in the equivalent open-loop chain, and the manipulability for three-jointed bevel-gear-type wrist mechanisms cannot be improved by the arrangement of the gear trains.

However, when the number of articulation points is greater than three, J_o and B become non-square matrices. We can expect the matrix B (the topological structure) to have some influence on the singularity. The structure shown in Fig. 4.8(f), is a three-DOF, four-jointed bevel-gear-type wrist mechanism with the motions of links 3 and 4 coupled. Two additional mechanisms, one with links 2 and 3 coupled, and the other with links 1 and 2 coupled, are shown in Figs. 4.9 and 4.10. The mechanism shown in Fig. 4.9 is derived from Fig. 4.6.5, and the mechanism shown in Fig. 4.10 does not belong to the atlas because it contains more than nine links. Considering of the wrist mechanism shown in Fig. 4.10, let all the twist angles be $\pi/2$, then the Jacobian matrix is given by

$$\begin{aligned} J &= J_o B \\ &= \begin{bmatrix} 0 & S_1 & C_1 S_2 & C_1 C_2 S_3 - S_1 C_3 \\ 0 & -C_1 & S_1 S_2 & S_1 C_2 S_3 + C_1 C_3 \\ 1 & 0 & -C_2 & S_2 S_3 \end{bmatrix} \\ & \quad \begin{bmatrix} 1 & 0 & 0 \\ -N_{02} & 0 & 0 \\ -N_{63}(N_{02} - N_{56}) & -N_{63}N_{56} & 0 \\ -N_{94}N_{63}(N_{02} - N_{56}) - N_{94}N_{89}(N_{78} - N_{02}) & -N_{94}N_{63}N_{56} & N_{94}N_{89}N_{78} \end{bmatrix} \end{aligned} \tag{4.6}$$

where $C_i = cos\theta_i$, $S_i = sin\theta_i$, θ_i's are the joint angles, and $N_{ij} = N_i/N_j$ is the gear ratio between the gears attached on links i and j.

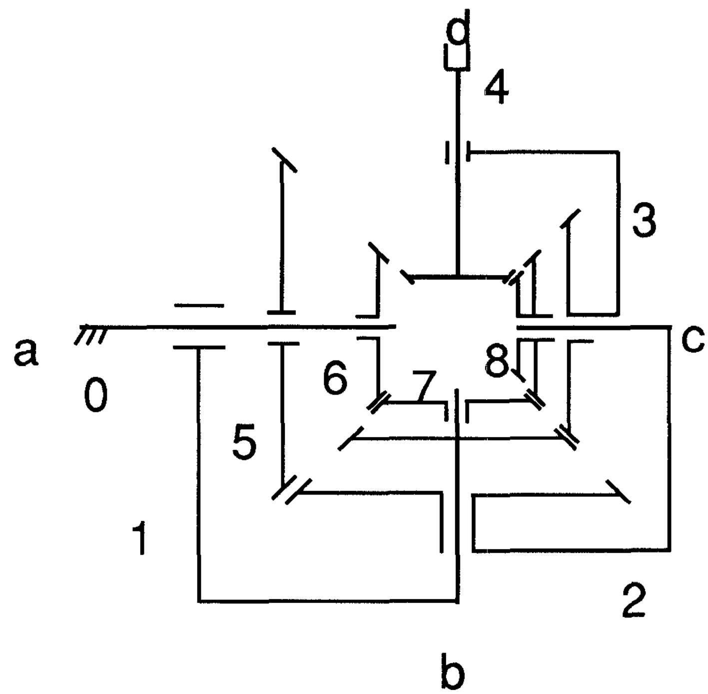

Figure 4.9 A three-DOF, four-jointed wrist mechanism with links 2 and 3 coupled, derived from Fig. 4.6.5.

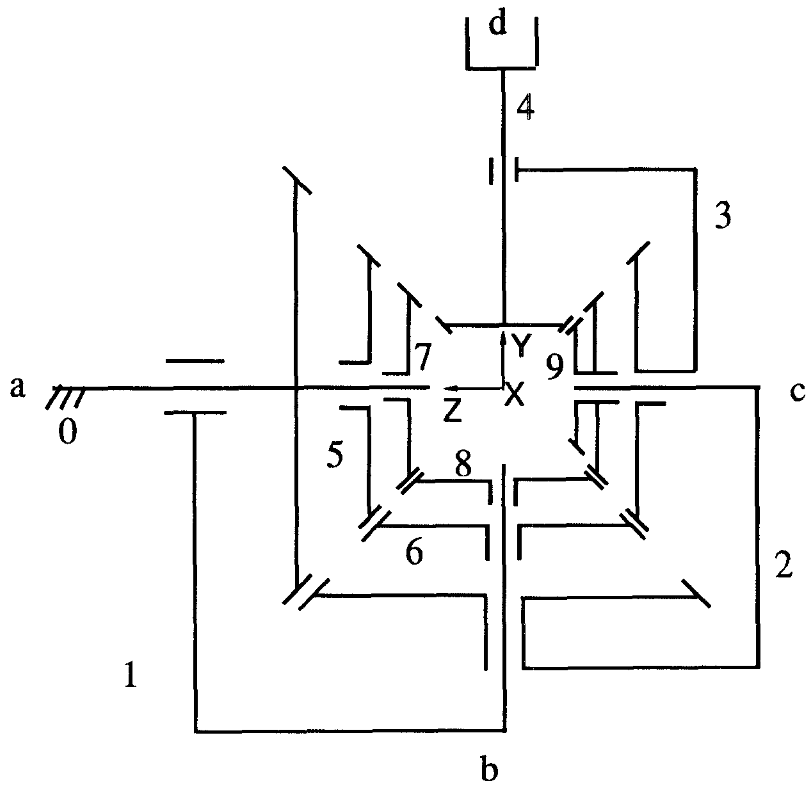

Figure 4.10 A three-DOF, four-jointed wrist mechanism with links 1 and 2 coupled.

The determinant of the Jacobian is

$$det(J) = K(N_{02}sin\theta_3 - sin\theta_2 cos\theta_3) \tag{4.7}$$

where K is a constant.

The locus of the singular points obtained by equating Eq. (4.7) to zero is shown in Fig. 4.11. We note that the singularity in the front end has been removed. Furthermore, there exist non-singular inverse kinematic solutions on the singular curve. Due to the above promising characteristics, three-DOF four-jointed bevel-gear-type wrist mechanisms deserve further study and is the subject of the next two chapters. Considering possible link interference, kinematic structures with more than four articulation points are not practical, and will not be studied.

4.4 Summary

All the admissible kinematic structures of spherical wrist mechanisms with up to nine links have been identified and categorized. A representative mechanism corresponding to each kinematic structure having seven and eight links has been sketched. Excluding three existing wrist mechanisms, all the other kinematic structures are believed to be new. It is found that thee-DOF, four-jointed wrist mechanisms do have the potential for improving the manipulability, and therefore will be studied in the next two chapters.

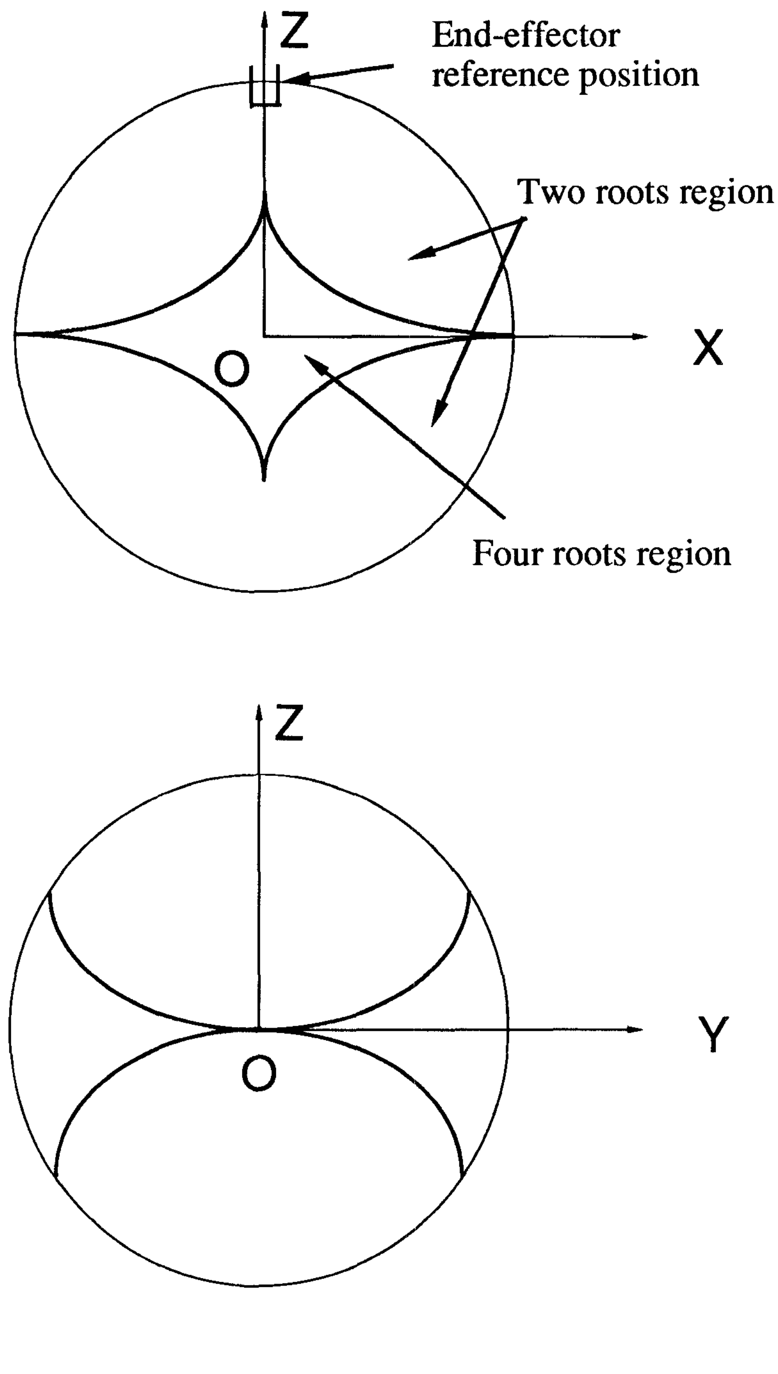

Figure 4.11 Two views of the singular curves
on the workspace sphere

Chapter 5

TRAJECTORY ANALYSIS OF SPHERICAL PLANETARY GEAR TRAINS

5.1 Introduction

In Chapter 4, three novel three-DOF, four-jointed bevel-gear-type wrist mechanisms have been identified. It was pointed out that four-jointed wrist mechanisms possess a significantly different kinematic characteristics in comparison with conventional three-jointed wrist mechanisms. In what follows, the workspace and singularity problems associated with this type of four-jointed wrist mechanisms will be stidied in detail. An examination of the structures shown in Figs. 4.8(f), 4.9, and 4.10 reveals that there is a spherical planetary gear train imbedded in each mechanism. Hence, it is helpful to study the trajectories generated by such spherical planetary gear trains, before we proceed to the workspace analysis.

In the theory of Kinematics of Mechanisms, trajectories generated by planetary gear trains form an important family of curves, known as Epitrochoids or Hypotrochoids, depending on whether the gearing is external or internal [35]. If the tracer point is on the pitch circle of the planet gear, the curve is called Epicycloid or Hypocycloid. Knowledge of planar epicyclic curves dates back to two thousand years ago, when ancient astronomer Hipparchos (180-125 B.C.) used epicycles to describe the paths of planets. Throughout the history of science and technology, these curves also found application in mechanics, optics, architecture, kinematics, etc [7].

It is helpful to briefly review the trajectories generated by a planar planetary gear train because of its analogy to the spherical case. Figure 5.1 shows a planar planetary gear train, which consists of three links, two turning pairs, and one gear pair. Therefore, it has one degree of freedom. The input of the system is the carrier (link 2). The sun gear is fixed to the ground (link 1), while the planet gear (link 3) revolves around the sun gear when the carrier rotates. Let the radii of the sun and planet gears be r_s and r_p, respectively. Then, the length of the carrier, l_2, is equal to $r_s + r_p$. Let the distance from the tracer point to the center of the planet gear be l_3 and let the initial position be as shown in Fig. 5.1 (zero phase angle). Then the position of the tracer point can be described by the following parametric equations:

$$\begin{aligned} x &= l_2 c\theta_2 + l_3 c[(1 + r_s/r_p)\theta_2] \\ y &= l_2 s\theta_2 + l_3 s[(1 + r_s/r_p)\theta_2] \end{aligned} \tag{5.1}$$

where θ_2 is the inclination of $\vec{OO'}$ (link 2), and where c denotes the cosine function and s the sine function.

Let the radii of both gears be one, and the lengths of l_3 for tracer points a, b, and c, be 0.7, 1.0, and 1.4, respectively. Then the trajectory traced by the point c, which lies outside the pitch circle of the planet gear, has a node, while the trajectory traced by point b, which lies on the pitch circle of the planet gear, has a cusp, as shown in Fig. 5.1. The curve is called a *limacon* when $r_s/r_p = 1$, and is called a *cardioid* when $r_s/r_p = l_3/r_p = 1$. The geometric properties of limacons and

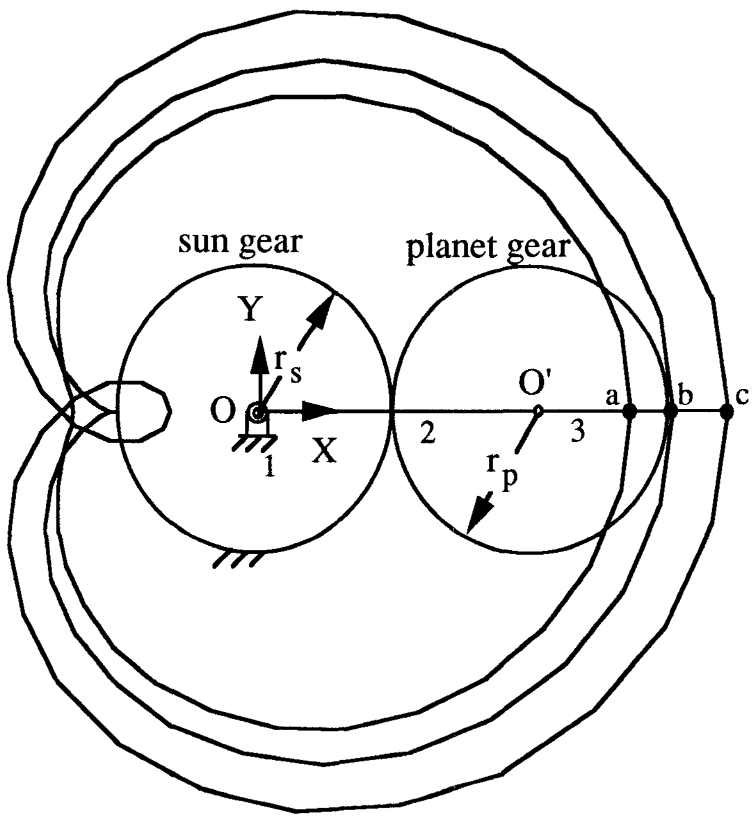

Figure 5.1 The limacons traced by a planar planetary gear train (n=1), where l_3= 0.7, 1, and 1.4 for tracer points a, b, and c, respectively.

cardioids can be found in [45,10]. For other ratios of r_s/r_p and l_3/r_p, see Lawrence [35] for the shape of curves.

5.2 Parametric equations of the trajectory

Figure 5.2 shows the schematic of a spherical planetary gear train. The trajectory generated by a tracer point on the planet gear lies on a sphere centered about point O, the common apex of the pitch cones formed by the sun and planet gears. The link coordinate systems are defined according to the D-H convention [17]. The origin of each coordinate system is located at the center O. However, they have been sketched away from the center for the reason of clarity. The $(XYZ)_1$ coordinate system is fixed to the base link with the X_1-axis pointing out of the paper and the Z_1-axis pointing along the first joint axis. The stretched out, joint axes coplanar configuration of the mechanism has been chosen as the reference position, and define all the positive X-axes to be pointing out of the paper. The joint angle θ_i is the angle measured from X_{i-1} to X_i-axis about the positive Z_{i-1}-axis. The directions of the Z-axes are chosen in such a way that twist angles, α_2 and α_3, are less than π and greater than zero. The twist angle α_i is the angle measured from Z_{i-1} to Z_i-axis about the positive X_i-axis. Let α_s and α_p denote the cone angles of the sun gear and planet gear, respectively, and let $n = \sin\alpha_s / \sin\alpha_p$ be the gear ratio, then,

$$n = -\frac{\dot{\theta}_{32}}{\dot{\theta}_{12}} = \frac{\dot{\theta}_{32}}{\dot{\theta}_{21}} \tag{5.2}$$

where $\dot{\theta}_{ij}$ is the magnitude of the angular velocity of link i with respect to link j. In what follows, $\dot{\theta}_i$ will be used to denote $\dot{\theta}_{i,i-1}$ for brevity.

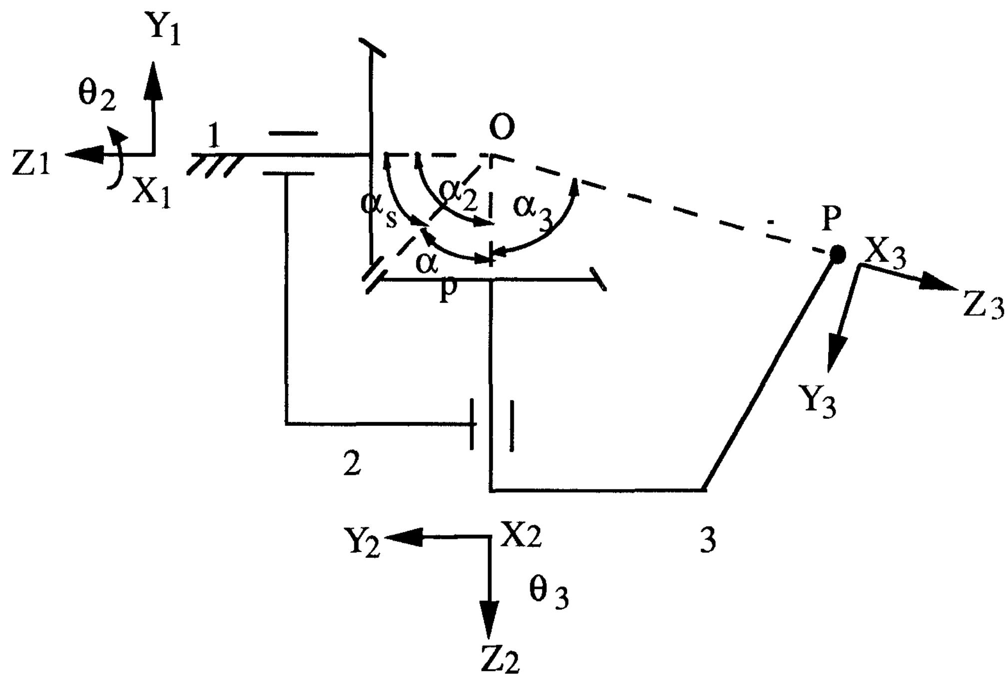

Figure 5.2 A spherical planetary gear train

Integrating Eq. (5.2), yields

$$\theta_3 = n\theta_2 + \theta_p \tag{5.3}$$

where $\theta_3 = \theta_{32}$ and $\theta_2 = \theta_{21}$ are the joint angles associated with links 3 and 2, respectively, and θ_p is a phase angle. For the configuration shown in Fig. 5.2, the phase angle θ_p is equal to zero.

The position vector $\vec{P}$ of a tracer point P, located on the Z_3-axis and one unit length away from the origin as shown in Fig. 5.2, can be expressed in the $(XYZ)_1$ frame as

$$\begin{aligned}
\vec{P} &= \begin{bmatrix} c\theta_2 & -s\theta_2 c\alpha_2 & s\theta_2 s\alpha_2 \\ s\theta_2 & c\theta_2 c\alpha_2 & -c\theta_2 s\alpha_2 \\ 0 & s\alpha_2 & c\alpha_2 \end{bmatrix} \begin{bmatrix} s\theta_3 s\alpha_3 \\ -c\theta_3 s\alpha_3 \\ c\alpha_3 \end{bmatrix} \\
&= \begin{bmatrix} c\theta_2 s\theta_3 s\alpha_3 + s\theta_2 c\theta_3 c\alpha_2 s\alpha_3 + s\theta_2 s\alpha_2 c\alpha_3 \\ s\theta_2 s\theta_3 s\alpha_3 - c\theta_2 c\theta_3 c\alpha_2 s\alpha_3 - c\theta_2 s\alpha_2 c\alpha_3 \\ -c\theta_3 s\alpha_2 s\alpha_3 + c\alpha_2 c\alpha_3 \end{bmatrix}
\end{aligned} \tag{5.4}$$

where θ_3 is related to θ_2 by Eq. (5.3). The point P will trace a curve as θ_2 varies from $-\pi$ to π.

5.3 Effect of the phase angle

Let $\theta_p = 0$, then $\theta_3 = n\theta_2$, and Eq. (5.4) becomes

$$\vec{P} = \begin{bmatrix} c\theta_2 s(n\theta_2) s\alpha_3 + s\theta_2 c(n\theta_2) c\alpha_2 s\alpha_3 + s\theta_2 s\alpha_2 c\alpha_3 \\ s\theta_2 s(n\theta_2) s\alpha_3 - c\theta_2 c(n\theta_2) c\alpha_2 s\alpha_3 - c\theta_2 s\alpha_2 c\alpha_3 \\ -c(n\theta_2) s\alpha_2 s\alpha_3 + c\alpha_2 c\alpha_3 \end{bmatrix} \tag{5.5}$$

Now suppose $\theta_p \neq 0$, then the new position vector $\vec{P'}$ becomes

$$\vec{P'} = \begin{bmatrix} c\theta_2 s(n\theta_2 + \theta_p) s\alpha_3 + s\theta_2 c(n\theta_2 + \theta_p) c\alpha_2 s\alpha_3 + s\theta_2 s\alpha_2 c\alpha_3 \\ s\theta_2 s(n\theta_2 + \theta_p) s\alpha_3 - c\theta_2 c(n\theta_2 + \theta_p) c\alpha_2 s\alpha_3 - c\theta_2 s\alpha_2 c\alpha_3 \\ -c(n\theta_2 + \theta_p) s\alpha_2 s\alpha_3 + c\alpha_2 c\alpha_3 \end{bmatrix} \tag{5.6}$$

Replacing the parameter $n\theta_2$ in Eq. (5.6) by $n\theta_2 - \theta_p$, and θ_2 by $\theta_2 - \theta_p/n$, yields,

$$\vec{P}'' = \begin{bmatrix} s(n\theta_2)c(\theta_2 - \theta_p/n)s\alpha_3 + c(n\theta_2)s(\theta_2 - \theta_p/n)c\alpha_2 s\alpha_3 + s(\theta_2 - \theta_p/n)s\alpha_2 c\alpha_3 \\ s(n\theta_2)s(\theta_2 - \theta_p/n)s\alpha_3 - c(n\theta_2)c(\theta_2 - \theta_p/n)c\alpha_2 s\alpha_3 - c(\theta_2 - \theta_p/n)s\alpha_2 c\alpha_3 \\ -c(n\theta_2)s\alpha_2 s\alpha_3 + c\alpha_2 c\alpha_3 \end{bmatrix} \tag{5.7}$$

Equation (5.7) can also be written as:

$$\begin{aligned} \vec{P}'' &= \begin{bmatrix} c(\theta_p/n) & s(\theta_p/n) & 0 \\ -s(\theta_p/n) & c(\theta_p/n) & 0 \\ 0 & 0 & 1 \end{bmatrix} \begin{bmatrix} c\theta_2 s(n\theta_2)s\alpha_3 + s\theta_2 c(n\theta_2)c\alpha_2 s\alpha_3 + s\theta_2 s\alpha_2 c\alpha_3 \\ s\theta_2 s(n\theta_2)s\alpha_3 - c\theta_2 c(n\theta_2)c\alpha_2 s\alpha_3 - c\theta_2 s\alpha_2 c\alpha_3 \\ -c(n\theta_2)s\alpha_2 s\alpha_3 + c\alpha_2 c\alpha_3 \end{bmatrix} \\ &= R(-\theta_p/n, \hat{Z}_1)\vec{P} \end{aligned} \tag{5.8}$$

where R denotes a rotation matrix.

Equation (5.8) shows that adding a phase angle has the effect of rotating the original vector and, hence, the trajectory about Z_1-axis an angle $-\theta_p/n$. Note that the shape of the trajectory is not changed under orthogonal transformation.

5.4 Geometry of the trajectory, gear ratio n=1

A geometric description of the parametric equations can help us to visualize the trajectory of P. Since θ_p only affects the orientation of the trajectory, we may assume $\theta_p = 0$ without loss of generality. For $n = 1$, Eq. (5.5) reduces to

$$\vec{P} = \begin{bmatrix} c\theta_2 s\theta_2 s\alpha_3(1 + c\alpha_2) + s\theta_2 s\alpha_2 c\alpha_3 \\ (1 - c^2\theta_2)s\alpha_3 - c^2\theta_2 c\alpha_2 s\alpha_3 - c\theta_2 s\alpha_2 c\alpha_3 \\ -c\theta_2 s\alpha_2 s\alpha_3 + c\alpha_2 c\alpha_3 \end{bmatrix} \tag{5.9}$$

5.4.1 Geometric description

Eliminating θ_2 from the second and third equations in Eq. (5.9), yields

$$(z + \frac{k_2}{2k_1})^2 + \frac{k_3}{k_1}\left[y - \left(\frac{k_2^2}{4k_1k_3} - \frac{k_4}{k_3}\right)\right] = 0 \tag{5.10}$$

where

$$k_1 = c\alpha_2 + 1$$

$$k_2 = -2c\alpha_2 c\alpha_3(1 + c\alpha_2) - c\alpha_3 s^2\alpha_2$$

$$k_3 = s^2\alpha_2 s\alpha_3$$

$$k_4 = c^2\alpha_2 c^2\alpha_3(1 + c\alpha_2) + s^2\alpha_2(c\alpha_2 c^2\alpha_3 - s^2\alpha_3)$$

Equation (5.10) represents a cylinder with a parabolic directrix in the Y-Z plane and with its elements parallel to the X-axis. The coefficient of y, (k_3/k_1), is always positive. Therefore, the directrix parabola is convex to the positive Y-axis direction. The z-coordinate of the apex is located at

$$\begin{aligned} z_a &= -\frac{k_2}{2k_1} \\ &= \frac{1}{2}c\alpha_3(1 + c\alpha_2) \end{aligned} \tag{5.11}$$

The sign of z_a depends on α_3. If $0 < \alpha_3 < \pi/2$, then the apex is located above the X-Y plane; if $\pi/2 < \alpha_3 < \pi$, then it is located below the X-Y plane. The y-coordinate of the apex, which is also the maximum y-coordinate of the cylinder, is given by

$$y_a = s\alpha_3 + \frac{c^2\alpha_3(1 - c\alpha_2)}{4s\alpha_3} \tag{5.12}$$

Summing the squares of the x, y, z components of Eq. (5.5), yields $x^2 + y^2 + z^2 = 1$. Hence, the trajectory of point P is the intersection of the cylinder and a unit sphere. Figure 5.3 shows a typical parabolic cylinder and its intersection with the unit sphere.

5.4.2 Extrema, nodes, and cusps

For the planar case, the geometry of epitrochoids has been described in several aspects: axes of symmetry, extent of the curve, number of node(s) or cusp(s) and their location(s), etc. Similar geometric characteristics can also be used in the spherical case. Since the elements of the cylinder (Fig. 5.3) are parallel to the X-axis, the intersection of the cylinder with a unit sphere centered at origin is symmetric with respect to the Y-Z plane. The extend of the trajectory can be found by solving the extreme values of its x, y, and z coordinates.

Extrema of z

The extreme values of z can be found by equating the derivative of the z-component in Eq. (5.9) to zero, i.e.

$$\frac{dz}{d\theta_2} = s\theta_2 s\alpha_2 s\alpha_3 = 0 \tag{5.13}$$

From the above equation and the second-order derivative of z, we may conclude that at $\theta_2 = \pi$ and $\theta_2 = 0$, z reaches its maximum z_{max} and minimum z_{min}, respectively, as shown in Fig. 5.3. Substituting $\theta_2 = \pi$ into Eq. (5.9), we obtain

$$\vec{P}_{z_{max}} = \begin{bmatrix} 0 \\ s(\alpha_2 - \alpha_3) \\ c(\alpha_2 - \alpha_3) \end{bmatrix} \tag{5.14}$$

Substituting $\theta_2 = 0$ into Eq. (5.9), we obtain

$$\vec{P}_{z_{min}} = \begin{bmatrix} 0 \\ -s(\alpha_2 + \alpha_3) \\ c(\alpha_2 + \alpha_3) \end{bmatrix} \tag{5.15}$$

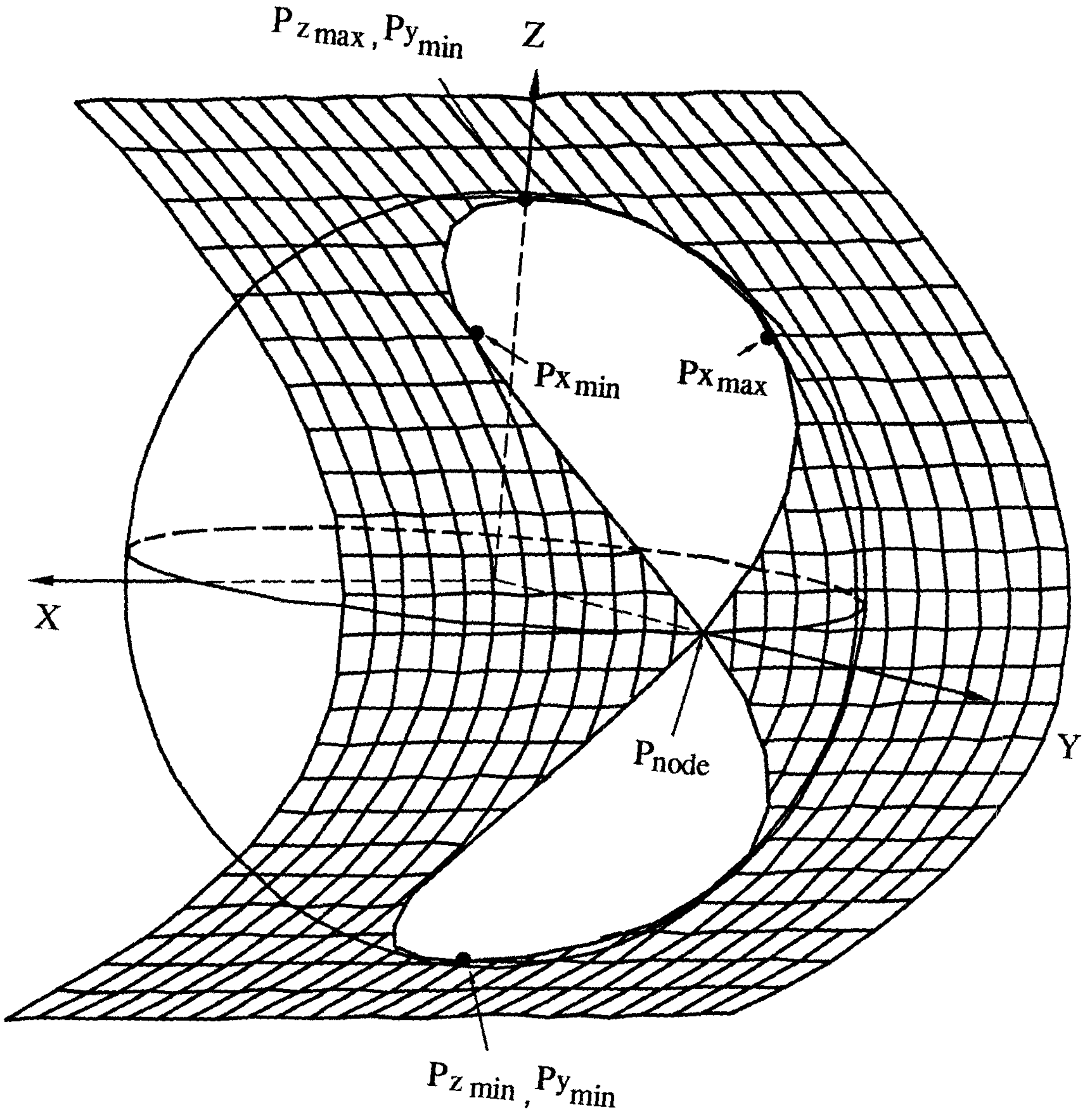

$\alpha_2 = \pi/2$ and $\alpha_3 = \pi/2$

Figure 5.3 Intersection of a parabolic cylinder and a unit sphere

Note that the two vectors with extreme values of z lie on the Y-Z plane, the plane of symmetry for the trajectory. Equations (5.14) and (5.15) imply that, the angle ψ_z, measured from $\vec{P}_{z_{max}}$ to $\vec{P}_{z_{min}}$ in the clockwise direction, is given by

$$\psi_z = 2(\pi - \alpha_2) \tag{5.16}$$

We note that the angle ψ_z is a function of α_2 only, and $\psi_z = \pi$ when $\alpha_2 = \pi/2$.

Extrema of x

The extreme values of x can be found by equating the first derivative of the x-component in Eq. (5.9) to zero, i.e.

$$\frac{dx}{d\theta_2} = 2u_0 c^2\theta_2 + u_1 c\theta_2 - u_0 = 0 \tag{5.17}$$

where $u_0 = s\alpha_3 + c\alpha_2 s\alpha_3$, $u_1 = s\alpha_2 c\alpha_3$.

The solutions of Eq. (5.17) are

$$\theta_2 = cos^{-1}\left(\frac{-u_1 \pm \sqrt{u_1^2 + 8u_0^2}}{4u_0}\right) \tag{5.18}$$

There will be four extreme values of x, if

$$-1 \leq \frac{-u_1 \pm \sqrt{u_1^2 + 8u_0^2}}{4u_0} \leq 1 \tag{5.19}$$

It can be shown that Eq. (5.19) is satisfied if

$$\frac{\alpha_2}{2} \leq \alpha_3 \leq \pi - \frac{\alpha_2}{2} \tag{5.20.a}$$

or

$$\alpha_p \leq \alpha_3 \leq \pi - \alpha_p \tag{5.20.b}$$

Equation (5.20) is the condition for the trajectory to have four extreme values of x. The position of $\vec{P}$ with extreme values of x-coordinates can be obtained by substituting the solutions of θ_2 from Eq. (5.18) into Eq. (5.9). However, they are no longer in a simple form. There are two pairs of $\vec{P}_{x_{max}}$ and $\vec{P}_{x_{min}}$ when Eq. (5.20) is satisfied, and $x_{min} = -x_{max}$ for each pair of extreme positions. The angle, ψ_x, between $\vec{P}_{x_{max}}$ and $\vec{P}_{x_{min}}$ is given by

$$\psi_x = 2sin^{-1}(x_{max}) \tag{5.21}$$

Points of intersection at the Y-Z plane

Equating the x-component in Eq. (5.9) to zero, we obtain the points where the trajectory intersect the Y-Z plane:

$$s\theta_2[c\theta_2 s\alpha_3(1 + c\alpha_2) + s\alpha_2 c\alpha_3] = 0$$

Hence,

$$\theta_2 = 0 \text{ or } \pi \tag{5.22.a}$$

or

$$\theta_2 = cos^{-1}\left(-\frac{s\alpha_2 c\alpha_3}{s\alpha_3(1 + c\alpha_2)}\right) \tag{5.22.b}$$

Equation (5.22.a) implies that the trajectory intersects the Y-Z plane at least twice at the locations where the extreme values of z occur. Equation (5.22.b) yields two real solutions if

$$-1 \leq -\frac{s\alpha_2 c\alpha_3}{s\alpha_3(1 + c\alpha_2)} \leq 1 \tag{5.23}$$

It can be shown that Eq. (5.23) is satisfied when

$$\frac{\alpha_2}{2} \leq \alpha_3 \leq \pi - \frac{\alpha_2}{2} \tag{5.24}$$

We note that Eq. (5.24) is identical to Eq. (5.20), which means that whenever there exist four extreme values of x, the trajectory intersects the plane of symmetry four times. When Eq. (5.24) is satisfied, the two additional points of intersection can be found by substituting $\cos\theta_2$ from Eq. (5.22.b) into Eq. (5.9). Since the y and z components of $\vec{P}$ depend only on $\cos\theta_2$, we may conclude that the two additional points of intersection is a double point. This means the trajectory intersects itself and the node lies on the plane of symmetry as shown in Fig. 5.3. The coordinates of the node are

$$\vec{P}_{node} = \begin{bmatrix} 0 \\ s\alpha_3 \\ c\alpha_3 \end{bmatrix} \tag{5.25}$$

which is function of α_3 only.

Inequality (5.20) or (5.24) implies that whenever the twist angle α_3 is greater than the cone angle of the planet gear ($\alpha_p = \alpha_s = \alpha_2/2$) and less than its supplement, the locus of point P will intersect itself similar to the planar planetary gear train shown in Fig. 5.1. The equal sign results in a critical case where the node degenerates into a cusp. The location of the cusp can also be expressed by Eq. (5.25). Hence, the criterion for the existence of a cusp is similar to the planar case: the tracer point lies on the pitch cone of the planet gear or its image cone.

Extrema of y

The extreme values of y can be found by equating the first derivative of the y-component in Eq. (5.9) to zero, i.e.

$$\frac{dy}{d\theta_2} = s\theta_2[2c\theta_2 s\alpha_3(1 + c\alpha_2) + s\alpha_2 c\alpha_3] = 0 \tag{5.26}$$

Hence,

$$\theta_2 = 0 \text{ or } \pi \tag{5.27.a}$$

or

$$\theta_2 = cos^{-1}\left(-\frac{s\alpha_2 c\alpha_3}{2s\alpha_3(1+c\alpha_2)}\right) \tag{5.27.b}$$

Equation (5.27.a) implies that two extreme values of y occur at the same locations where the extreme values of z occur, and they are given by Eqs. (5.14) and (5.15), respectively. If the θ_2's derived from Eq. (5.27.b) are real, then two additional points for extreme values of y exist. It can be shown that the y and z-coordinates of these two extreme points are given by Eqs. (5.12) and (5.11), respectively. Since the y and z components of $\vec{P}$ in Eq. (5.9) depend only on $\cos\theta_2$, the two extreme points have the same y and z coordinates, but different values of x.

Typical trajectories

Figure 5.4 shows some trajectories generated from a few typical spherical planetary gear trains. Generally, The angle α_2 defines the maximum range in latitudinal direction of the trajectory, while α_3 defines the position of the node (or cusp). When $\alpha_2 = \pi/2$, the angle ψ_z between $\vec{P}_{z_{max}}$ and $\vec{P}_{z_{min}}$ is equal to π; when $\alpha_3 = \pi/2$, the trajectory is symmetric about the X-Y plane. The trajectory has a figure-8 shape if both sides of inequality in Eq. (5.24) are satisfied as shown in Figs. 5.4(a)-(d). They are analogous to curves generated by a planar planetary gear train (Fig. 5.1), which are called limacons. A limacon is defined as the curve which has the form of $r = a - b\sin\theta$ or $r = a - b\cos\theta$, where r and θ are the parameters in polar coordinate system, and a and b are two constants. In the spherical case, the third equation in Eq. (5.9) resembles the above relation. In what follows, the trajectories traced by a tracer point on a spherical planetary gear train will be called *spherical limacons*. In summary, there are three types of spherical limacons: (i) when the

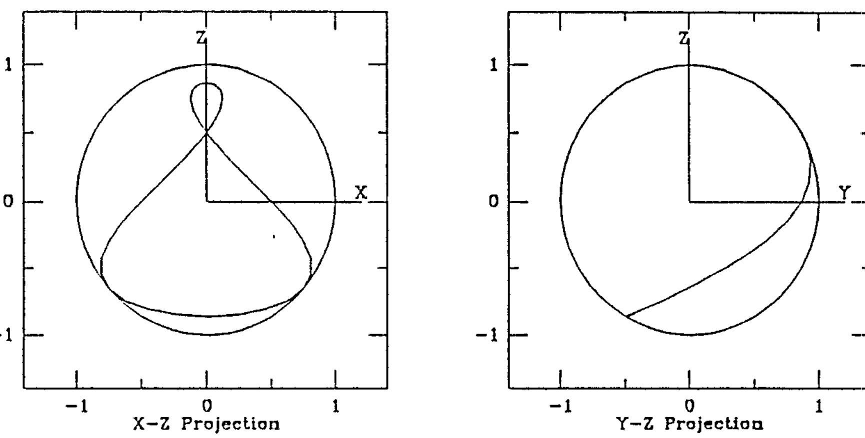

(a) $\alpha_2 = \pi/2, \quad \alpha_3 = \pi/3$

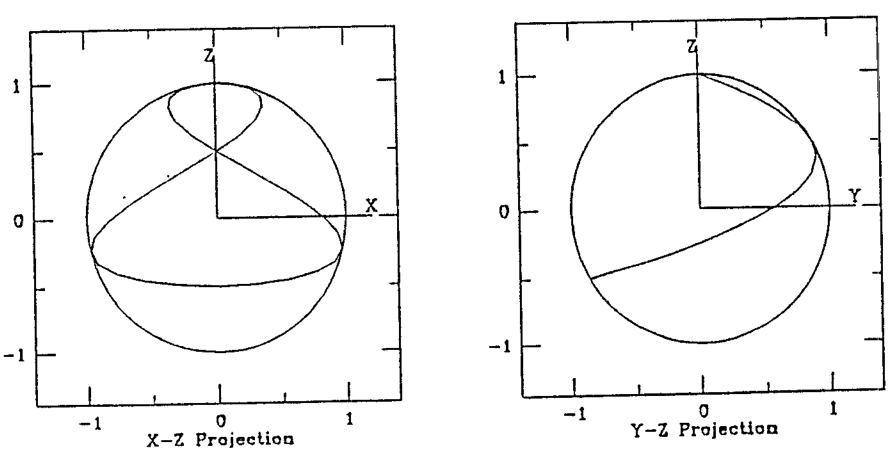

(b) $\alpha_2 = \pi/3, \quad \alpha_3 = \pi/3$

Figure 5.4 Spherical limacons generated by spherical planetary gear trains (n=1)

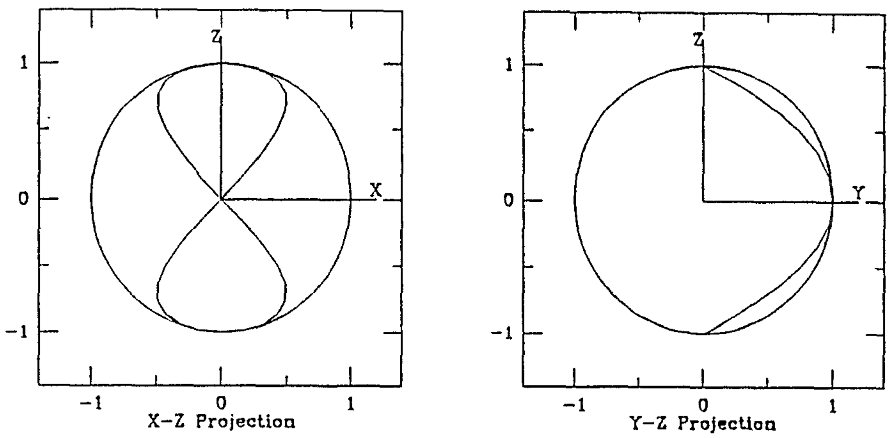

(c) $\alpha_2 = \pi/2, \quad \alpha_3 = \pi/2$

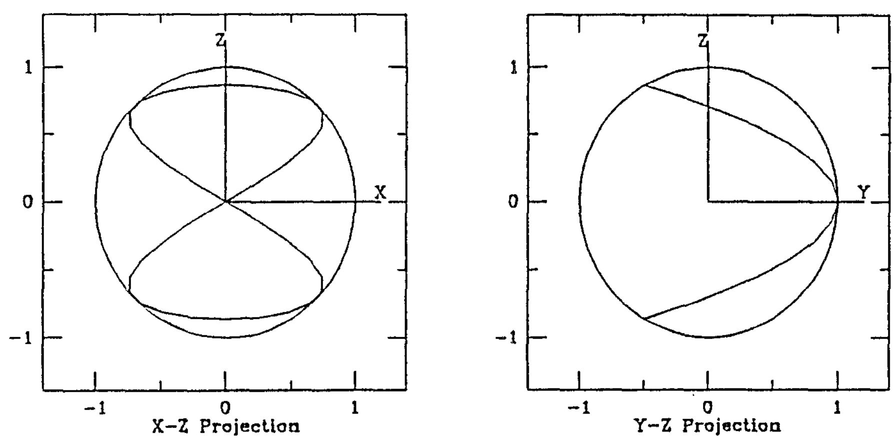

(d) $\alpha_2 = \pi/3, \quad \alpha_3 = \pi/2$

Figure 5.4 (Continued)

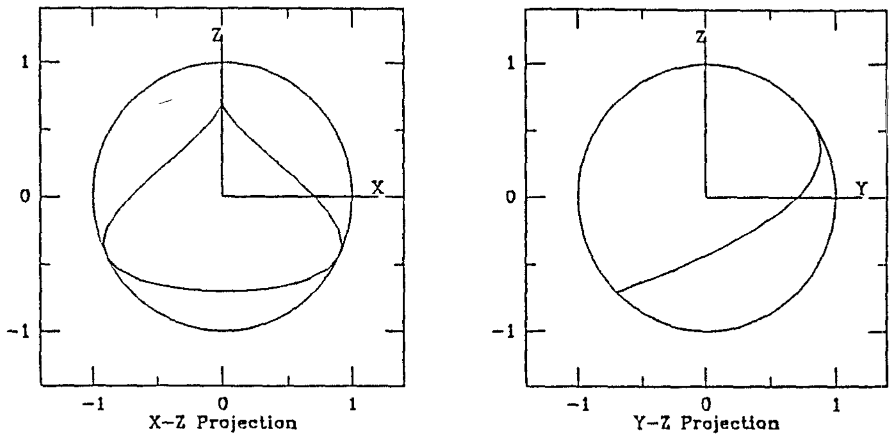

(e) $\alpha_2 = \pi/2, \quad \alpha_3 = \pi/4$

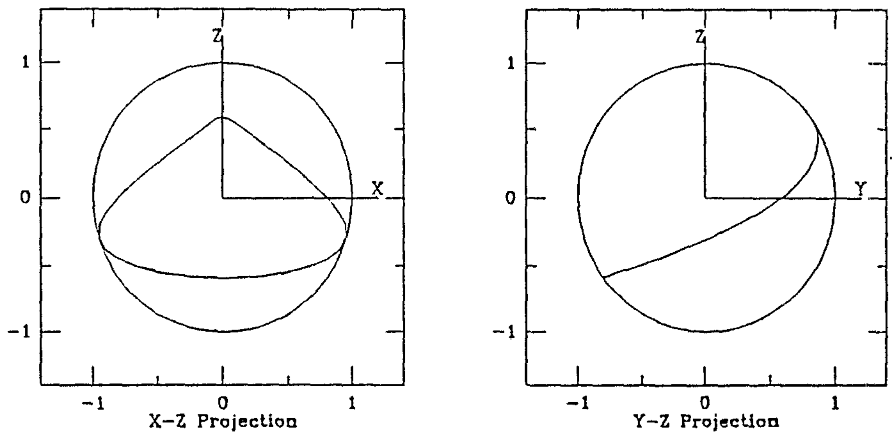

(f) $\alpha_2 = \pi/2, \quad \alpha_3 = \pi/5$

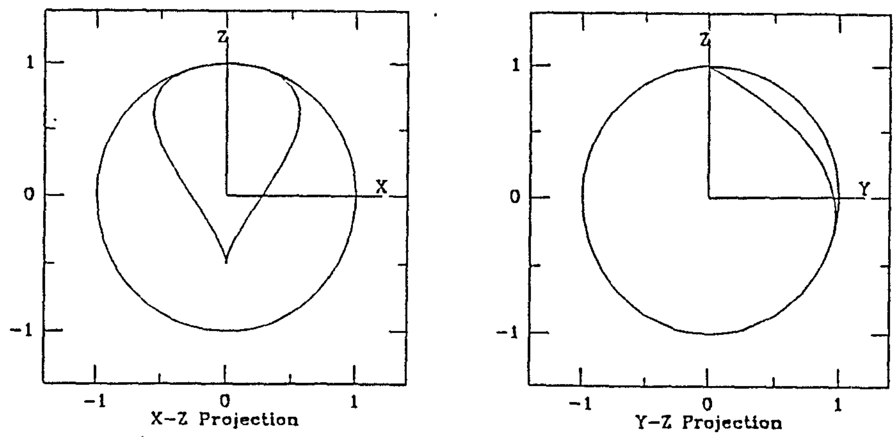

(g) $\alpha_2 = 2\pi/3, \; \alpha_3 = 2\pi/3$

Figure 5.4 (Continued)

twist angles do not satisfy Eq. (5.24), the trajectories become simply-connected curves; (ii) when one of the equality-sign in Eq. (5.24) is satisfied, the trajectory has a cusp; and (iii) when the inequality in Eq. (5.24) is satisfied, the trajectory has a node. Figures 5.4(e) and (g) show two critical cases where the trajectories change to spherical cardioids, while Fig. 5.4(f) shows an example for which the left-hand-side of Eq. (5.24) is not satisfied.

5.5 Geometry of the trajectory, gear ratio n=2

For $n = 2$, Eq. (5.5) reduces to

$$\vec{P} = \begin{bmatrix} s\theta_2[2(1-s^2\theta_2)s\alpha_3(1+c\alpha_2)+s(\alpha_2-\alpha_3)] \\ c\theta_2[2(1-c^2\theta_2)s\alpha_3(1+c\alpha_2)-s(\alpha_2+\alpha_3)] \\ -c(2\theta_2)s\alpha_2 s\alpha_3 + c\alpha_2 c\alpha_3 \end{bmatrix} \tag{5.28}$$

Note that $\cos(2\theta_2) = 2\cos^2\theta_2 - 1 = 1 - 2\sin^2\theta_2$.

5.5.1 Geometric description

Eliminating θ_2 from the second and third equations in Eq. (5.28), yields

$$y^2 = \frac{1+\zeta}{2}\left[s\alpha_3 - s\alpha_2 c\alpha_3 - s\alpha_3(1+c\alpha_2)\zeta\right]^2 \tag{5.29}$$

and eliminating θ_2 from the first and third equations, yields

$$x^2 = \frac{1-\zeta}{2}\left[s\alpha_3 + s\alpha_2 c\alpha_3 + s\alpha_3(1+c\alpha_2)\zeta\right]^2 \tag{5.30}$$

where $\zeta = (c\alpha_2 c\alpha_3 - z)/s\alpha_2 s\alpha_3$

Equations (5.29) represents a cylinder with a cubic directrix in the Y-Z plane.

Similarly, Eq. (5.30) also represents a cylinder with a cubic directrix in the X-Z plane. The cubic curve is called *Tschirnhausen's Cubic* or *l'Hospital's Cubic.* Hence, we may consider the trajectory as the intersection of a cubic cylinder and a unit sphere. From the two equations, it can be concluded that the curve has two planes of symmetry, the X-Z plane and the Y-Z plane.

5.5.2 Extrema, nodes, and cusps

Extrema of z

When the gear ratio is equal to two, the stationary condition for z coordinate is

$$\frac{dz}{d\theta_2} = 2s(2\theta_2)s\alpha_2 s\alpha_3 = 0 \tag{5.31}$$

Considering the second-order derivative of z, we may conclude that, when $\theta_2 = -\pi/2$ and $\theta_2 = \pi/2$, z reaches its maximum, z_{max}. Substituting them into Eq. (5.28), we obtain, for $\theta_2 = -\pi/2$

$$\vec{P}_{z_{max}} = \begin{bmatrix} -s(\alpha_2 - \alpha_3) \\ 0 \\ c(\alpha_2 - \alpha_3) \end{bmatrix} \tag{5.32}$$

and for $\theta_2 = \pi/2$

$$\vec{P}_{z_{max}} = \begin{bmatrix} s(\alpha_2 - \alpha_3) \\ 0 \\ c(\alpha_2 - \alpha_3) \end{bmatrix} \tag{5.33}$$

Substituting $\theta_2 = 0$ into Eq. (5.28), we obtain the minimum of z

$$\vec{P}_{z_{min}} = \begin{bmatrix} 0 \\ -s(\alpha_2 + \alpha_3) \\ c(\alpha_2 + \alpha_3) \end{bmatrix} \tag{5.34}$$

and for $\theta_2 = \pi$

$$\vec{P}_{z_{min}} = \begin{bmatrix} 0 \\ s(\alpha_2 + \alpha_3) \\ c(\alpha_2 + \alpha_3) \end{bmatrix} \tag{5.35}$$

Note that the two vectors with maximal values of z lie on the X-Z plane, and are symmetric with respect to the Y-Z plane; while the two vectors with minimal values of z lie on the Y-Z plane, and are symmetric with respect to the X-Z plane.

Extrema of y

The stationary condition for y coordinate is found by letting

$$\frac{dy}{d\theta_2} = s\theta_2[-6s^2\theta_2 s\alpha_3(1 + c\alpha_2) + 4s\alpha_3(1 + c\alpha_2) + s(\alpha_2 + \alpha_3)] = 0 \tag{5.36}$$

The vectors with extreme values of y can be found by substituting the solutions of Eq. (5.36) into (5.28). There are at least two and, at most six, solutions to Eq. (5.36). When $\theta_2 = 0$ (or $\theta_2 = \pi$), the curve has minimal (or maximal) value of y. Four additional solutions exist only if

$$0 \le \frac{2}{3} + \frac{s(\alpha_2 + \alpha_3)}{6s\alpha_3(1 + c\alpha_2)} \le 1 \tag{5.37}$$

Equation (5.37) can be simplified as

$$-2 \le \frac{s(\alpha_2 + \alpha_3)}{2s\alpha_3(1 + c\alpha_2)} \le 1 \tag{5.38}$$

Points of intersection at planes of symmetry

(i) The X-Z plane

The points of intersection at the X-Z plane can be obtained by equating the y component of Eq. (5.28) to zero, i.e.,

$$c\theta_2[2s^2\theta_2 s\alpha_3(1+c\alpha_2) - s(\alpha_2+\alpha_3)] = 0$$

Hence,

$$\theta_2 = -\pi/2 \text{ or } \pi/2 \tag{5.39.a}$$

or

$$\theta_2 = \sin^{-1}\left[\pm\left(\frac{s(\alpha_2+\alpha_3)}{2s\alpha_3(1+c\alpha_2)}\right)^{\frac{1}{2}}\right] \tag{5.39.b}$$

Equation (5.39.a) implies that the trajectory intersects the X-Z plane at least twice at the locations where the maximal values of z occur. Equation (5.39.b) yields four real solutions if

$$0 \leq \frac{s(\alpha_2+\alpha_3)}{2s\alpha_3(1+c\alpha_2)} \leq 1 \tag{5.40}$$

Since the denominator in Eq. (5.40) is always positive, the left-hand-side of Eq. (5.40) is satisfied when

$$\alpha_3 \leq \pi - \alpha_2 \tag{5.41}$$

Substituting the relationship $\alpha_2 = \alpha_s + \alpha_p$ into the right-hand-side of Eq. (5.40) and after simplification, yields

$$\frac{s(\alpha_s+\alpha_p-\alpha_3)}{s\alpha_3} \leq 2.$$

Comparing it with

$$\frac{\sin\alpha_s}{\sin\alpha_p} = 2,$$

we can see that when $\alpha_3 = \alpha_p$, the right equality sign of Eq. (5.40) is satisfied. For a given α_2, the function in Eq. (5.40) is a monotonically decreasing function of α_3

within the interval $0 < \alpha_3 < \pi$. Hence, it follows that

$$\alpha_3 \geq \alpha_p \tag{5.42}$$

will satisfy the right-hand-side of Eq. (5.40). Combining Eqs. (5.41) and (5.42), yields

$$\alpha_p \leq \alpha_3 \leq \pi - \alpha_2 \tag{5.43}$$

When Eq. (5.43) is satisfied, four additional points of intersection can be found by substituting $\sin\theta_2$ from Eq. (5.39.b) into (5.28). Since the x and z components of $\vec{P}$ depend only on $\sin\theta_2$, we conclude that the four additional points of intersection are two double points (nodes). When the equal sign in Eq. (5.43) holds, the two nodes become two cusps.

Since Eq. (5.40) is a subset of Eq. (5.38), it can be concluded that Eq. (5.43) also satisfy Eq. (5.38). Thus, when the trajectory intersects the X-Z plane six times, it has six extreme values of y.

(ii) The Y-Z plane

The points of intersection at the Y-Z plane can be obtained by equating the x component of Eq. (5.28) to zero, i.e.,

$$s\theta_2[2c^2\theta_2 s\alpha_3(1 + c\alpha_2) + s(\alpha_2 - \alpha_3)] = 0$$

Hence,

$$\theta_2 = 0 \text{ or } \pi \tag{5.44.a}$$

or

$$\theta_2 = cos^{-1}\left[\pm\left(\frac{s(\alpha_3 - \alpha_2)}{2s\alpha_3(1 + c\alpha_2)}\right)^{\frac{1}{2}}\right] \tag{5.44.b}$$

Equation (5.44.a) implies that the trajectory intersects the Y-Z plane at least twice at the locations where the minimal values of z occur. Equation (5.44.b) yields four real solutions if

$$0 \leq \frac{s(\alpha_3 - \alpha_2)}{2s\alpha_3(1 + c\alpha_2)} \leq 1 \tag{5.45}$$

The right-hand-side of Eq. (5.45) can be simplified as

$$-\frac{s(\alpha_s + \alpha_p + \alpha_3)}{s\alpha_3} \leq 2.$$

Comparing it with

$$\frac{\sin\alpha_s}{\sin\alpha_p} = 2,$$

it can be seen that when $\alpha_3 = \pi - \alpha_p$, the right equality sign of Eq. (5.45) is satisfied. For a given α_2, the function in Eq. (5.45) is a monotonically increasing function of α_3 within the interval $0 < \alpha_3 < \pi$. Hence, it follows that

$$\alpha_3 \leq \pi - \alpha_p$$

will satisfy the right-hand-side of Eq. (5.45). Hence, it can be concluded that Eq. (5.45) will be satisfied if and only if

$$\alpha_2 \leq \alpha_3 \leq \pi - \alpha_p \tag{5.46}$$

Since the y and z components of $\vec{P}$ depend only on $\cos\theta_2$, it is concluded that the four additional points of intersection are two double points (nodes).

Typical trajectories

Figure 5.5 shows some trajectories generated by spherical planetary gear trains having gear ratio equal to two. The curves are symmetric with respect to the X-Z

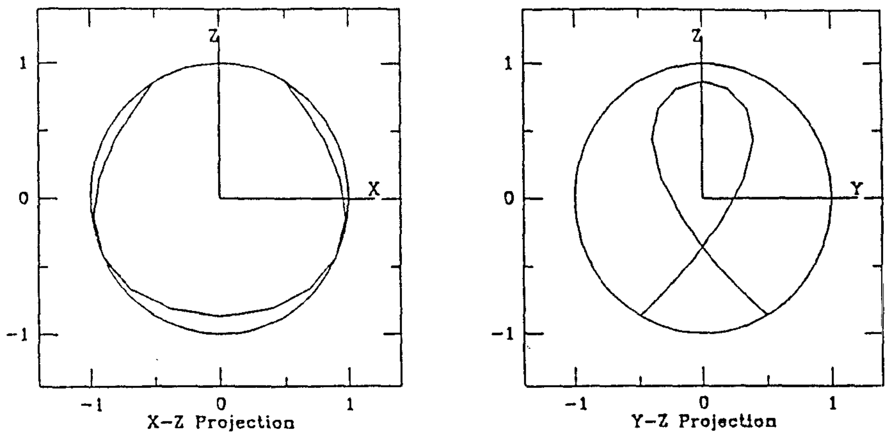

(a) $\alpha_2 = \pi/2, \quad \alpha_3 = \pi/3$

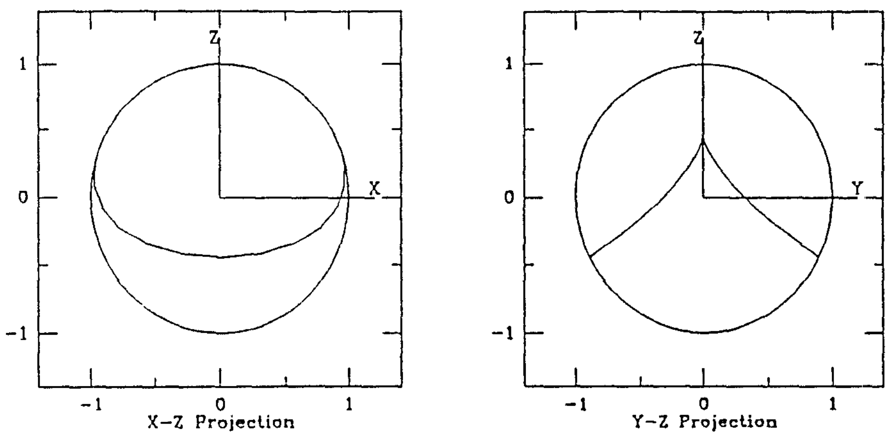

(b) $\alpha_2 = \pi/2, \quad \alpha_3 = 0.4636$

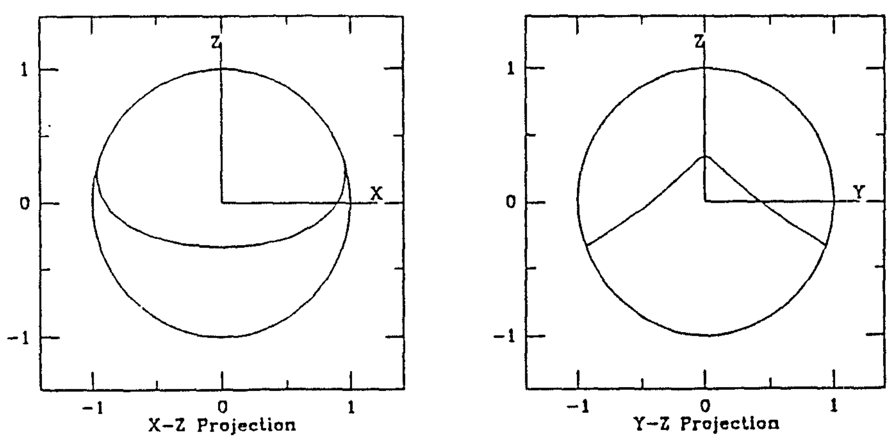

(c) $\alpha_2 = \pi/2, \quad \alpha_3 = \pi/9$

Figure 5.5 Trajectories generated by spherical planetary gear trains (n=2)

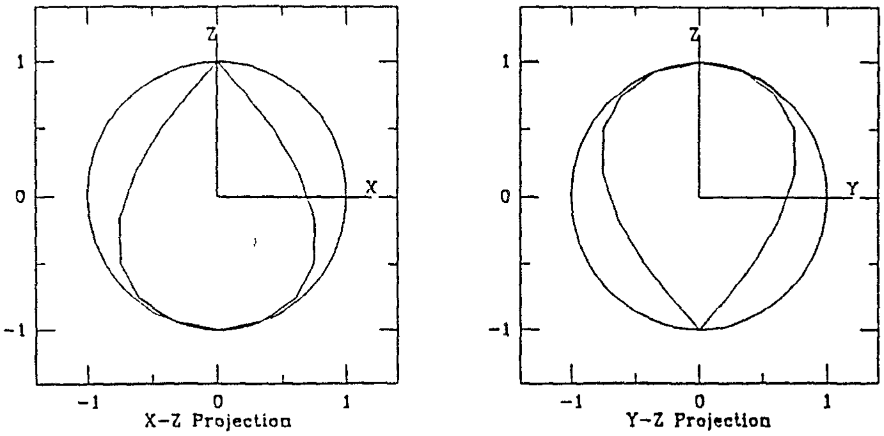

(d) $\alpha_2 = \pi/2, \quad \alpha_3 = \pi/2$

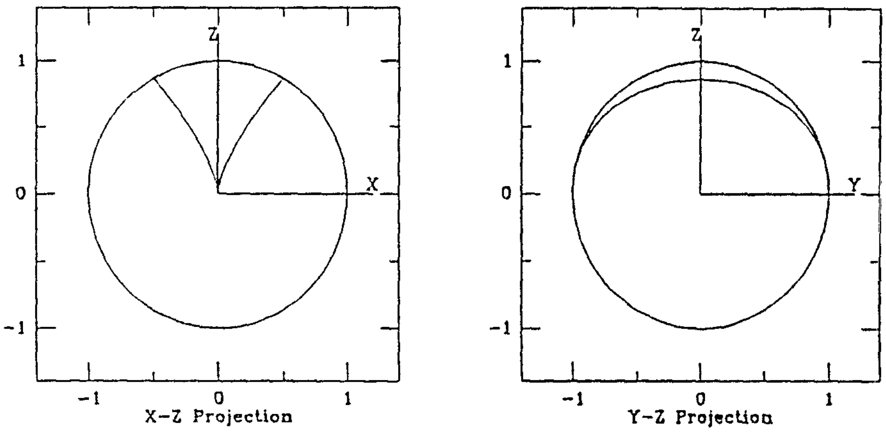

(e) $\alpha_2 = 2\pi/3, \ \alpha_3 = 5\pi/6$

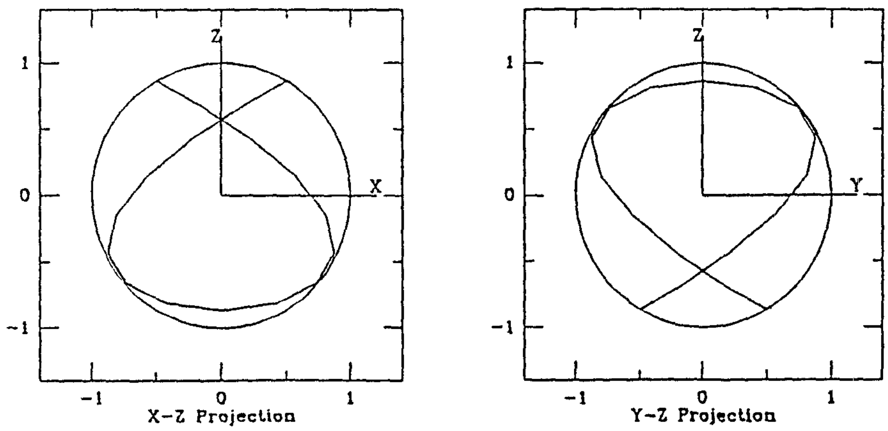

(f) $\alpha_2 = \pi/3, \quad \alpha_3 = \pi/2$

Figure 5.5 (Coutinued)

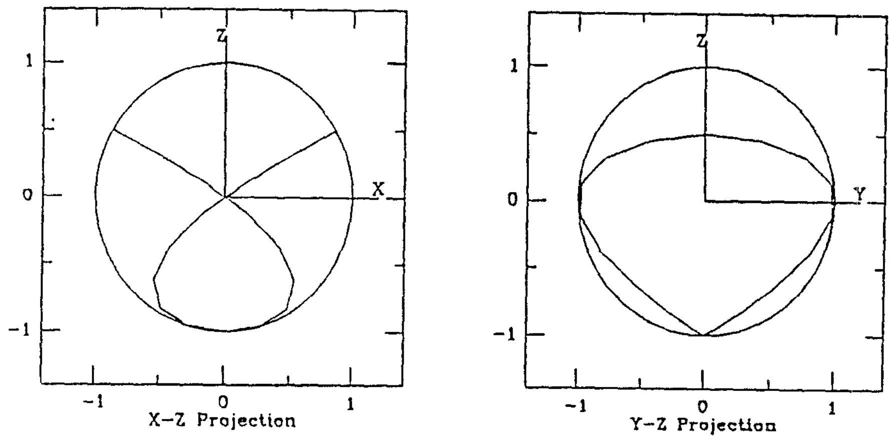

(g) $\alpha_2 = \pi/3, \quad \alpha_3 = 2\pi/3$

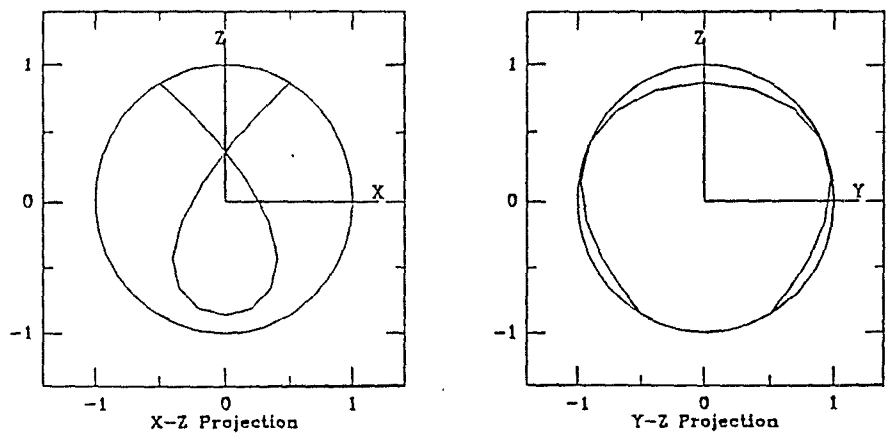

(h) $\alpha_2 = \pi/2, \quad \alpha_3 = 2\pi/3$

Figure 5.5 (Continued)

and Y-Z planes. It is noted that, given an α_2, the cone angle of the planet gear can be calculated by

$$\alpha_p = \tan^{-1}\left(\frac{s\alpha_2}{c\alpha_2 + 2}\right).$$

Except for Fig. 5.5(c), all the other figures satisfy Eqs. (5.43) and/or (5.46). In Fig. 5.5(b), $\alpha_3 = \alpha_p$, the curve has two cusps; and in Fig. 5.5(e), $\alpha_3 = \pi - \alpha_p$, the curve also has two cusps. These curves are called *spherical nephroids.* Note that when Eq. (5.43) is satisfied, there will be a node or cusp on the Y-Z projection; Similarly, when Eq. (5.46) is satisfied, there will be a node or cusp on the X-Z projection. Table 5.1 shows the number of nodes and cusps of the trajectories shown in Fig. 5.5, and their relationship with Eqs. (5.43) and (5.46). It is concluded that, Eq. (5.43) or (5.46) should be satisfied for the existence of any nodes or cusps.

	Nodes	Cusps	$\alpha_p < \alpha_3 < \pi - \alpha_2$	$\alpha_2 < \alpha_3 < \pi - \alpha_p$
Fig. 5.5(a)	2	0	$\surd$	
Fig. 5.5(b)	0	2	$\alpha_3 = \alpha_p$	
Fig. 5.5(c)	0	0		
Fig. 5.5(d)	2	0	$\alpha_3 = \pi - \alpha_2$	$\alpha_3 = \alpha_2$
Fig. 5.5(e)	0	2		$\alpha_3 = \pi - \alpha_p$
Fig. 5.5(f)	4	0	$\surd$	$\surd$
Fig. 5.5(g)	3	0	$\alpha_3 = \pi - \alpha_2$	$\surd$
Fig. 5.5(h)	2	0		$\surd$

Table 5.1: **The number of nodes or cusps and their relationship with Eqs. (5.43) and (5.46).**

5.6 Instantaneous screw axis

For a spherical planetary gear train (Fig. 5.2), given $\dot{\theta}_2$, the angular velocity of link 3 with respect to the base link can be expressed in the $(XYZ)_1$ coordinate system as:

$$
\begin{aligned}
{}^1\vec{\omega}_3 &= \dot{\theta}_2\vec{Z}_1 + \dot{\theta}_3\vec{Z}_2 \\
&= \dot{\theta}_2(\vec{Z}_1 + n\vec{Z}_2)
\end{aligned}
$$

$$
= \dot{\theta}_2 \begin{bmatrix} ns\theta_2 s\alpha_2 \\ -nc\theta_2 s\alpha_2 \\ (1 + nc\alpha_2) \end{bmatrix} \tag{5.47.a}
$$

The magnitude of ${}^1\vec{\omega}_3$ is equal to $\dot{\theta}_2\sqrt{1 + n^2 + 2nc\alpha_2}$, and its the direction is along the line of $(\vec{Z}_1 + n\vec{Z}_2)$. Hence, the line passing through the origin and pointing in the direction of $(\vec{Z}_1 + n\vec{Z}_2)$ is the instantaneous screw axis for the motion of link 3 with respect to link 1. As θ_2 varies from 0 to 2π, the locus of the instantaneous screw axis form a screw cone with its vertex located at the origin. Similarly, the angular velocity vector of link 3 with respect to link 1 can also be expressed in the moving coordinate system $(XYZ)_2$ as:

$$
{}^2\vec{\omega}_3 = \dot{\theta}_2 \begin{bmatrix} 0 \\ s\alpha_2 \\ c\alpha_2 + n \end{bmatrix} \tag{5.47.b}
$$

Equation (5.47.b) implies that the instantaneous screw axis is fixed in the Y-Z plane of the carrier. Hence, it revolves around the fixed Z_1-axis as the carrier rotates about the first joint axis.

5.7 Summary

This chapter discusses the trajectories of spherical planetary gear trains. Parametric equations for the trajectory are derived using 3×3 rotation matrix. It has been shown that the trajectory generated by a tracer point on the planet of a spherical planetary gear train is analogous to that of the planar gear train. When the gear ratio is equal to one, the trajectory is called spherical limacon or spherical cardioid depending on whether the tracer point lies on the outside of or on the pitch cone of the planet gear. When the gear ratio is equal to two and the tracer point lies on the pitch cone of the planet gear, the curve is a spherical nephroid.

The geometric properties of these trajectories are investigated, including the planes of symmetry, extent of curves, number of nodes (cusps) and their locations. It has also been shown that the criterion for the existence of cusps can be interpreted geometrically as the tracer point being on the pitch cone of the planet gear or its image cone. From the geometric point of view, the spherical limacon can be interpreted as the intersection of a parabolic cylinder and a unit sphere; and the spherical nephroid can be interpreted as the intersection of Tschirnhausen's cylinder and a unit sphere.

The results of this study will be applied to the study of orientational workspace of several three-DOF, four-jointed spherical wrist mechanisms in next chapter. It is also anticipated that this study can be helpful in the development of spherical kinematics.

Chapter 6

THE WORKSPACE OF THREE-DEGREE-OF-FREEDOM, FOUR-JOINTED SPHERICAL WRIST MECHANISMS

6.1 Introduction

Figure 6.1 shows three types of three-DOF, four-jointed wrist mechanisms in which the motion of: (i) links 2 and 3 are coupled, (ii) links 1 and 2 are coupled, and (iii) links 3 and 4 are coupled. In this chapter, the workspace associated with type (i) and (ii) mechanisms will be studied. However, type (iii) mechanism will not be discussed, because the end-effector can not possess an independent motion about the last joint axis. Motion such as drilling is not possible for such a wrist mechanism.

The workspace of a manipulator, as defined by Gupta and Roth [26], is the aggregate of all possible positions of a point attached to the free end of the manipulator. This definition of workspace is usually referred to as the reachable

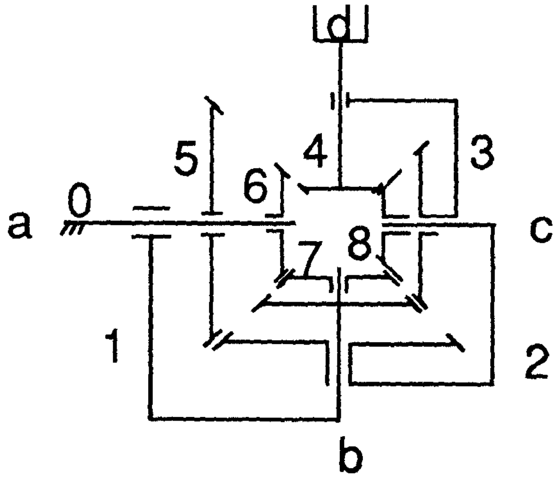

(a) links 2 & 3 coupled

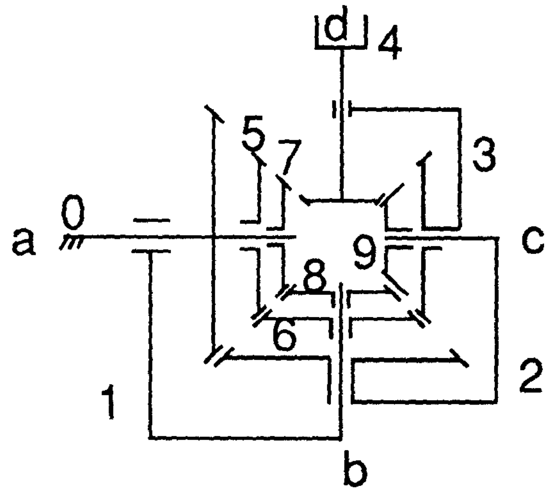

(b) links 1 & 2 coupled

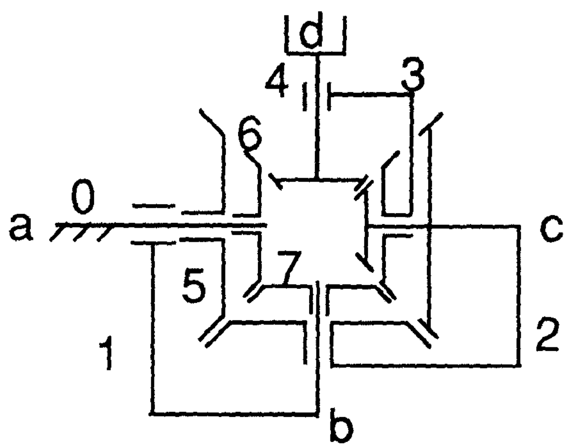

(c) links 3 & 4 coupled

Figure 6.1 Three-DOF, four-jointed bevel-gear-type spherical wrist mechanisms workspace. For orientational structures, the workspace can be defined in a similar manner, that is, the aggregate of all possible orientations of a frame attached to the end-effector of a manipulator. The orientation of a rigid body can be represented in many ways, such as Euler angles, roll-pitch-yaw angles, Euler parameters (unit quaternion), Rodrigues parameters, etc. Each representation has its advantages and disadvantages. If the approach vector $\vec{a}$ of an end-effector is coaxial with the last joint axis of a spherical wrist, then the orientation of the end-effector can be described by the direction of the last joint axis plus a rotation about it. Since the contribution to the workspace due to the last joint motion is always a constant, 2π, the workspace can be represented in a two dimensional space. Specifically, the spherical surface area swept by a point located on the last joint axis and one unit length away from the wrist center can be used to describe the workspace.

Workspace of three-jointed wrist mechanisms has been investigated by many researchers [27,33,47,55,58,65]. Some significant results have been derived from the application of Grashof-type conditions on spherical four-bar linkages. Gupta [27] derived general equations for the design of three-jointed spherical wrist mechanisms including non-zero twist angle of the gripper mount. It was concluded that maximal workspace can be obtained when the twist angle of the first two links is equal to $\pi/2$ and the joint axes intersect at a common point. Although the workspace associated with three-jointed wrist mechanisms has been studied extensively, the problem associated with three-DOF, four-jointed wrist mechanisms is completely new, and is the subject of this study.

6.2 Three-jointed wrist mechanisms

In what follows, it is assumed that (i) the joint axes intersect at a common point O called the wrist center, (ii) the twist angles of moving links (except the gripper mount) can not be zero or π, (iii) the twist angle of the gripper mount is zero, and (iv) mechanical interference will not be considered.

Figure 6.2 shows a general three-DOF, three-jointed spherical wrist mechanism. The origin of each coordinate system is located at the wrist center. However, they have been sketched away from the wrist center for the reason of clarity. The $(XYZ)_0$ coordinate system is fixed to the base link with the X_0-axis pointing out of the paper. The other link coordinate systems are defined according to the D-H convention. The stretched out, joint axes coplanar configuration of the mechanism has been chosen as the reference position, and defined all the positive X-axes to be pointing out of the paper. The end-effector coordinate system can be chosen arbitrarily as long as the approach vector $\vec{a}$ is in line with the last joint axis.

Under the condition of zero twist angle between the last joint axis and the Z-axis of the hand coordinate system, we may use a more direct method to determine the workspace. Figure 6.3 shows that the end point P of a unit vector along the last joint axis will trace over a unit sphere. Let $W_k(P)$ be the workspace of the end point P with respect to a frame fixed in the kth link. Then, the workspace $W_{k-1}(P)$ can be obtained by revolving $W_k(P)$ about Z_{k-1} axis as suggested by Gupta and Roth [26]. In the three-jointed case, $W_1(P)$ is a circle whose radius is equal to $sin(\alpha_2)$. The workspace $W_0(P)$ is obtained by revolving the circle $W_1(P)$ about Z_0-axis and, therefore, is a partial spherical surface area $\mathcal{A}$. This area is continuous and axisymmetric with respect to the first axis of rotation $\vec{Z}_0$. There

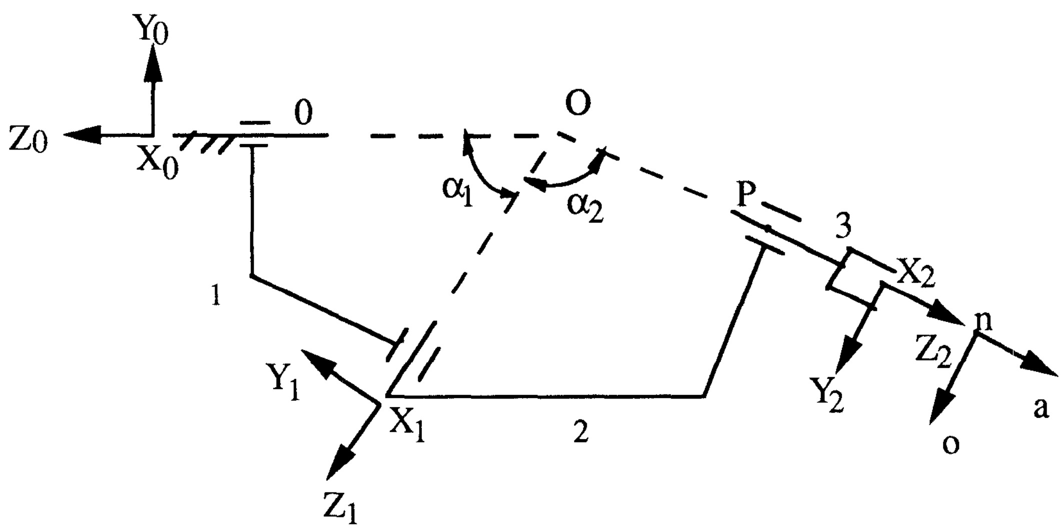

Figure 6.2 An open-loop, three-jointed spherical wrist mechanism

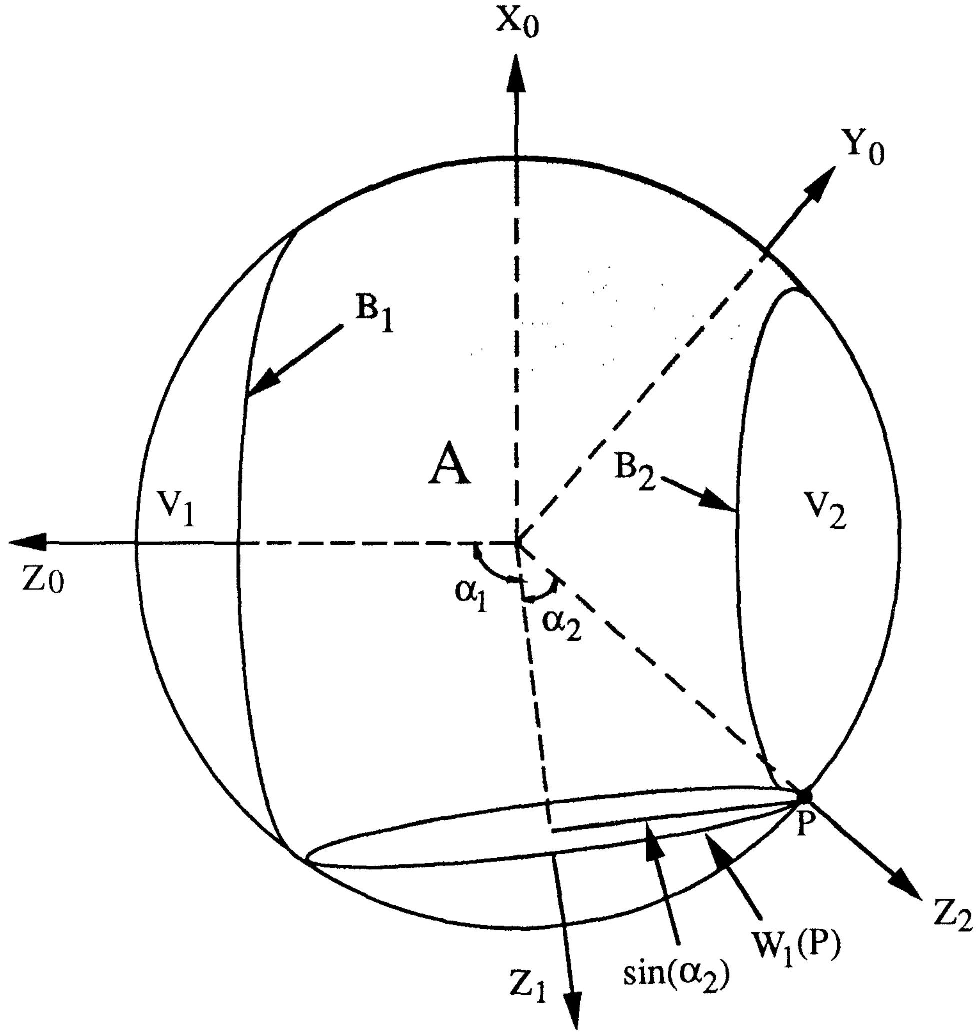

Figure 6.3 Workspace of a three-jointed spherical wrist mechanism

are two voids, V_1 and V_2, which are the aggregate of all unreachable orientations by the wrist mechanism. The boundaries, B_1 and B_2, are two circles centered at Z_0-axis, whose radii depend on the twist angles α_1 and α_2. Figure 6.3 shows that the radii of B_1 and B_2 are equal to $sin(\alpha_1 - \alpha_2)$ and $sin(\alpha_1 + \alpha_2)$, respectively. From the above analysis we can easily determine the orientational workspace, i.e. the shape of the area $\mathcal{A}$.

We may ask ourselves the following question. What are the twist angles required to produce a full orientational workspace, i.e. no voids on the sphere? The necessary and sufficient condition is that the radii of B_1 and B_2 are both equal to zero, that is,

$$s(\alpha_1 - \alpha_2) = 0 \qquad (6.1.a)$$

and

$$s(\alpha_1 + \alpha_2) = 0 \qquad (6.1.b)$$

where s is used to denote the sine function and c the cosine function.
The only solution for the above equations is $\alpha_1 = \alpha_2 = \pi/2$. This result is identical to that obtained by Gupta [27], but the approach is simpler.

As another example, assume that only the front void V_2 is to be eliminated, then Eq.(6.1.b) yields $\alpha_1 + \alpha_2 = \pi$. The twist angles, $\alpha_1 = \pi/3$ and $\alpha_2 = 2\pi/3$, of Cincinnati-Milacron 3-Roll wrist satisfy this condition. This design allows all the three joints to have full rotation without mechanical interference.

The boundaries separating $\mathcal{A}$ and the two voids can also be derived by the Jacobian analysis [32]. It can be proved that, the accessibility for any point inside the workspace $\mathcal{A}$ is two, which means there are two inverse solutions corresponding to each given end-effector orientation. The accessibility for any point inside the void is zero. We may consider the boundary as a transition region separating two areas of different accessibility. The accessibility on the boundaries is one. A special case is when the boundary lies on the fixed axis of rotation $\vec{Z}_0$, which results in an infinite accessibility.

6.3 Three-DOF, four-jointed mechanisms with links 2 and 3 coupled

Figure 6.1(a) shows a three-DOF, four-jointed wrist mechanism. The mechanism contains three input links labeled as 1, 5 and 6, and four joint axes labeled as a, b, c, and d. The bevel gears attached to links 1 and 3 are used for coupling the relative motion of link 2 with respect to link 1 to that of link 3 with respect to link 2. All the other bevel gears are used for power transmission. Overall, this mechanism contains nine links, eight revolute joints, and five gear pairs. The four joint axes, a, b, c, and d, intersect at a common point. Hence, the end-effector, link 4, possesses a spherical motion with three degrees of freedom. Figure 6.4 shows a similar mechanism with all the driving and driven gears removed for the convenience of discussion. In what follows, we shall choose the gear ratio for coupling the motion of links 2 and 3 to be one.

6.3.1 Workspace analysis

For the mechanism shown in Fig. 6.4, links 1, 2, and 3 form a one-DOF spherical planetary gear train. The trajectory $W_1(P)$ traced by the end point of a

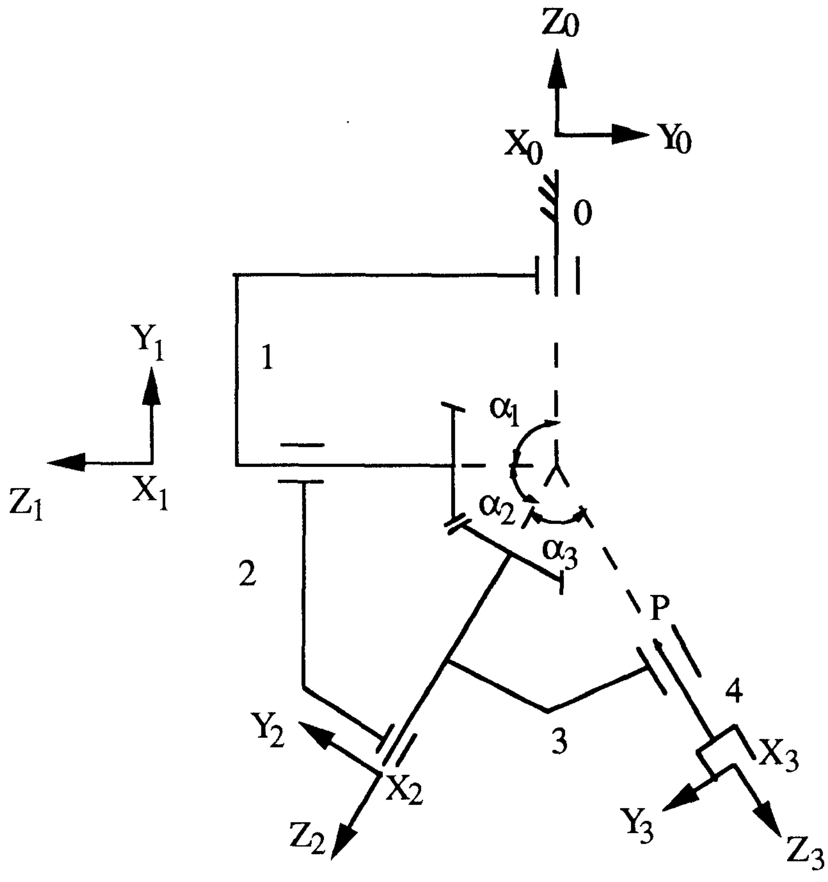

Figure 6.4 A four-jointed spherical wrist mechanism with links 2 and 3 coupled

unit vector $\vec{P}$ along the Z_3-axis and expressed in the $(XYZ)_1$ frame can be written as

$$^1\vec{P} = \begin{bmatrix} c\theta_2 s\theta_3 s\alpha_3 + s\theta_2 c\theta_3 c\alpha_2 s\alpha_3 + s\theta_2 s\alpha_2 c\alpha_3 \\ s\theta_2 s\theta_3 s\alpha_3 - c\theta_2 c\theta_3 c\alpha_2 s\alpha_3 - c\theta_2 s\alpha_2 c\alpha_3 \\ -c\theta_3 s\alpha_2 s\alpha_3 + c\alpha_2 c\alpha_3 \end{bmatrix} \tag{6.2}$$

where $\theta_3 = \theta_2 + \theta_p$, and where θ_p is a phase angle.

The analysis of such trajectory has been studied extensively in Chapter 5. Note that a leading superscript has been used to indicate the coordinate system in which the vector is expressed. A vector without a leading superscript indicates the vector is expressed in the base coordinate system $(XYZ)_0$.

In Fig. 6.4, $\alpha_1 = \pi/2$, $\alpha_2 = \alpha_3 = \pi/3$, and $\theta_p = 0$ has been chosen for the purpose of demonstration. The spatial drawing of $W_1(P)$ is shown in Fig. 6.5(a), and its Y_1Z_1 projection is shown in Fig. 6.5(b). The workspace $W_0(P)$ can be obtained by revolving $W_1(P)$ about the Z_0-axis.

Similar to three-jointed case, the workspace $\mathcal{A}$ has two voids V_1 and V_2, and two circular boundaries B_1 and B_2 separating the voids and the workspace as shown in Fig. 6.5(b). However, the workspace $\mathcal{A}$ is further divided into two regions of different accessibility by an inner (circular) boundary B_3. In Fig. 6.5(b), let a point P be located in the region between B_1 and B_3. Then, revolving the trajectory about the Y_1-axis will sweep point P four times per revolution. Hence the area between B_1 and B_3 has an accessibility of four. Similarly, the region between B_2 and B_3 has an accessibility of two.

In general, when $\theta_p = 0$ and the twist angles α_1, α_2 and α_3 are arbitrary, the coordinates of a unit position vector $\vec{P}$ along the Z_3-axis and expressed in the

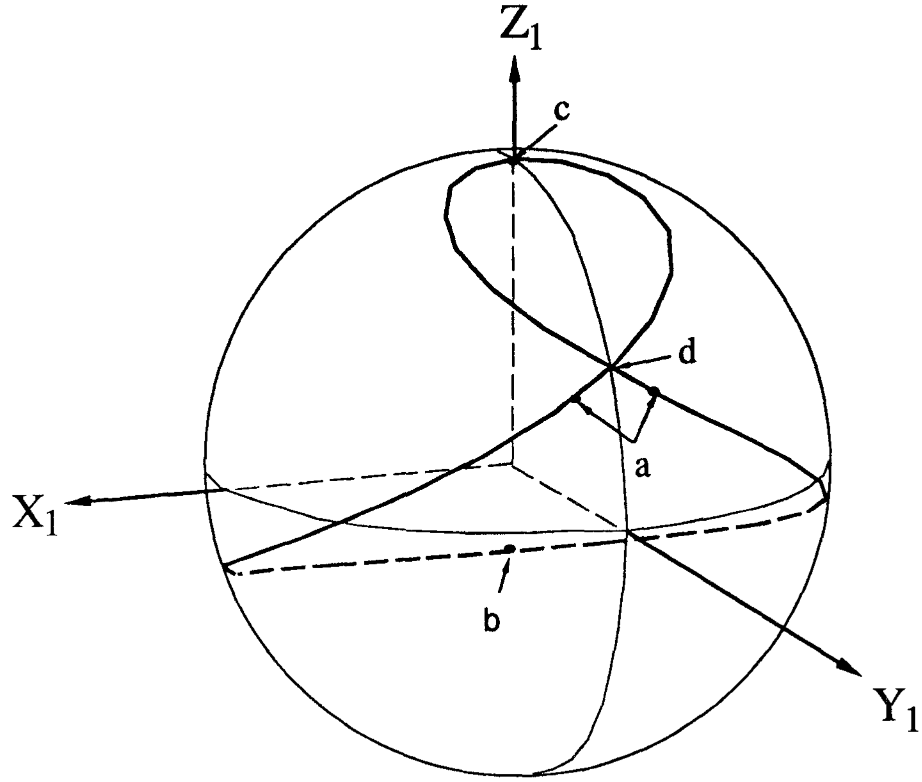

Figure 6.5(a) A spherical limacon with
$\alpha_2 = \pi/2$ and $\alpha_3 = \pi/3$

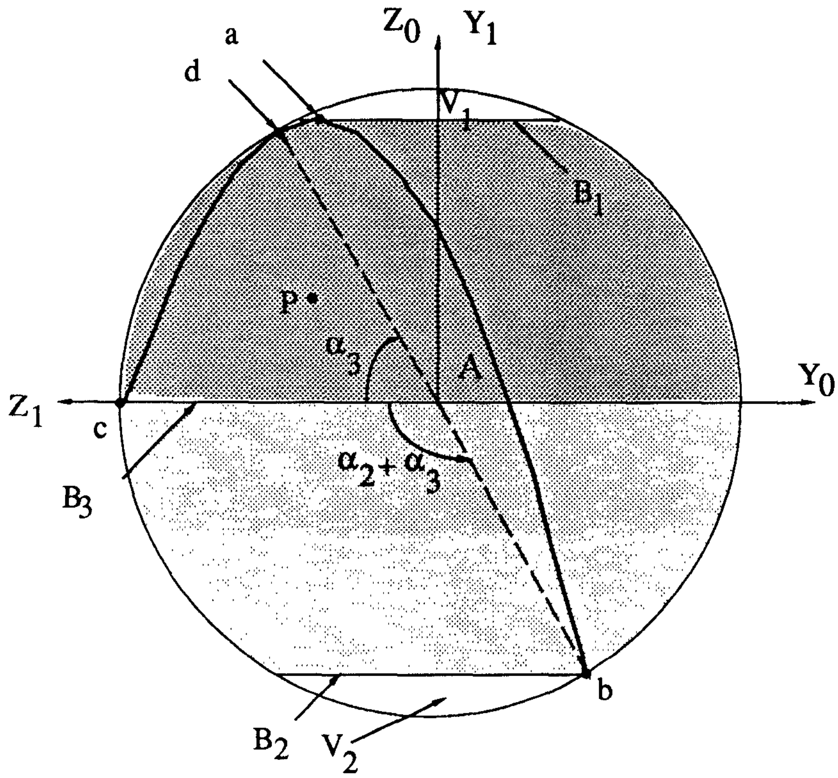

(b) Workspace generated by revolving the limacon about the Z-axis ($\theta_p = 0$)

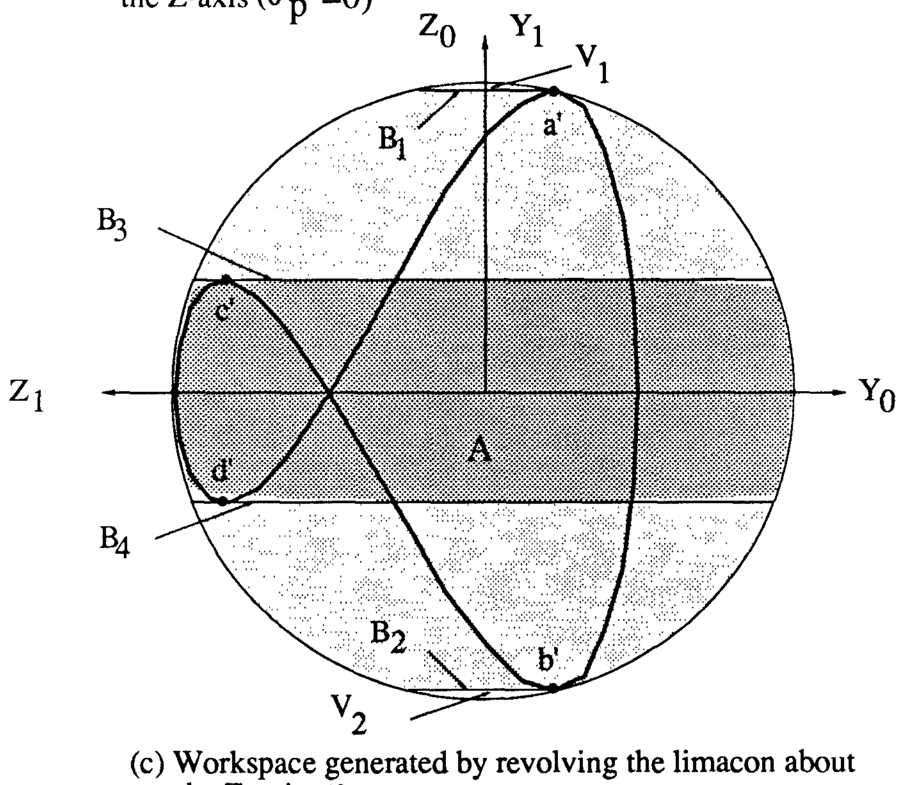

(c) Workspace generated by revolving the limacon about the Z-axis ($\theta_p = \pi/2$)

Figure 6.5

$(XYZ)_0$ system are given by

$$\begin{aligned}
\vec{P} &= \begin{bmatrix} c\theta_1 & -s\theta_1 c\alpha_1 & s\theta_1 s\alpha_1 \\ s\theta_1 & c\theta_1 c\alpha_1 & -c\theta_1 s\alpha_1 \\ 0 & s\alpha_1 & c\alpha_1 \end{bmatrix} \begin{bmatrix} c\theta_2 s\theta_3 s\alpha_3 + s\theta_2 c\theta_3 c\alpha_2 s\alpha_3 + s\theta_2 s\alpha_2 c\alpha_3 \\ s\theta_2 s\theta_3 s\alpha_3 - c\theta_2 c\theta_3 c\alpha_2 s\alpha_3 - c\theta_2 s\alpha_2 c\alpha_3 \\ -c\theta_3 s\alpha_2 s\alpha_3 + c\alpha_2 c\alpha_3 \end{bmatrix} \\
&= \begin{bmatrix} x \\ y \\ z \end{bmatrix} \qquad (6.3)
\end{aligned}$$

where $\theta_3 = \theta_2 + \theta_p$.

The z-component of $\vec{P}$ is independent of θ_1, and its extreme values can be derived by setting its first derivative to zero, i.e.

$$\begin{aligned}
\frac{dz}{d\theta_2} &= s\theta_2[2c\theta_2 s\alpha_3 s\alpha_1(1 + c\alpha_2) + s\alpha_2 s(\alpha_1 + \alpha_3)] \\
&= 0 \qquad (6.4)
\end{aligned}$$

Hence, the extreme values of z occur at:

$$\theta_2 = cos^{-1}\left(-\frac{s\alpha_2 s(\alpha_1 + \alpha_3)}{2s\alpha_1 s\alpha_3 (1 + c\alpha_2)}\right), \qquad (6.5.a)$$

$$\theta_2 = 0, \qquad (6.5.b)$$

and

$$\theta_2 = \pi. \qquad (6.5.c)$$

Equation (6.5.a) will not have real solutions if the absolute value in the argument of the arc cosine function is greater than one. Substituting the values of θ_2 from Eqs. (6.5.a), (6.5.b), and (6.5.c) into the third equation of Eq. (6.3), yields

$$z_a = s\alpha_1 s\alpha_3 + c\alpha_1 c\alpha_2 c\alpha_3 + \frac{s^2(\alpha_1 + \alpha_3)(1 - c\alpha_2)}{4s\alpha_1 s\alpha_3}, \qquad (6.6.a)$$

$$z_b = c(\alpha_1 + \alpha_2 + \alpha_3), \tag{6.6.b}$$

and

$$z_c = c(\alpha_1 - \alpha_2 + \alpha_3), \tag{6.6.c}$$

respectively. Since $W_0(P)$ is obtained by revolving $W_1(P)$ about the Z_0-axis, the boundaries B_i of $W_0(P)$ depend on the extreme values of z. The radius of the circular boundary B_1 is the shortest distance between point a and Z_0-axis, which is

$$R_{B_1} = \sqrt{1 - z_a^2} \tag{6.7.a}$$

Note that for $\theta_p = 0$, then $\theta_3 = \theta_2$ and the z-coordinate is a function of $\cos\theta_2$ only. Hence the two solutions of θ_2 given by Eq. (6.5.a) yield two points with the same z-coordinate. The solutions of θ_2 given by Eqs. (6.5.b) and (6.5.c) yield points b and c. The coordinates of points b and c can be derived by substituting Eqs. (6.5.b) and (6.5.c) into Eq. (6.3), respectively. Therefore, the radii of B_2 and B_3 are given by:

$$R_{B_2} = \sqrt{1 - z_b^2} = |s(\alpha_1 + \alpha_2 + \alpha_3)| \tag{6.7.b}$$

$$R_{B_3} = \sqrt{1 - z_c^2} = |s(\alpha_1 - \alpha_2 + \alpha_3)| \tag{6.7.c}$$

If the phase angle $\theta_p \neq 0$, the trajectory shown in Fig. 6.5(a) will be rotated an angle $-\theta_p$ about the Z_1-axis. For $\theta_p = \pi/2$, the $Y_1 Z_1$ projection of the resulting trajectory is shown in Fig. 6.5(c). Revolving the trajectory about the Z_0-axis (Y_1 axis), results in a workspace $W_0(P)$ with four circular boundaries. The two outer boundaries B_1 and B_2 separate the workspace $\mathcal{A}$ and the voids, and the two inner boundaries B_3 and B_4 divide the workspace $\mathcal{A}$ into three regions, two regions with an accessibility of two and one region with an accessibility of four. The radii of B_1 through B_4 can be derived by finding points a', b', c', and d' with extreme

z-coordinates. Equating the first derivative of z with respect to θ_2 to zero, yields

$$\begin{aligned} \frac{dz}{d\theta_2} &= s(2\theta_2+\theta_p)s\alpha_1 s\alpha_3(1+c\alpha_2)+s\alpha_2[s(\theta_2+\theta_p)c\alpha_1 s\alpha_3+s\theta_2 s\alpha_1 c\alpha_3] \\ &= 0 \end{aligned} \tag{6.8}$$

Equation (6.8) yields four solutions of θ_2 in the range of $-\pi < \theta_2 \leq \pi$. The solutions, $\tilde{\theta}_2$, of Eq. (6.8) define the positions of extreme points. Substituting $\tilde{\theta}_2$ and θ_p into Eq. (6.3), yields

$$\begin{aligned} z_i &= s\alpha_1[s\tilde{\theta}_{2_i}s(\tilde{\theta}_{2_i}+\theta_p)s\alpha_3 - c\tilde{\theta}_{2_i}c(\tilde{\theta}_{2_i}+\theta_p)c\alpha_2 s\alpha_3 - c\tilde{\theta}_{2_i}s\alpha_2 c\alpha_3] \\ &\quad + c\alpha_1[c\alpha_2 c\alpha_3 - c(\tilde{\theta}_{2_i}+\theta_p)s\alpha_2 s\alpha_3] \end{aligned} \tag{6.9}$$

The radii of the circular boundaries are:

$$R_{B_i} = \sqrt{1-z_i^2}, \qquad i = 1,2,3,4. \tag{6.10}$$

6.3.2 Kinematic synthesis

In the synthesis of four-jointed spherical wrist mechanisms with links 2 and 3 coupled, it is desirable to have the workspace as well as the four-root region as large as possible. The advantage of four-roots over two-roots is that a mechanism with four roots has more choices of postures to orient the end-effector.

The workspace is determined by three parameters, α_1, α_2 and α_3. Its circular boundaries, B_i, are related to the extreme values of z given by Eqs. (6.6.a)-(6.6.c), or Eq. (6.9). Hence, if $\theta_p = 0$, then given the radii of the boundaries R_{B_i}, the twist angles α_1, α_2, and α_3 can be obtained by solving Eqs. (6.6.a) through (6.6.c) simultaneously. Figure 6.5(b) gives us some insight about the workspace limitation.

Now suppose a full workspace is desired. What are the twist angles? A full workspace has no voids. Therefore, the trajectory has to pass through the $z_0 = \pm 1$ points. It has been shown in Chapter 5 that the trajectory intersects the $Y_1 Z_1$ plane at three points: b, c, and d, where b and c are the points having extreme z_1 coordinates, and point d is the node (double point) of the spherical limacon. The criterion for the spherical limacon to have a node is given by

$$\frac{\alpha_2}{2} < \alpha_3 < \pi - \frac{\alpha_2}{2} \tag{6.11}$$

The coordinates of the node, expressed in the $(XYZ)_1$ frame, are given by

$$^1\vec{P}_d = {}^1\vec{P}_{node} = \begin{bmatrix} 0 \\ s\alpha_3 \\ c\alpha_3 \end{bmatrix} \tag{6.12.a}$$

When $\theta_1 = \theta_p = 0$, it can be expressed in the $(XYZ)_0$ frame as

$$\vec{P}_d = \vec{P}_{node} = \begin{bmatrix} 0 \\ -s(\alpha_1 - \alpha_3) \\ c(\alpha_1 - \alpha_3) \end{bmatrix} \tag{6.12.b}$$

The coordinates of b and c, expressed in the $(XYZ)_1$ frame are given by:

$$^1\vec{P}_b = \begin{bmatrix} ^1x_b \\ ^1y_b \\ ^1z_b \end{bmatrix} = \begin{bmatrix} 0 \\ -s(\alpha_2 + \alpha_3) \\ c(\alpha_2 + \alpha_3) \end{bmatrix} \tag{6.13}$$

and

$$^1\vec{P}_c = \begin{bmatrix} ^1x_c \\ ^1y_c \\ ^1z_c \end{bmatrix} = \begin{bmatrix} 0 \\ s(\alpha_2 - \alpha_3) \\ c(\alpha_2 - \alpha_3) \end{bmatrix} \tag{6.14}$$

The angle ψ_z, measured from $\vec{P}_c$ to $\vec{P}_b$ in the clockwise direction, is given by

$$\psi_z = 2(\pi - \alpha_2) \tag{6.15}$$

There are three cases from which full workspace can be achieved:

Case (1): Z_0-axis passes through points b and c of the trajectory.

In this case, points b and c subtend the origin at an angle equal to π. Equating Eq. (6.15) to π yields

$$\alpha_2 = \pi/2 \tag{6.16.a}$$

Equating Eqs. (6.6.b) and (6.6.c) to -1 and +1, respectively, and eliminating α_2 from the two equations yields

$$\alpha_1 + \alpha_3 = \pi/2 \tag{6.16.b}$$

Case (2): Z_0 axis passes through points b and d of the trajectory.

In this case, points b and d subtend the origin at an angle equal to π. Taking the dot product of Eqs. (6.13), and (6.12.a) yields

$$^1\vec{P}_b \cdot {}^1\vec{P}_{node} = c(2\alpha_3 + \alpha_2) = -1.$$

Hence,

$$2\alpha_3 + \alpha_2 = \pi. \tag{6.17.a}$$

For the existence of a node, solving Eq. (6.17.a) for α_3 and then substituting it into Eq. (6.11), yields

$$\alpha_2 < \pi/2. \tag{6.17.b}$$

Equating the z-component of Eq. (6.12.b) to +1, yields

$$\alpha_1 = \alpha_3. \tag{6.17.c}$$

Case(3): Z_0 axis passes through points c and d of the trajectory.

In this case, points c and d subtend the origin at an angle equal to π. Taking the dot product of Eqs. (6.14), and (6.12.a) yields

$$^1\vec{P}_c \cdot {}^1\vec{P}_{node} = c(2\alpha_3 - \alpha_2) = -1.$$

Hence,

$$2\alpha_3 - \alpha_2 = \pi. \tag{6.18.a}$$

For the existence of a node, solving Eq. (6.18.a) for α_3 and then substituting it into Eq. (6.11), yields

$$\alpha_2 < \pi/2. \tag{6.18.b}$$

Equating the z-component of Eq. (6.12.b) to +1, yield

$$\alpha_1 = \alpha_3 \tag{6.18.c}$$

Note that α_1, α_2 and α_3 can not be 0 or π, in which case the mechanism will degenerate and lose one degree of freedom.

Hence, if $\theta_p = 0$, Eqs. (6.16.a)-(6.16.b), or Eqs. (6.17.a)-(6.17.c), or Eqs. (6.18.a)-(6.18.c) are the necessary conditions for a mechanism to have full workspace. For examples, for case (1) $\alpha_1 = \pi/6$, $\alpha_2 = \pi/2$, and $\alpha_3 = \pi/3$ satisfy Eqs. (6.16.a) and (6.16.b); for case (2) $\alpha_1 = \pi/3$, $\alpha_2 = \pi/3$, and $\alpha_3 = \pi/3$ satisfy Eqs. (6.17.a) (6.17.b) and (6.17.c); and for case (3) $\alpha_1 = 2\pi/3$, $\alpha_2 = \pi/3$, and $\alpha_3 = 2\pi/3$, satisfy Eqs. (6.18.a), (6.18.b) and (6.18.c). Among the three cases, case (1) has an accessibility of two for the entire workspace while cases (2) and (3) contain a four-root region. To maximize the four-root region for case (2), Eqs. (6.7.b) or (6.7.c) can be used for the determination of the inner boundary B_{in}. If $R_{B_{in}} = 0$, then two extreme cases occur. One is the entire workspace is a two-root region, the other is a entire four-root region. Substituting $R_{B_3} = 0$ in Eq. (6.7.c), and solving it simultaneously with Eqs. (6.17.a) and (6.17.c), we obtain two sets of solutions. One is $\alpha_1 = \alpha_3 = \pi/4$, and $\alpha_2 = \pi/2$; and the other is $\alpha_1 = \alpha_3 = \pi/2$, and $\alpha_2 = 0$. Although the latter is the solution for a maximum four-root region, it results in a degenerate mechanism. Case (3) is actually the mirror image of case

(2). Substituting $R_{B_2} = 0$ into Eq. (6.7.b), and solving it simultaneously with Eqs. (6.18.a) and (6.18.c), yields $\alpha_1 = \alpha_3 = \pi/2$, and $\alpha_2 = 0$ as the solution for an entire four-root workspace; and $\alpha_1 = \alpha_3 = 3\pi/4$, and $\alpha_2 = \pi/2$ for an entire two-root workspace.

If $\theta_p \neq 0$, the workspace is defined by four extreme points, namely, the z-coordinates of the centers of four circular boundaries, given by Eq. (6.9). The design is much more complicated than the $\theta_p = 0$ case.

6.3.3 Jacobian analysis

It is well-known that boundaries of workspace can be derived from Jacobian analysis. Jacobian curve (or surface) is defined as the space in which the rank of Jacobian matrix is lower than its order. When the determinant of Jacobian matrix becomes zero, there will be at least two equal roots of the characteristic polynomial [32], and the curves divide the workspace into regions of different accessibility. The angular velocity of the end effector, with respect to the $(XYZ)_0$ coordinate system and expressed in the $(XYZ)_1$, can be written as follows:

$$\begin{aligned}
{}^1\vec{\omega}_4 &= \dot{\theta}_{10}\vec{Z}_0 + \dot{\theta}_{21}\vec{Z}_1 + \dot{\theta}_{32}\vec{Z}_2 + \dot{\theta}_{43}\vec{Z}_3 \\
&= \dot{\theta}_{10}\vec{Z}_0 + \dot{\theta}_{21}\vec{Z}_1 + n\dot{\theta}_{21}\vec{Z}_2 + \dot{\theta}_{43}\vec{Z}_3 \\
&= \begin{bmatrix} \vec{Z}_0 & \vec{Z}_1 + n\vec{Z}_2 & \vec{Z}_3 \end{bmatrix} \begin{bmatrix} \dot{\theta}_1 \\ \dot{\theta}_2 \\ \dot{\theta}_4 \end{bmatrix}
\end{aligned} \tag{6.19}$$

where $n = \frac{N_1}{N_3}$ is the gear ratio, and $\vec{Z}_i$ is a unit vector in the Z_i-axis direction. Expressing the vector $\vec{Z}_0$, $\vec{Z}_1 + n\vec{Z}_2$ and $\vec{Z}_3$ in the $(XYZ)_1$ coordinate system, the

Jacobian matrix can be written as

$$J = \begin{bmatrix} 0 & ns\theta_2 s\alpha_2 & c\theta_2 s\theta_3 s\alpha_3 + s\theta_2 c\theta_3 c\alpha_2 s\alpha_3 + s\theta_2 s\alpha_2 c\alpha_3 \\ s\alpha_1 & -nc\theta_2 s\alpha_2 & s\theta_2 s\theta_3 s\alpha_3 - c\theta_2 c\theta_3 c\alpha_2 s\alpha_3 - c\theta_2 s\alpha_2 c\alpha_3 \\ c\alpha_1 & 1 + nc\alpha_2 & -c\theta_3 s\alpha_2 s\alpha_3 + c\alpha_2 c\alpha_3 \end{bmatrix} \tag{6.20}$$

where $\theta_3 = n\theta_2 + \theta_p$.

The three column vectors in the Jacobian matrix are the instantaneous screw axes of the wrist mechanism. If the rank of the Jacobian matrix becomes less than three, the three instantaneous screw axes become coplanar. The solutions of $det(J) = 0$ define the singular conditions and Jacobian curves. When n is equal to one, then the singular condition can be written as.

$$\begin{aligned} det(J) &= s\alpha_1 s\alpha_3(1 + c\alpha_2)s(2\theta_2 + \theta_p) + s\alpha_2[s\alpha_1 c\alpha_3 s\theta_2 + c\alpha_1 s\alpha_3 s(\theta_2 + \theta_p)] \\ &= 0, \end{aligned} \tag{6.21}$$

which is the same as Eq. (6.8). It has been shown that boundary curves can be obtained from either geometric consideration or Jacobian analysis.

6.4 Three-DOF, four-jointed mechanisms with links 1 and 2 coupled

Figure 6.1(b) shows another three-DOF, four-jointed wrist mechanism, where links 1, 5 and 7 are the input links. The bevel gears attached to links 0 and 2 are used to couple the relative motion of link 2 with respect to link 1 to that of link 1 with respect to link 0. All the other bevel gears are used for power transmission. The four joint axes, a, b, c, and d, intersect at a common point. Hence, the end-effector, link 4, possesses a spherical motion with three degrees of freedom. Figure 6.6 shows a similar mechanism with all the driving and driven gears removed

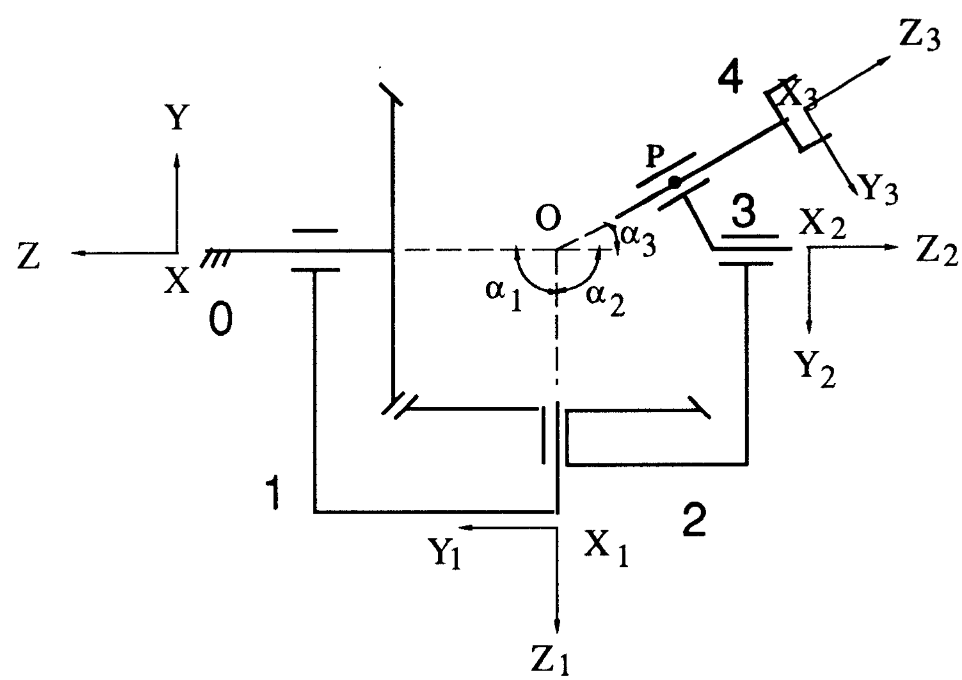

Figure 6.6 A four-jointed spherical wrist mechanism with links 1 and 2 coupled

from the mechanism. It can be clearly seen that links 0, 1, and 2 form a one-DOF spherical planetary gear train. In what follows, we shall choose the gear ratio for coupling the motion of links 1 and 2 to be one. Hence, the trajectory of a point on the third joint axis is a spherical limacon.

6.4.1 Workspace analysis

The workspace analysis for four-jointed spherical wrist mechanisms with links 1 and 2 coupled is more involved, since the approach of revolving $W_1(P)$ about Z_0-axis can no longer be used. In this case, $W_2(P)$ is a circle centered about the third joint axis, and its radius is equal to $\sin(\alpha_3)$. And the workspace $W_0(P)$ is obtained by integrating $W_2(P)$ for every point Q on the spherical limacon traced by first two links. The accessibility and boundaries of the workspace will be investigated from geometric consideration.

Figure 6.7(a) through 6.7(c) shows the spatial drawings of a typical workspace for this type of mechanisms. In Fig. 6.7(a), the twist angles are $\alpha_1 = \alpha_2 = \pi/2$, and $\alpha_3 = \pi/9$. Curve C is the spherical limacon traced by the end-point located on the third joint axis of link 2 and one unit away from the origin. The workspace $W_0(P)$ is obtained by sweeping $W_2(P)$ along C, which results in a figure-8 band on the sphere. Note that the spherical limacon C is the center-line of the band and the 'bandwidth' is $2\alpha_3$. The envelopes of all $W_2(P)$, B_1 and B_2, form the inner and outer boundaries of the workspace.

As shown in Fig. 6.7(a), the accessibility in the light-gray areas is two, because every point in these areas (except at the boundaries) are swept by $W_2(P)$

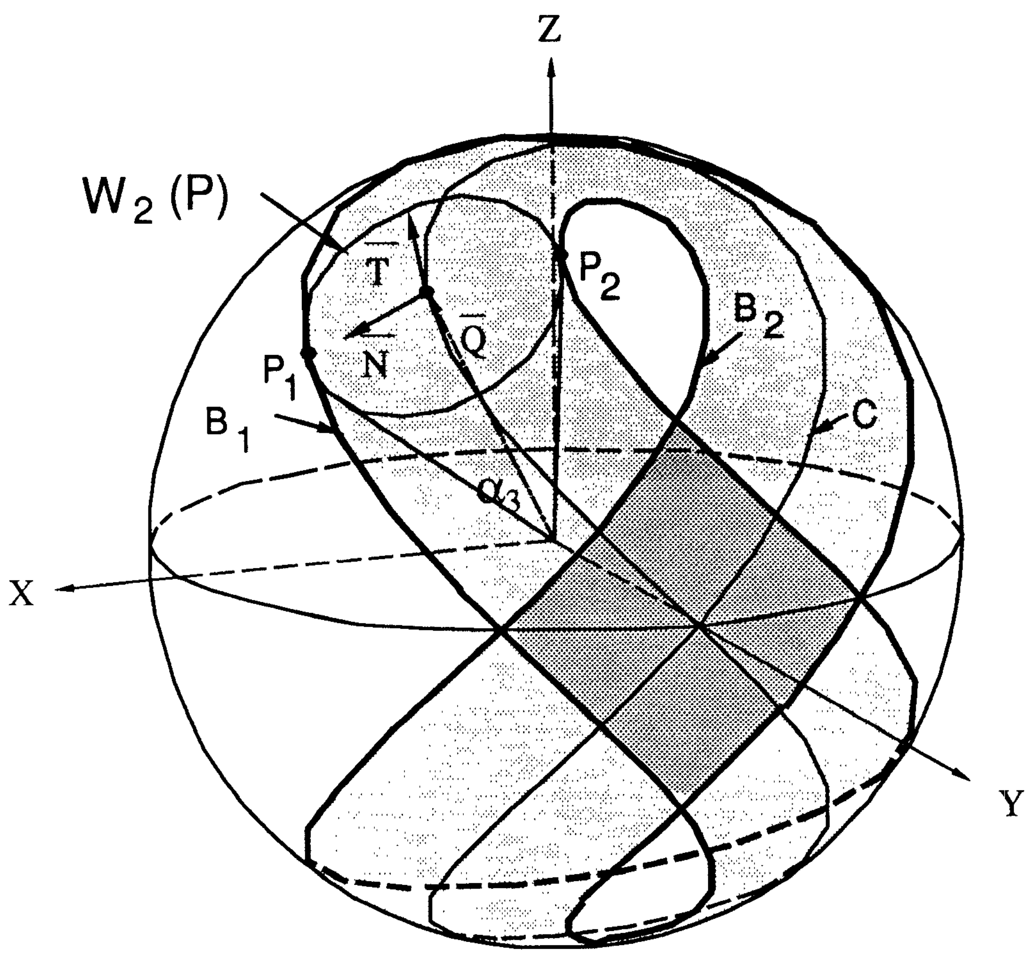

(a) $\alpha_1 = \pi/2$ $\alpha_2 = \pi/2$ $\alpha_3 = \pi/9$

Figure 6.7 Workspace generated by sweeping W_2 (P) along a spherical limacon $(\theta_p = 0)$

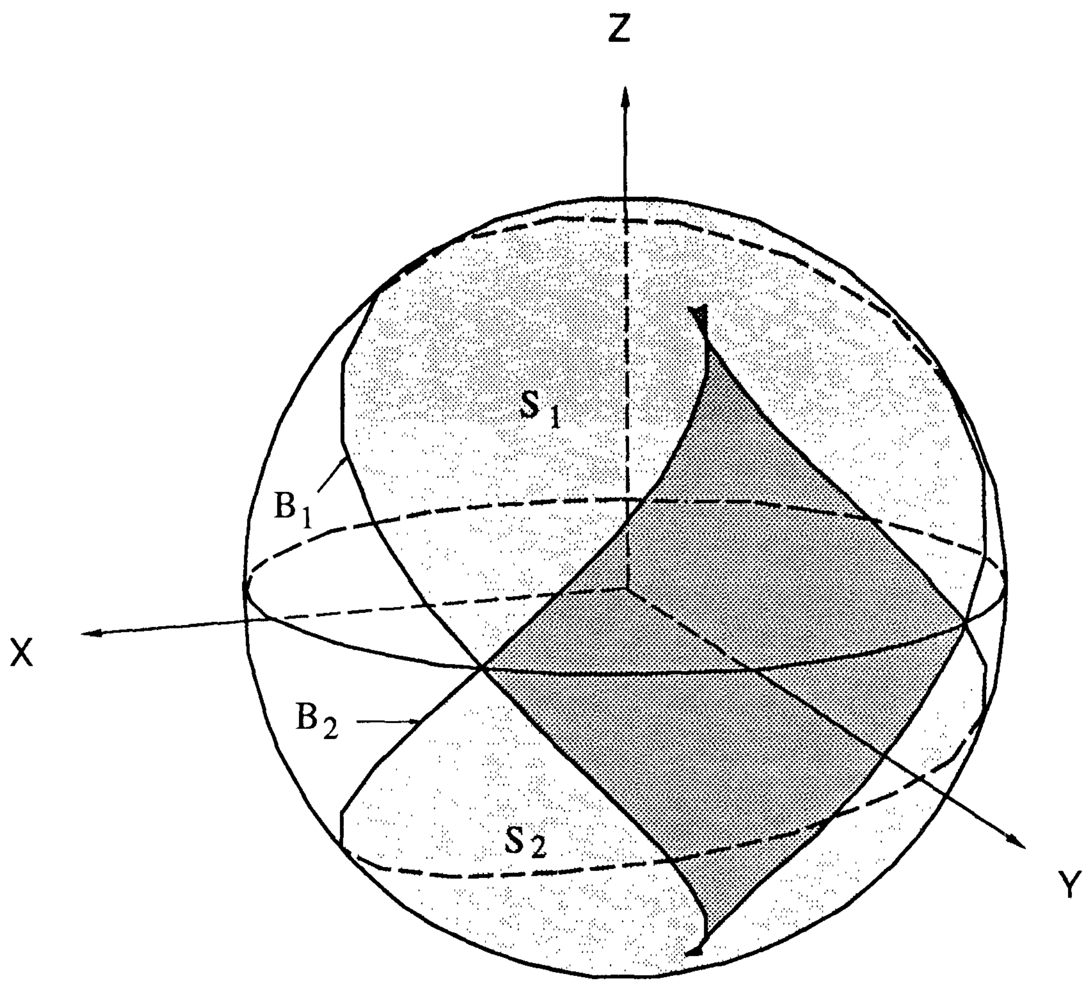

(b) $\alpha_1 = \pi/2 \qquad \alpha_2 = \pi/2 \qquad \alpha_3 = \pi/6$

Figure 6.7 (Continued)

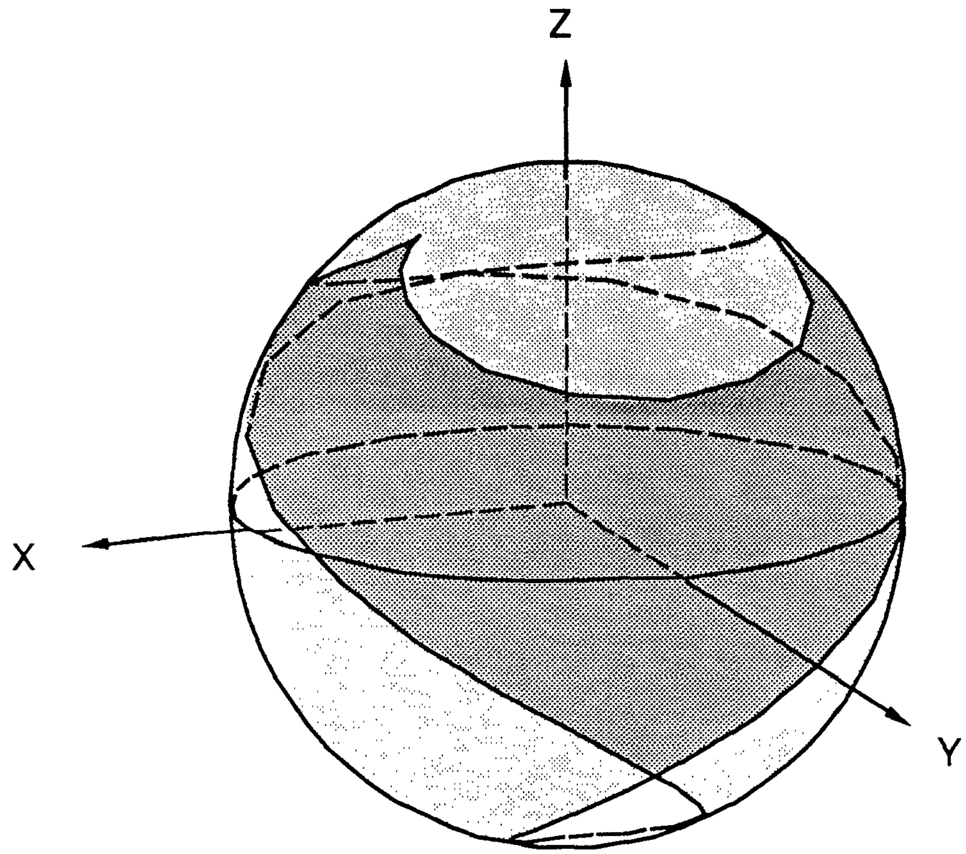

(c) $\alpha_1 = \pi/3$ $\alpha_2 = \pi/3$ $\alpha_3 = \pi/3$

Figure 6.7 (Continued)

twice for each cycle of θ_1; and the accessibility in the dark-gray area is four, since the band overlaps itself in that area. The white areas are voids. For the example, Fig. 6.7(a) shows three voids: two of them are 'inside' and the third is 'outside' the limacon, where the partial spherical surface within the figure-eight is defined as the interior of the spherical limacon. The accessibility on the boundary is one, except for the portions enclosing the dark-gray area where the accessibility is three.

From the above geometric discussion, the boundary curves, B_1 and B_2, can be found analytically. In Fig. 6.7(a), let Q be an arbitrary point on the spherical limacon. Then, for $\theta_p = 0$, the position vector of point Q can be written as a function of the twist angles and the first joint angle as

$$\vec{Q} = \begin{bmatrix} c\theta_1 s\theta_1 s\alpha_2 + s\theta_1 c\theta_1 c\alpha_1 s\alpha_2 + s\theta_1 s\alpha_1 c\alpha_2 \\ s^2\theta_1 s\alpha_2 - c^2\theta_1 c\alpha_1 s\alpha_2 - c\theta_1 s\alpha_1 c\alpha_2 \\ -c\theta_1 s\alpha_1 s\alpha_2 + c\alpha_1 c\alpha_2 \end{bmatrix} \tag{6.22}$$

Corresponding to each point Q, there are two boundary points, P_1 and P_2. According to a property in spherical geometry, the arc $\overset{\frown}{QP_1}$ (or $\overset{\frown}{QP_2}$) along the great circle is normal to C and B_1 (or B_2). The vector $\vec{T}$ tangent to C at point Q can be obtained by differentiating Eq. (6.22) with respect to θ_1, that is,

$$\vec{T} = \begin{bmatrix} (1 + c\alpha_1)s\alpha_2 c2\theta_1 + s\alpha_1 c\alpha_2 c\theta_1 \\ (1 + c\alpha_1)s\alpha_2 s2\theta_1 + s\alpha_1 c\alpha_2 s\theta_1 \\ s\alpha_1 s\alpha_2 s\theta_1 \end{bmatrix}_Q \tag{6.23}$$

The vector tangent to the great arc $\overset{\frown}{P_1P_2}$ at Q is normal to both $\vec{Q}$ and $\vec{T}$, i.e.

$$\vec{N} = \vec{Q} \times \vec{T} \tag{6.24}$$

Hence, the position vectors of P_1 and P_2 are given by

$$\vec{P}_1 = c\alpha_3\vec{Q} + \frac{s\alpha_3}{\|\vec{N}\|}\vec{N}, \tag{6.25}$$

and

$$\vec{P}_2 = c\alpha_3 \vec{Q} - \frac{s\alpha_3}{\|\vec{N}\|}\vec{N} \tag{6.26}$$

where $\|\vec{N}\|$ is the length of the vector $\vec{N}$.

Equations (6.25) and (6.26) provide the parametric forms of boundary curves.

As shown in Fig. 6.7(a), the shape of boundaries is closely related to that of the limacon and the twist angle α_3. If α_3 is small, there may be two voids inside the noded limacon, and the boundary curves B_1 and B_2 are parallel to the limacon C. In this case, the workspace forms a figure-eight band similar to the shape of the limacon. As α_3 increases, the inner voids become smaller and smaller, and finally disappear completely, leaving only an outer void. Figure 6.7(b) shows the case, $\alpha_3 = \pi/6$, for which the inner voids begin to disappear. If α_3 is further increased, till $\alpha_3 = \pi/2$, both inner and outer voids will completely disappear. As shown in Fig. 6.7(b), the workspace $W_0(P)$ can be thought of as the union of two bounded regions, S_1 and S_2. Each region is bounded by a curve, B_1 or B_2. The intersection of these two bounded regions forms a four-root region (dark-gray area). This approach of determining the accessibility of workspace only applies to situations where the spherical limacon has a node, and where there is no inner voids. It is also possible, however, that the outer void may disappear before the inner voids do. This situation usually occurs when α_1 is small. Figure 6.7(c) shows such an example.

Based on the above analysis, we may conclude that the workspace can be found by plotting the boundary curves given by Eqs. (6.25) and (6.26) and then find the area bounded by these two curves. Figures 6.8(a)-(f) show the workspace of mechanisms with their first two twist angles taken from the spherical planetary

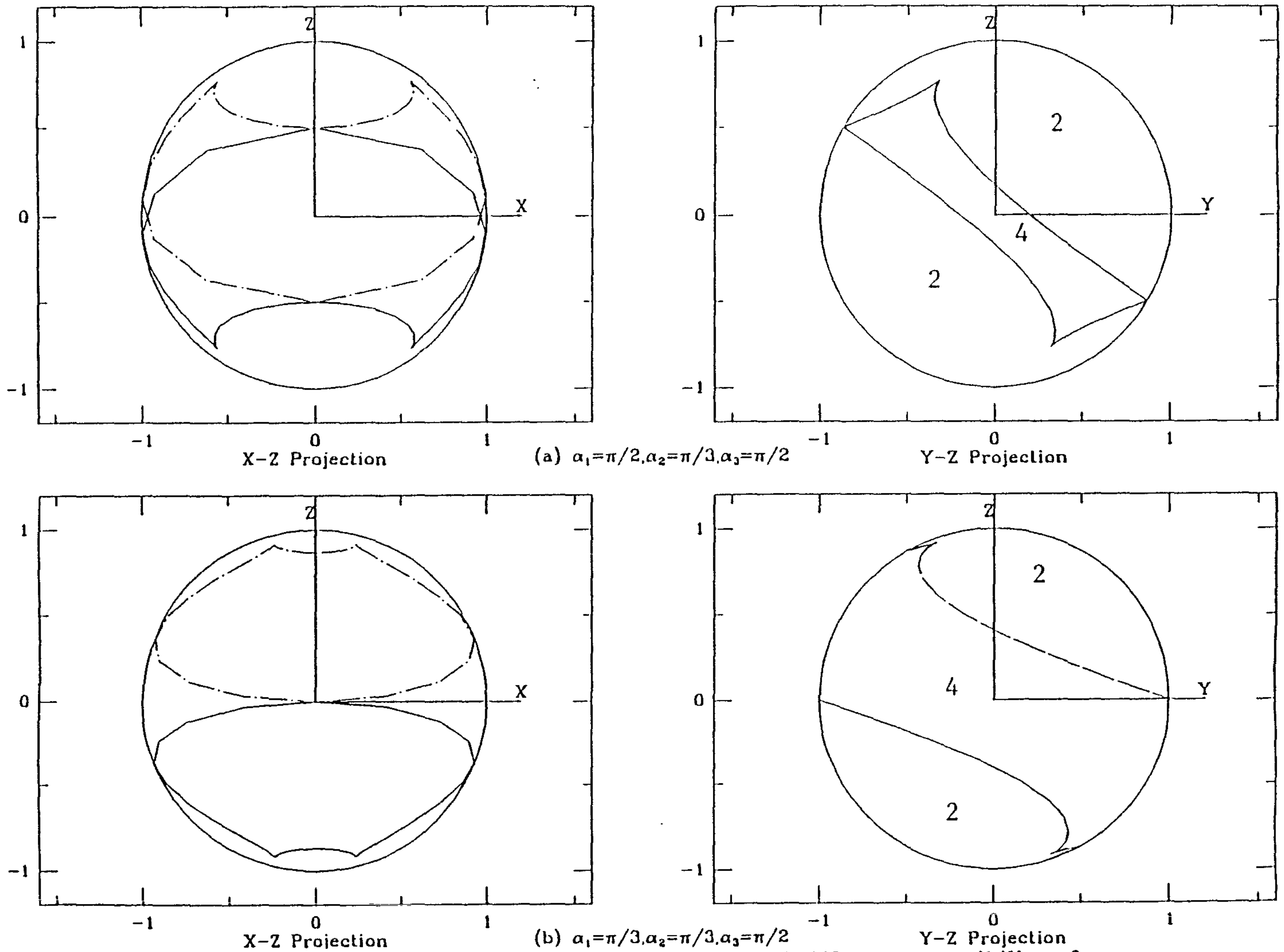

(a) $\alpha_1=\pi/2, \alpha_2=\pi/3, \alpha_3=\pi/2$

(b) $\alpha_1=\pi/3, \alpha_2=\pi/3, \alpha_3=\pi/2$

Figure 6.8 Boundary curves and areas of different accessibility of four-jointed spherical wrist mechanisms with links 1 and 2 coupled

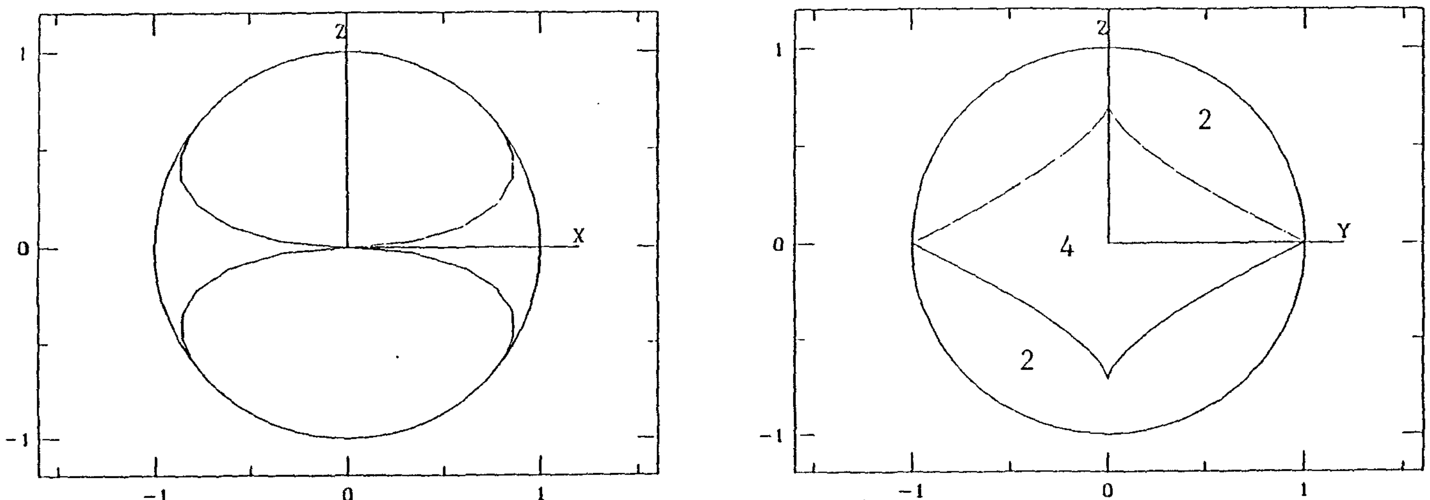

(c) $\alpha_1=\pi/2, \alpha_2=\pi/2, \alpha_3=\pi/2$

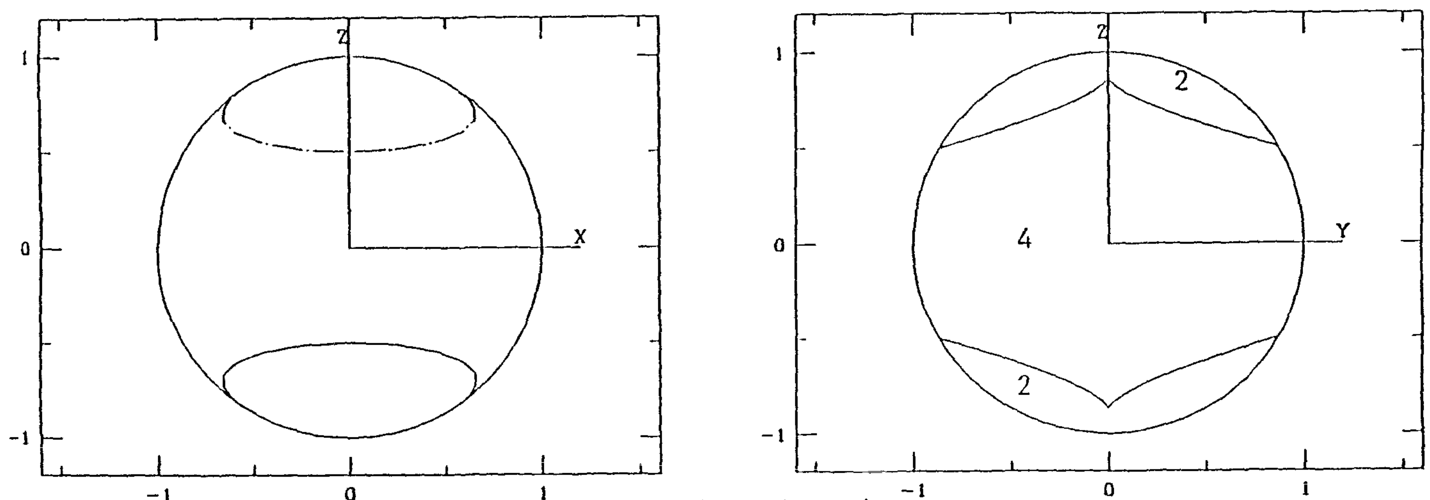

(d) $\alpha_1=\pi/3, \alpha_2=\pi/2, \alpha_3=\pi/2$

Figure 6.8 (Continued)

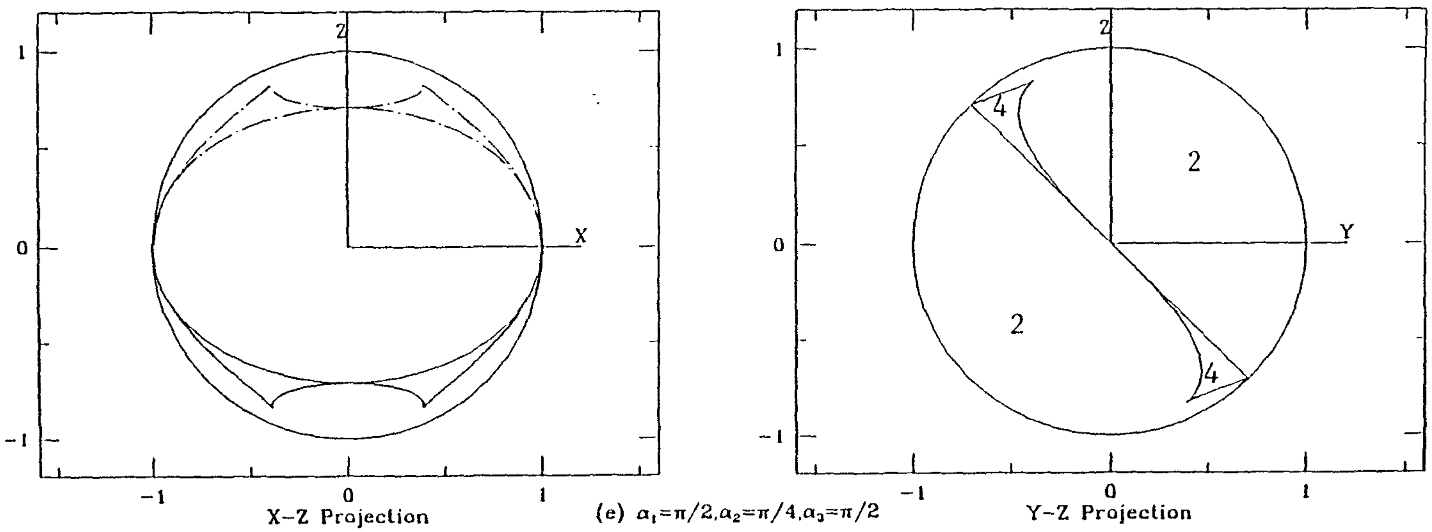

(e) $\alpha_1=\pi/2, \alpha_2=\pi/4, \alpha_3=\pi/2$

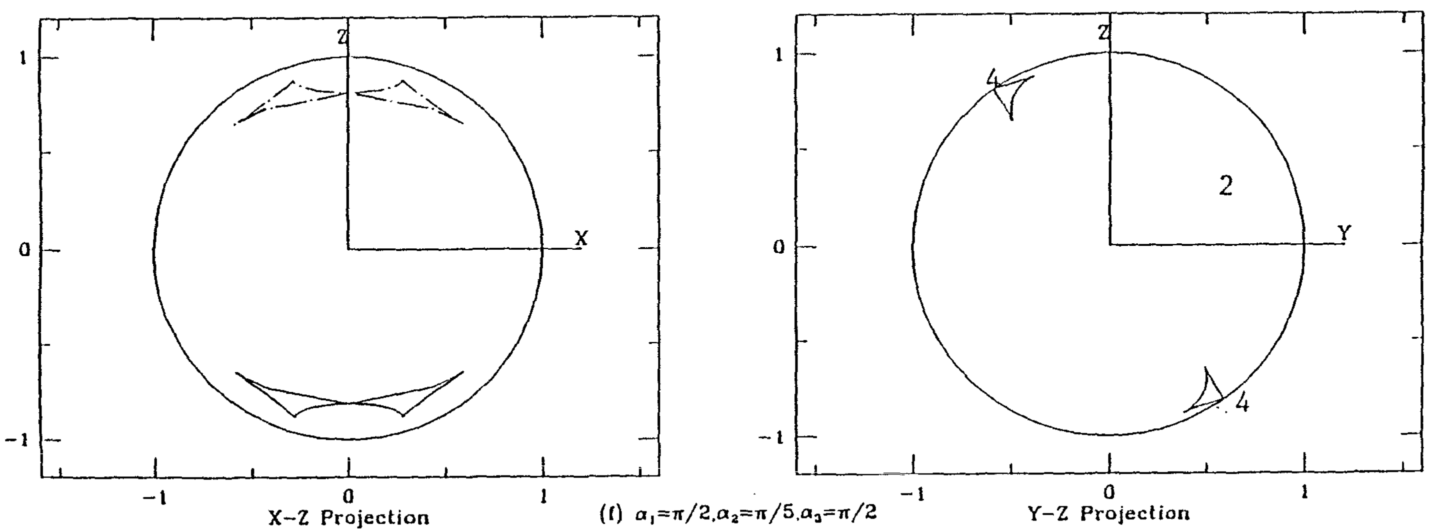

(f) $\alpha_1=\pi/2, \alpha_2=\pi/5, \alpha_3=\pi/2$

Figure 6.8 (Continued)

gear trains shown in Figs. 5.4(a)-(f) respectively, and with $\alpha_3 = \pi/2$. (Note that α_2 and α_3 in Fig. 5.4 correspond to α_1 and α_2 in Fig. 6.8.) In Figs. 6.8(a)-(d), there are two two-root regions separated by one four-root region; while in Figs. 6.8(e)-(f), there are two four-root regions separated by one two-root region. The difference is due to the criterion given by Eq. (6.11). The accessibility on the boundary curves is three, except for the cusps and those points having extreme y-coordinates where the accessibility is two. An inspection of Figs. 6.8(a)-(f) reveals that the workspace is symmetric with respect to the XY-plane when $\alpha_2 = \pi/2$, and the four-root region increases as α_1 decreases.

Since the workspace is obtained by sweeping $W_2(P)$ along the limacon, some geometric properties of the boundaries can be stated as follows:

P1 Adding a phase angle θ_p has the effect of rotating the workspace about Z_0-axis an angle $-\theta_p$.

P2 When $\theta_p = 0$, the workspace is symmetric about the Y-Z plane.

P3 When $\alpha_2 = \pi/2$, the workspace is symmetric about the X-Y plane.

P4 Given α_1 and α_2, maximum workspace is achieved if $\alpha_3 = \pi/2$.

P5 Given α_1 and α_2, the workspace derived for $\alpha_3 = \alpha_0$ is the mirror image of the workspace derived for $\alpha_3 = \pi - \alpha_0$.

P6 The workspace may have both inner and outer voids if α_3 is too small.

6.4.2 Kinematic synthesis

In the previous section, we have known that the workspace can be obtained by sweeping $W_2(P)$ along a spherical limacon. To achieve full workspace, the twist angles should be properly chosen so that there are no inner and outer voids. In what follows, we shall limit the angle α_3 to be no larger than $\pi/2$, because of the geometric properties **P4** and **P5** stated in the previous section. The following objectives will be explored for the workspace synthesis of three-DOF, four-jointed spherical wrist mechanisms with links 1 and 2 coupled: (i) to establish design criteria for full workspace, and (ii) to maximize the four-root regions.

As shown in Fig. 6.7(a), inner voids will exist if the radius of $W_2(P)$ is too small to cover the interior of the spherical limacon. Therefore, to eliminate inner voids, the twist angle α_3 should be greater than $\psi_x/2$, i.e.,

$$\alpha_3 \geq \psi_x/2 \tag{6.27}$$

where ψ_x is the angle between $\vec{Q}_{x_{max}}$ and $\vec{Q}_{x_{min}}$, and where $Q_{x_{max}}$ and $Q_{x_{min}}$ are the points on the spherical limacon having maximum and minimum x-coordinates, respectively. The locations of $\vec{Q}_{x_{max}}$ and $\vec{Q}_{x_{min}}$ can be found by substituting

$$\theta_1 = cos^{-1}\left(\frac{-u_1 \pm \sqrt{u_1^2 + 8u_0^2}}{4u_0}\right) \tag{6.28}$$

into Eq. (6.22), where $u_0 = s\alpha_2 + c\alpha_1 s\alpha_2$, and $u_1 = s\alpha_1 c\alpha_2$. Although there can be two $\vec{Q}'_{x_{max}}s$, and $\vec{Q}'_{x_{min}}s$, only the greater one is considered. Equation (6.27) can also be written in terms of the x-coordinates of $Q_{x_{max}}$ as follows:

$$\alpha_3 \geq sin^{-1}(x_{max}) \tag{6.29}$$

Similarly, to eliminate outer void only, it is necessary that

$$\alpha_3 \geq \pi - \psi_z/2, \tag{6.30}$$

where ψ_z is the angle measure from $\vec{Q}_{z_{max}}$ to $\vec{Q}_{z_{min}}$ in the clockwise direction, and is given by

$$\psi_z = 2(\pi - \alpha_1).$$

Hence, Eq. (6.30) can also be written as

$$\alpha_3 \geq \alpha_1 \tag{6.31}$$

Therefore, the necessary and sufficient condition to achieve a full workspace design is

$$\alpha_3 \geq Max(\alpha_1, sin^{-1}x_{max}) \tag{6.32}$$

For a given choice of α_1 and α_2, $\alpha_3 = \pi/2$ results in a largest workspace with no inner voids. Hence, by applying Eq. (6.31), it can be concluded that a sufficient condition for full workspace design is

$$\alpha_3 = \pi/2 \text{ and } \alpha_1 \leq \pi/2 \tag{6.33}$$

In general, ψ_x is a function of α_1 and α_2. Hence, for each α_2, we can use Eqs. (6.22) and (6.28) to compute ψ_x as a function of α_1. Figure 6.9 shows five such curves for $\alpha_2 = 50, 60, 70, 80, 90$ degrees, respectively. Also shown in Fig. 6.9 is the curve $\alpha_3 = \alpha_1$. The intersection of $\alpha_3 \geq \alpha_1$ and $\alpha_3 \geq \psi_x/2$ is the solution space satisfying full workspace consideration.

From previous analysis, it is known that a four-root region is the intersection of two bounded regions S_1 and S_2. Hence, a large $W_2(P)$ is a necessary condition for achieving large area of overlapping. In addition, when the limacon is symmetric

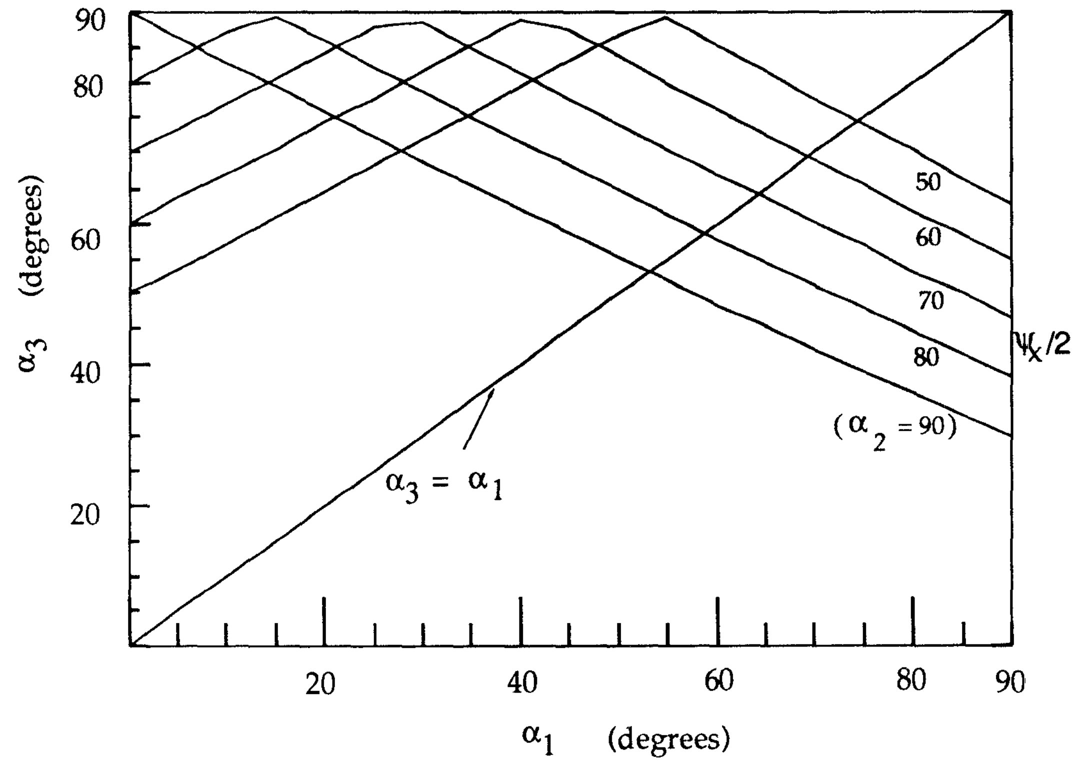

Figure 6.9 The criteria for full workspace design:

$\alpha_3 > \alpha_1$ and $\alpha_3 > \psi_x/2$

with respect to the XY plane, it will also produce larger overlapping area. Hence, it is necessary that $\alpha_2 = \alpha_3 = \pi/2$ in order to achieve a full workspace with maximum four-root region. With $\alpha_2 = \alpha_3 = \pi/2$, the smaller the angle α_1 is, the larger the four-root region is achieved. If $\alpha_1 = 0$, and $\alpha_2 = \alpha_3 = \pi/2$, the mechanism will have its entire spherical surface filled with four-root region. However, this results in a degenerated mechanism. The design shown in Fig. 5.8(d), ($\alpha_1 = \pi/3$, $\alpha_2 = \pi/2$,$\alpha_3 = \pi/2$), seems to be better than others. Its advantages are:

(i) It has a full workspace with large four-root region.

(ii) The inner boundary curves are symmetric about the X-Y, X-Z, and Y-Z planes. Hence, its mechanical performance in each quadrant is equal.

(iii) The undesirable singular point at $z = -1$ is avoided.

6.4.3 Jacobian analysis

The angular velocity of the end effector in a four-jointed wrist mechanism with links 1 and 2 coupled can be written as follows:

$$
\begin{aligned}
{}^1\vec{\omega}_4 &= \dot{\theta}_{10}\vec{Z}_0 + \dot{\theta}_{21}\vec{Z}_1 + \dot{\theta}_{32}\vec{Z}_2 + \dot{\theta}_{43}\vec{Z}_3 \\
&= \dot{\theta}_{10}\vec{Z}_0 + n\dot{\theta}_{10}\vec{Z}_1 + \dot{\theta}_{32}\vec{Z}_2 + \dot{\theta}_{43}\vec{Z}_3 \\
&= \begin{bmatrix} \vec{Z}_0 + n\vec{Z}_1 & \vec{Z}_2 & \vec{Z}_3 \end{bmatrix} \begin{bmatrix} \dot{\theta}_1 \\ \dot{\theta}_3 \\ \dot{\theta}_4 \end{bmatrix}
\end{aligned}
\tag{6.34}
$$

where n is the gear ratio $(\frac{N_Q}{N_2})$.

The Jacobian matrix can be expressed in the $(XYZ)_1$ coordinate system as

$$J = \begin{bmatrix} 0 & s\theta_2 s\alpha_2 & c\theta_2 s\theta_3 s\alpha_3 + s\theta_2 c\theta_3 c\alpha_2 s\alpha_3 + s\theta_2 s\alpha_2 c\alpha_3 \\ s\alpha_1 & -c\theta_2 s\alpha_2 & s\theta_2 s\theta_3 s\alpha_3 - c\theta_2 c\theta_3 c\alpha_2 s\alpha_3 - c\theta_2 s\alpha_2 c\alpha_3 \\ c\alpha_1 + n & c\alpha_2 & -c\theta_3 s\alpha_2 s\alpha_3 + c\alpha_2 c\alpha_3 \end{bmatrix} \tag{6.35}$$

where $\theta_2 = n\theta_1 + \theta_p$.

The column vectors in the Jacobian matrix represent three instantaneous screw axes for the motion of the wrist mechanism. Unlike those mechanisms with links 2 and 3 coupled, all the instantaneous screw axes change their directions with respect to the base link as the mechanism rotates. This property provides an advantage for this type of wrist mechanisms. That is, singular points at $z = \pm 1$ can be avoided. For other three-DOF wrist mechanisms, when the last joint axis is in line with the first axis, the mechanism will lose one degree of freedom, which severely limits the manipulability in the frontal working zone. Actually, singular points still exist for this type of mechanisms, they are those points having extreme y-coordinates as shown in Fig. 6.8. At those points, all four joint axes become coplanar, and the end-effector can not make an instantaneous rotation about the direction perpendicular to that plane.

When the gear ratio $n = 1$, the singular condition is

$$\begin{aligned} det(J) &= s\alpha_3[(c\alpha_1 s\alpha_2 + s\alpha_2 + s\alpha_1 c\alpha_2 c\theta_2)s\theta_3 + s\alpha_1 s\theta_2 c\theta_3] \\ &= 0 \end{aligned} \tag{6.36}$$

Equation (6.36) has infinite many solutions. Solving Eq. (6.36) for θ_3, we obtain

$$\theta_3 = \tan^{-1}\left(-\frac{s\alpha_1 s\theta_2}{c\alpha_1 s\alpha_2 + s\alpha_2 + s\alpha_1 c\alpha_2 c\theta_2}\right) \tag{6.37}$$

Equation (6.37) explicitly expresses the relation between θ_3 and θ_2 when the mechanism is at a singular point. Parametric equations for the singular points can be obtained by substituting Eq. (6.37) into (6.3), with $\theta_2 = \theta_1 + \theta_p$. The equations are very tedious and are not presented here. The Jacobian curves are actually the boundary curves, B_1 and B_2, derived in Eqs. (6.25) and (6.26).

6.5 Summary

The orientational workspace associated with two types of three-DOF, four-jointed spherical wrist mechanisms has been investigated. An important step in the workspace analysis is the derivation of the geometric properties associated with spherical planetary gear trains. It has been shown in Chapter 5 that the trajectory traced by a one-DOF, spherical planetary gear train is a spherical limacon. In this chapter, it has been shown that it is preferable for a spherical limacon to have a node and to be symmetrical in order to maximize the four-root region.

For three-DOF, four-jointed wrist mechanisms with links 2 and 3 coupled, the approach of revolving $W_1(P)$ about the fixed joint axis has been successfully applied to both analysis and synthesis problems. The relationship between the radii of boundary curves and the twist angles, and the criterion for full workspace design have been derived.

For three-DOF, four-jointed wrist mechanisms with links 1 and 2 coupled, the criteria for full workspace design and maximum four-root region have been established. This type of mechanisms has the advantage of avoiding its singular points to occur at $z = \pm 1$ locations. Therefore, the manipulability in the frontal working zone can be improved. Parametric equations for the workspace boundaries have been derived from both geometric consideration and Jacobian analysis. It is found that the boundaries consist of two branches of curves.

The advantage of four-jointed mechanisms is that the number of inverse solutions is greater than that of three-jointed mechanisms. Hence, without adding extra degrees of freedom, they can offer more choices of postures to orient the end-effector. Although singularities can not be fully eliminated, they can be located in a more desirable area by choosing the design parameters properly.

Chapter 7

CONCLUDING REMARKS

7.1 Review

This dissertation aimed to develop a novel class of robotic wrist mechanisms, and through dimensional synthesis to improve their kinematic performance. The research has been concerned with two aspects of bevel-gear-type robotic wrist mechanisms: (i) the kinematic structures and (ii) the workspace and singularities.

The research began with the structural analysis of an existing bevel-gear-type wrist mechanism. The purpose was to establish the fundamental requirements for this type of wrist mechanisms so that they could be used in the process of structural synthesis. It has been shown that a three-DOF bevel-gear-type wrist mechanism could be regarded as a non-fractionated, two-DOF gear train jointed with a single link. Hence, the structural synthesis of bevel-gear-type wrist mechanisms could be simplified into the problem of identifying the non-fractionated, two-DOF gear trains. Then a systematic methodology was developed for the enumeration of non-fractionated, two-DOF epicyclic gear trains. It has been shown that, for six-link chains, there are two blocks which have been labeled into three canonical displacement graphs. For seven-link chains, there are twenty blocks which have been labeled into fifty canonical displacement graphs. Then in Chapter 4, the fundamental requirements were applied in the examination of the atlas of non-fractionated two-DOF gear trains. The admissible kinematic structures of spherical wrist mechanisms with up to nine links have been categorized. In the atlas, three kinematic structures were identified to be existing ones. The others are considered to be new designs. In particular, for the first time, three-DOF, four-jointed bevel-gear-type wrist mechanisms have been synthesized. The mechanisms were further evaluated based on the singularity consideration. It was found that three-DOF, four-jointed wrist mechanisms were promising in improving the manipulability because (i) they had more inverse solutions than three-jointed wrist mechanisms, and (ii) the singularities could be relocated without reducing the workspace.

Three-DOF, four-jointed bevel-gear-type wrist mechanisms were further investigated regarding their workspace and singularities. Since the gear drive system did not affect the workspace, we could conveniently disregard the gear drives to simplify the kinematic structures. It was clear that the motion of such four-jointed mechanisms were constrained by a coupling gear, which guaranteed the inverse solutions to be determinate. It was noticed that there was a spherical planetary gear train imbedded in each four-jointed wrist mechanism. To study the workspace, it was concluded that the trajectories of spherical planetary gear trains first must be studied first. In Chapter 5, the geometric properties of the trajectories were derived. The analogy between the spherical and planar cases has been shown. The parametric equations for spherical limacons were derived. From the geometric point of view, the spherical limacon could be interpreted as the intersection of a parabolic cylinder and a unit sphere. It has been shown that the criterion for existence of cusps could be interpreted geometrically as the occurence of the tracer point on the pitch cone of the planet gear or its image cone. This criterion was useful for designing the workspace and determining number of inverse solutions for a four-jointed wrist mechanism with links one and two coupled. The workspace of three-DOF, four-jointed wrist mechanisms contained regions of accessibility four, two, and zero, which were divided by inner and outer boundaries. The workspace of a four-jointed wrist mechanism with links two and three coupled was obtained by revolving $W_1(P)$ about the Z_0-axis. Hence the boundaries were circles centered at the Z_0-axis, and the radii of boundaries could be determined by the extreme z-coordinates of the spherical limacon $W_1(P)$. The workspace of a four-jointed wrist mechanism with links one and two coupled was obtained by integrating all $W_2(P)$ along the spherical limacon. Parametric equations for the boundaries, which consists of two branches of curves, were derived. The criteria of full workspace design for both types of four-jointed wrist mechanisms were established. It was concluded that the designs which had whole four-root workspace were degenerate mechanisms. Finally, the superior wrist mechanism design was suggested. It is the four-jointed wrist mechanism with links one and two coupled, and with twist angles of $\alpha_1 = \pi/3, \alpha_2 = \pi/2$, and $\alpha_3 = \pi/2$.

Thus a systematic methodology to improve the kinematic performance of bevel-gear-type wrist mechanisms has been established. These design guidelines, criteria, and suggestions will help robot designers broaden their understanding of the kinematics of robotic wrist mechanisms.

7.2 Future work

This dissertation provides the knowledge required for the kinematic analysis and synthesis of bevel-gear-type robotic wrist mechanisms. To some extent, it is not only an intensive work, but also an extensive one. It has covered the areas of mechanisms structural analysis, topological synthesis, kinematic analysis (Jacobian analysis), trajectory analysis, workspace analysis and synthesis. However, there is no "completed" work in the research world. In the following paragraphs, several directions are proposed for future work.

1. When studying the workspace, it is assumed that the twist angle of an end-effector mount is zero, and that there is no link interference. In practice, link interference is a problem that should be taken into account, especially for four-jointed wrist mechanisms. For three-jointed wrist mechanisms, the problem has been investigated, while for three-DOF, four-jointed wrist mechanisms, it is still a good topic to be further explored.

2. To optimize the global manipulability, people traditionally consider every point in the workspace to be equally important. However, an end-effector usually works in the front working-zone for most of its working cycle. Therefore, we know some regions are more important than others. If we can define a weighting function, or a 'usage distribution function' for the workspace and incorporate it into the optimization process, then the global manipulability would be more meaningful.

3. The kinematics of four-DOF bevel-gear-type wrist mechanisms deserve further studies, including structural synthesis, kinematic analysis, and dimensional synthesis. In addition, dynamics and controls are also interesting problems.

4. A large number of non-fractionated, two-DOF epicyclic gear trains has been enumerated. It would be interesting to investigate if there are any other applications besides wrist mechanisms. A promising direction would be automotive transmissions. Other than that, we may consider mechanism designs on knees, necks, and knuckles of robotic applications.

5. It is suggested that the research be conducted regarding application of expert systems to the design of gear trains. The future direction of the study would be the determination of methodology for implementation of design rules into the knowledge base, so that the systems can learn, reason, and interactively provide the best knowledge for the designer.

6. Traditionally, we use linkage characteristic polynomials to identify kinematic structures of mechanisms. Is it possible to identify kinematic structures using the ideas of pattern recognition in computer vision, or some symbolic pattern instead of numerical one? This is a question to be answered.

Bibliography

[1] Angeles, J., 1985, *"On the Numerical Solution of the Inverse Kinematic Problem,"* The International Journal of Robotics Research, Vol. 4, No. 2, pp. 21-37.

[2] Angeles, J., and López-Cajún, C., 1988, *"The Dexterity Index of Serial-Type Robotic Manipulators,"* Proceedings of ASME 20th Biennial Mechanisms Conference, Sept. 25-28, Kissimmee, Florida, Vol. 3, pp. 79-84.

[3] Anonymous, Aug. 1982, *"Bevel Gears Make Robot's Wrist More Flexible,"* Machine Design, Vol. 54, No. 18, pp. 55.

[4] Asada, H., and Cro Granito, J.A., 1985, *"Kinematic and Static Characterization of Wrist Joints and Their Optimal Design,"* Proceedings of 1985 IEEE International Conference On Robotics and Automation, St. Louis, pp. 244-250.

[5] Berger, M., and Gostiaux, B., 1988, Differential Geometry: Manifolds, Curves, and Surfaces, Springer-Verlag, New York.

[6] Brady, M. (editor), 1989, Robotics Science, The MIT Press, Cambridge, MA.

[7] Brieskorn, E., and Knörrer, H, 1986, Plane Algebraic Curves, Birkhäuser Boston Inc.

[8] Buchsbaum, F., 1967, *"Structural Classification and Type Synthesis of Mechanisms With Multiple Elements,"* Eng. ScD dissertation, Columbia University,

publication 67-15479, University Microfilm, Inc., Ann Arbor, MI 1968.

[9] Buchsbaum, F., and Freudenstein, F., 1970, *"Synthesis of Kinematic Structure of Geared Kinematic Chains and Other Mechanisms,"* Journal of Mechanisms, Vol. 5, pp.357-392.

[10] Butchart, J. H., 1945, *"Some Properties of the Limacon and Cardioid,"* Amer. Math. Monthly, Vol. 52, pp. 384-387.

[11] Chang, S.L., and Tsai, L.W., 1989, *"Topological Synthesis of Articulated Gear Mechanisms,"* IEEE J. of Robotics and Automation, Vol. 6, No. 1, pp. 97-103.

[12] Chen, D.Z., and Tsai, L.W., 1990, *"Kinematic and Dynamic Synthesis of Geared Robotic Mechanisms,"* Proceedings of the ASME 21th Biennial Mechanisms Conference, Chicago, IL, DE-Vol. 26, pp. 397-404.

[13] Chiu, S.L., 1988, *"Kinematic Characterization of Manipulators: An Approach to Defining Optimality,"* Proceedings of 1988 International Conference On Robotics and Automation, Philadelphia, PA., IEEE, pp. 828-833.

[14] Crossley, F. R. E., Feb. 1965, *"A Contribution to Gruebler's Theory in the Number Synthesis of Plane Mechanisms,"* ASME Journal of Engineering for Industry, pp.1-5.

[15] Crossley, F. R. E., 1965, *"The Permutations of Kinematic Chains of Eight Members or Less From the Graph Theoretic Viewpoint,"* Development in Theoretical and Applied Mechanics, Vol. 2, Pergamon Press, pp. 467-486.

[16] Datseris, P., and Palm, W., 1984, *"Principles of the Development of Mechanical Hands Which Can Manipulate Objects by Means of Active Control,"* ASME

Journal of Mechanisms, Transmissions, and Automation in Design, Vol. 107, No. 2, pp. 148-156.

[17] Denavit, J., and Hartenberg, R.S., 1955, *"A Kinematic Notation for Lower Pair Mechanisms Based on Matrices,"* ASME Journal of Applied Mechanics, Vol. 77, pp. 215-221.

[18] Erdman, A. G., and Bowen, J., Dec. 1981, *"Type and Dimensional Synthesis of Casement Window Mechanism,"* Mechanical Engineering, Vol. 103, pp. 46-55.

[19] Fisher, W.D., 1984, *"The Kinematic Control of Redundant Manipulators,"* Ph.D. thesis, School of Electrical Engineering, Purdue University.

[20] Freudenstein, F., February 1971, *"An Application of Boolean Algebra to the Motion of Epicyclic Drives,"* ASME Journal of Engineering for Industry, Vol. 93, Series B, pp. 176-182.

[21] Freudenstein, F., and Maki, E. R., 1979, *"The Creation of Mechanisms According to Kinematic Structure and Function,"* The International Journal of Architecture and Design, Environment, and Planning, B, Vol. 6, pp. 375-391.

[22] Freudenstein, F., Longman, R. W., and Chen, C-K, 1984, *"Kinematic Analysis of Robotic Bevel-Gear Train,"* ASME J. of Mechanisms, Transmissions, and Automation in Design, Vol. 106, No. 3, pp. 371-375.

[23] Gibsons, A., 1985, Algorithmic Graph Theory, Cambridge University Press, Cambridge, London, Greattt Britain.

[24] Gosselin, C., and Angeles, J., 1987, *"The Optimum Kinematic Design of a Spherical Three-degree-of-freedom Parallel Manipulator,"* Proceedings of 13th Design Automation Conference, Boston Mass., Sept. 27-30, pp. 111-115.

[25] Gosselin, C., and Angeles, J., 1988, *"A New Performance Index for The Kinematic Optimization of Robotic Manipulators,"* Proceedings of ASME 20th Biennial Mechanisms Conference, Sept. 25-28, Kissimmee, Florida, Vol. 3, pp. 441-447.

[26] Gupta, K.C., and Roth, B., 1982, *"Design Considerations for Manipulator Workspace,"* ASME Journal of Mechanical Design, Vol. 104, pp 704-712.

[27] Gupta, K.C., 1986, *"Rotatability Considerations for Spherical Four-Bar Linkages With Applications to Robot Wrist Design,"* ASME Journal of Mechanisms, Transmissions, and Automation in Design, Vol 108, pp. 387-391.

[28] Harary, F., 1969, Graph Theory, Addison Wesley.

[29] Hollerbach, J.M., and Sahar, G., 1983, *"Wrist-Partitioned, Inverse Kinematic Accelerations and Manipulator Dynamics,"* The International Journal of Robotics Research, Vol. 2, No. 4, pp. 61-76.

[30] Hsu, M.S., and Kohli, D., 1987, *"Boundary Surfaces and Accessibility Regions for Regional Structures of Manipulators,"* Mechanisms and Machine Theory, Vol. 22, No. 3, pp. 277-289.

[31] Jacobsen, S.C., Wood, J.E., Knutti, D.F., and Biggers, K.B., 1985, *"The Utah/MIT Dextrous Hand: Work in Progress,"* The International Journal of Robotics Research, Vol. 3, No. 4, pp. 21-50.

[32] Kohli, D, and Hsu, M.S., 1987, *"The Jacobian Analysis of Workspace of Mechanical Manipulators,"* Mechanisms and Machine Theory, Vol. 22, No. 3, pp. 265-275.

[33] Kumar, A., and Waldron, K.J., 1980, *"The Dexterous Workspace,"* ASME Paper No. 80-DET-108.

[34] Kumar, A., and Waldron, K.J., 1981, *"The Workspace of a Mechanical Manipulator,"* ASME Journal of Mechanical Design, Vol. 103, No. 3, pp. 665-672

[35] Lawrence, J. D., 1972, A Catalog of Special Plane Curves, Dover Publications, New York.

[36] Leaver, S.O., and McCarthy, J.M., 1987, *"The Design of Three-Jointed, Two-Degree-of-Freedom Robot Fingers,"* ASME Advances in Design Automation, Vol. 2: Robotics, Mechanisms, and Machine System, DE-Vol.10-2, pp. 127-134.

[37] Lin, C.C., and Tsai, L.W., 1989, *"The Development of an Atlas of Bevel-Gear-Type Spherical Wrist Mechanisms,"* Proceedings of First National Conference on Applied Mechanisms and Robotics, Paper No. 89-AMR-2A-3, Cincinnati, OH., Nov. 5-8, 1989.

[38] Lin, C.C., and Tsai, L.W., 1990, *"The Trajectory Analysis of Spherical Planetary Gear Trains,"* submitted for Publication in ASME Journal of Mechanical Design and for presentation at The 1991 ASME Design Automation Conference.

[39] Lin, C.C., and Tsai, L.W., 1991, *"The Workspace of Three-Degree-of-Freedom, Four-Jointed Spherical Wrist Mechanisms,"* Submitted for presentation at the 1991 IEEE International Conference on Robotics and Automation, to be held in Sacramento, CA.

[40] Long, G.L., Paul, R.P., Fisher, W.D., 1989, *"The Hamilton Wrist: A Four-Revolute-Joint Spherical Wrist Without Singularities,"* Proceedings of 1989 International Conference On Robotics and Automation, Scottsdale, AZ, pp. 902-907.

[41] Manseur, R, and Doty, K., 1988, *"A Fast Algorithm for Inverse Kinematic Analysis of Robot Manipulators,"* The International Journal of Robotics Research, Vol. 7, No. 3, pp. 52-63.

[42] Manseur, R, and Doty, K., 1989, *"A Robot Manipulator with 16 Real Inverse Kinematic Solution Sets"* The International Journal of Robotics Research, Vol. 8, No. 5, pp. 75-79.

[43] Mayourian, M., and Freudenstein, F., 1984, *"The Development of an Atlas of the Kinematic Structures of Mechanisms,"* ASME J. of Mechanisms, Transmission, and Automation in Design, Vol. 106, pp. 458-461.

[44] Mayourian, M., 1985, *"The Creation of Mechanisms According to the Separation of Kinematic Structure and Function and Its Partial Automation,"* Engr., Sc.D. Dissertation, Columbia

[45] McCarthy, J. P., 1945, *"The Limacon and The Cardioid,"* Math. Gazette, Vol. 29, pp. 219-220.

[46] Milenkovic, V., 1987, *"New Non-Singular Robot Wrist Design,"* Robots 11 Conference Proceedings RISME. 17th International Symposium on Industrial Robots, Chicago, April 26-30, pp. 13-29-13-42.

[47] Paul, R.P., and Stevenson, C.N., 1983, *"Kinematics of Robot Wrists,"* International Journal of Robotics Research, Vol. 2, No. 1, pp. 31-38.

[48] Paul, R.P., and Zhang, H., 1986, *"Computationally Efficient Kinematics for Manipulators with Spherical Wrists Based on the Homogeneous Transformation Representation,"* International Journal of Robotics Research, Vol. 5, No. 2, pp. 32-44.

[49] Pennock, G.R., and Yang, A.T., 1985, *"Application od Dual-Number Matrices to the Inverse Kinematics Problem of Robot Manipulator,"* ASME J. of Mechanisms, Transmissions, and Automation in Design, Vol. 107, No. 2, pp. 201-208.

[50] Pieper, D.L., 1968, *"The kinematics of Manipulators under Computer Control,"* Ph.D. Thesis, Department of Computer Science, Standford University.

[51] Poole, H. H., 1989, Fundamentals of Robotics Engineering, Van Nostrand Reinhold, New York, NY.

[52] Ravisankar, R., and Mruthyunjaya, T. S., 1985, *"Computerized Synthesis of the Structure of Geared Kinematic Chains,"* Mechanisms and Machine Theory, Vol. 20, No. 5, pp. 367-387.

[53] Rivin, E.I., 1987, Mechanical Design of Robots, McGraw-Hill Book Company. New York.

[54] Rosheim, M.E., 1989, Robot Wrist Actuators, John Wiley & Sons. New York.

[55] Roth, B., 1975, *"Performance Evaluation of Manipulators From Kinematic Viewpoint,"* NBS Special Publication- Performance Evaluation of Programmable Robots and Manipulators, pp. 39-61.

[56] Salisbury, J.K. Jr., 1982, *"Kinematic and Force Analysis of Articulated Hands,"* Ph.D. Thesis, Department of Mechanical Engineering, Standford University.

[57] Sohn, W. J., and Freudenstein, F., 1986, *"An Application of Dual Graphs to the Automatic Generation of the Kinematic Structures of Mechanisms,"* ASME J. of Mechanisms, Transmissions, and Automation in Design, Vol. 108, No. 3, pp. 392-398.

[58] Stackhouse, T., 1979, *"A New Concept in Wrist Flexibility,"* Proceedings of the 9th International Symposium on Industrial Robots, Washington, DC, pp. 589-599.

[59] Trevelyan, J.P., Kovesi, P.D., Ong, M., and Elford, D., 1986, *"ET: A Wrist Mechanism without Singular Positions,"* The International Journal of Robotics Research, Vol. 4, No. 4., pp. 71-85.

[60] Tsai, L.W., and Morgan, A.P., 1985, *"Solving the Kinematics of the Most General Six and Five-Degree-of-Freedom Manipulators by Continuation Methods,"* ASME J. of Mechanisms, Transmissions, and Automation in Design, Vol. 107, No. 2, pp. 189-200.

[61] Tsai, L. W., 1987, *"An application of the Linkage Characteristic Polynomial to the Topological Synthesis of Epicyclic Gear Trains,"* ASME J. of Mechanisms, Transmissions, and Automation in Design, Vol. 109, No. 3, pp. 329-336.

[62] Tsai, L.W., 1988, *"The Kinematics of Spatial Robotic Bevel-Gear Train"*, IEEE J. of Robotics and Automation, Vol. 4, No.2, pp. 150-156.

[63] Tsai, L.W., and Lin, C.C., 1988, *"The Creation of Nonfractionated, Two-Degree-of-Freedom Epicyclic Gear Trains,"* ASME J. of Mechanisms, Transmissions, and Automation in Design, Vol. 111, No. 4, pp. 524-529.

[64] Uicker, J. J., Jr., and Raicu, A., 1975, *"A Method for the Identification and Recognition of Equivalence of Kinematic Chains,"* Mechanism and Machine Theory, Vol. 10, pp 375-383.

[65] Vijaykumar, R., Tsai, M.J., and Waldron, K.J., 1985, *"Geometric Optimization of Manipulator Structures for Working Volume and Dexterity,"* Proceed-

ings of the IEEE International Conference on Robotics and Automation, St. Louis, pp. 228-236.

[66] Yan, H. S., and Hall, A. S., 1981, *"Linkage Characteristic Polynomials: Definitions, Coefficients by Inspection,"* ASME Journal of Mechanical Design, Vol. 103, No. 3, pp. 578-584.

[67] Yan, H. S., and Hall, A. S., 1982, *"Linkage Characteristic Polynomials: Assembly Theorem, Uniqueness,"* ASME Journal of Mechanical Design, Vol. 104, No. 2, pp. 11-20.

[68] Yan, H. S., and Hwang, W. M., 1983, *"A Method for the Identification of Planar Linkage Chains,"* ASME Journal of Mechanical Design, Vol. 105, No. 4, pp. 658-662.

[69] Yoshikawa, T., 1985, *"Manipulability of Robotic Mechanisms,"* The International Journal of Robotic Research, Vol. 4, No. 2, pp. 3-9.